Kinetics of the β-AlFeSi to α-Al(FeMn)Si transformation in Al-Mg-Si alloys

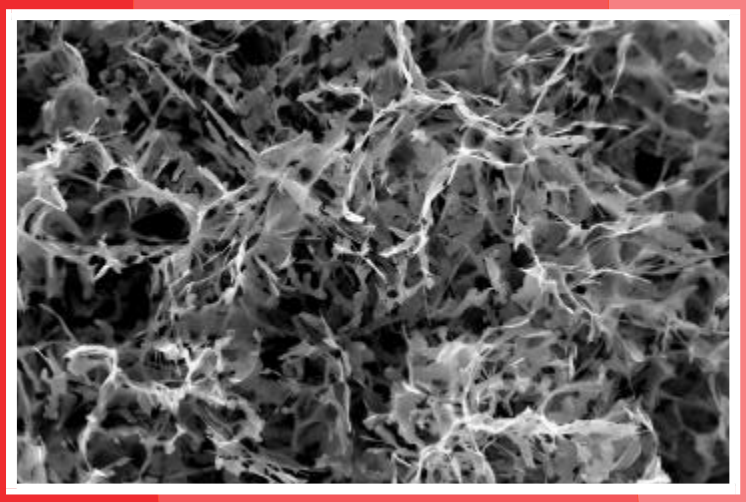

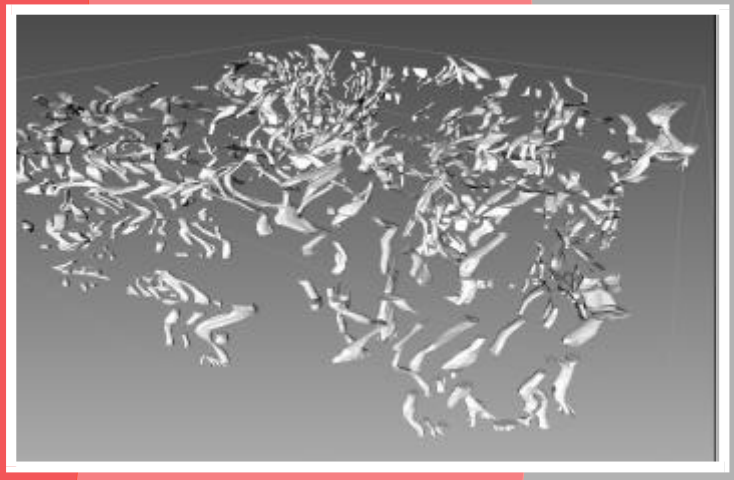

Niels Kuijpers

Kinetics of the β-AlFeSi to α-Al(FeMn)Si transformation in Al-Mg-Si alloys

Kinetics of the β-AlFeSi to α-Al(FeMn)Si transformation in Al-Mg-Si alloys

PROEFSCHRIFT

ter verkrijging van de graad van doctor
aan de Technische Universiteit Delft,
op gezag van de Rector Magnificus Prof. dr. ir. J.T. Fokkema,
voorzitter van het College voor Promoties,
in het openbaar te verdedigen op maandag 2 februari 2004 om 15.30 uur

door

Niels Cees Willem KUIJPERS

natuurkundig ingenieur
geboren te Oss

Dit proefschrift is goedgekeurd door de promotor:
Prof. dr. ir. S. van der Zwaag

Samenstelling promotiecommissie:

Rector Magnificus, voorzitter
Prof. dr. ir. S. van der Zwaag, Technische Universiteit Delft, promotor
Dr. W. H. Kool, Technische Universiteit Delft, toegevoegd promotor
Prof. ir. L. Katgerman, Technische Universiteit Delft
Prof. dr. ir. P. Wesseling, Technische Universiteit Delft
Prof. dr. R. Boom, Technische Universiteit Delft
Prof. dr. ir. J. Huétink, Technische Universiteit Twente
Prof. F. Delannay, Université Catholique de Louvain (België)

This research was carried out under the project number MP 97009-3 in the framework of the Strategic Research Program of the Netherlands Institute for Metals Research (NIMR) in the Netherlands (www.nimr.nl).

ISBN 90-77172-07-6

Keywords: Aluminium alloys, Homogenisation, Modelling, Transformation, Intermetallics

Printed in the Netherlands

Table of contents

Chapter 1

Introduction

During the homogenisation process of as-cast Al-Mg-Si alloys a phase transformation takes place transforming single plate-like β-AlFeSi particles into multiple, more rounded, α-AlFeMnSi particles. This intermetallic phase transformation is of technological interest since it improves the extrudability of the aluminium considerably. Therefore this transformation will be analysed in more detail in this thesis. In this introduction, first the scope of the thesis will be given, detailing the focal points of this research. Subsequently some background will be given about the intermetallic phase transformations as well as the approaches to model intermetallic transformations. Finally the outline of this thesis is presented, explaining briefly the contents and conclusions of each separate chapter.

1.1 Scope of this thesis

Figure 1.1 shows the different process steps that are carried out for the production of aluminium extrusion profiles, such as frames and pipes. The scheme shows that, after casting, the aluminium material is "homogenised". During this homogenisation process the aluminium billets are annealed in a furnace for a few hours at temperatures between 530 and 600°C [1]. Subsequently the billets are cooled down and transported to the extrusion press; the billets are re-heated and extruded in an extrusion press. During this extrusion process aluminium billets are pressed through a die with a shaped opening, as depicted schematically in Figure 1.1. In an optional final step, the extrusion profiles are artificially age-hardened. Among all these process steps, the homogenisation of Al-Mg-Si aluminium billets is a very important one, since it gives significant changes in the microstructure of the alloy, leading to an improved extrudability of the material and improved properties of the final extruded product [2]. Historically, the homogenisation

process is quite a young addition to the process cycle. It was introduced in industry around 1960 [2].

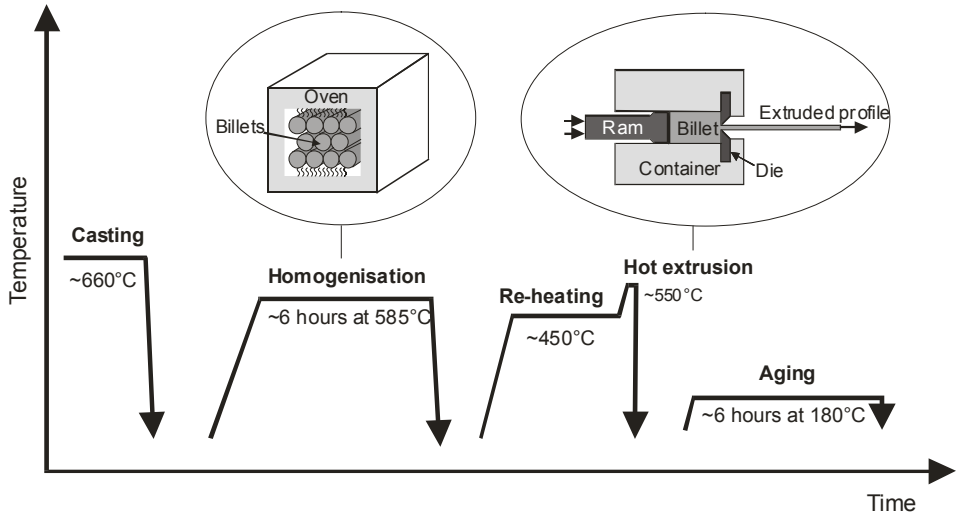

Figure 1.1 Schematic temperature path of the aluminium heating process during the production of extrusion profiles. The homogenisation and the hot extrusion processes are displayed schematically.

One important microstructural change during homogenisation is the transformation of plate-like intermetallic β-Al_5FeSi particles to multiple rounded α-AlFeMnSi type of intermetallic particles [3-5]. The change in morphology is shown in Figure 1.2. Figure 1.2a shows that the plate-like β particles in the as-cast state appear as needles in a two dimensional micrograph. Figure 1.2b shows that after homogenisation these β plates are transformed into a string of separate coarse α particles. The β-to-α phase transformation considerably improves the extrusion process of the aluminium since the transformed α-particles in the homogenised material improve the ductility of the material and the surface quality of the extruded material. Often, the as cast microstructure is not extrudable at all as many cracks appear when as cast material is extruded anyway. Additional microstructural changes, such as the dissolution of Mg_2Si or Si particles, also occur during homogenisation (See Appendix 1) [6]. However, since the Mg_2Si or Si particles dissolve rather fast, it is the β-to-α transformation kinetics which determines the minimum homogenisation time that is needed to get the material in a suitable state for extrusion.

A better understanding of the β-to-α transformation kinetics is important, since this gives a better insight into the effects of process parameters of the homogenisation, such as temperature [7], homogenisation time, cast microstructure [8] and chemical composition [9]. It is the objective of this research to characterise the β-to-α transformation kinetics in Al-Mg-Si alloys (6xxx Al alloys) and to develop a physical

model that describes this transformation. This specific objective belongs to the broader scientific objective to get a better insight into the total behaviour of intermetallic constituents during thermal processing.

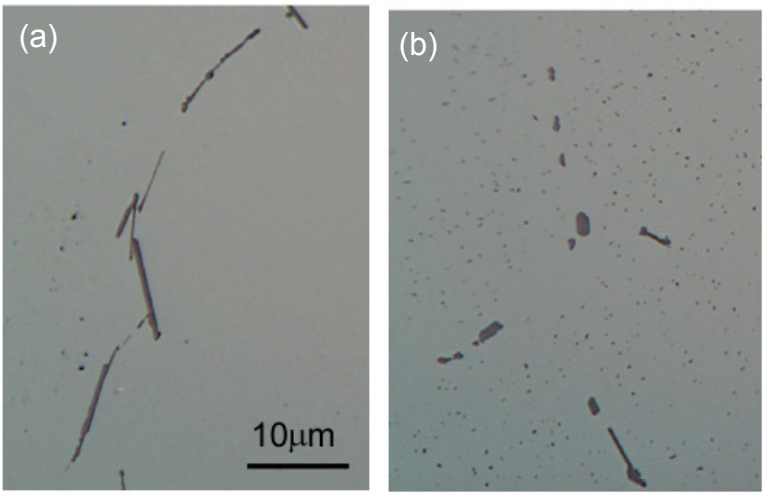

Figure 1.2 The β-to-α transformation in Al-Mg-Si alloys (AA 6005A series). (a) β particles in the as-cast state (b) Transformed α particles after homogenisation at 540°C for 32 hours. Both pictures have the same scale and were obtained by optical microscopy.

Experimentally, this thesis focuses on the β-to-α transformation in extrusion alloys which are common in commercial practice, such as AA 6005A and AA 6063 alloys. Most experiments were performed by microscopic analysis at the micrometer scale, using techniques such as SEM and optical and laser-confocal microscopy. A physical model was made, which uses observed morphological features and dimensions of the intermetallics and realistic diffusion coefficients as model parameters. Furthermore, we used existing thermo-dynamical databases to derive the boundary conditions. We aimed to obtain a generic model that is potentially applicable for a wider range of alloys than the alloys investigated experimentally in this thesis.

1.2 Background of homogenisation

1.2.1 Intermetallic phases in AA 6xxx Al series alloys

The AA 6xxx Al series alloys are also called the Al-Mg-Si series, since their main alloying elements are Mg (0.3-1.2 wt.%) and Si (0.4-1.3 wt.%), which allow age-hardening by coherent or semi-coherent Mg-Si precipitates. However, besides Mg and Si also other elements such as Fe (0-0.8 wt.%) and Mn (0-0.8 wt.%) can be present [10]. Since Fe has a very low solubility in the Al-matrix, almost all Fe present in 6xxx Al alloys will bind with the excess of Si and the abundant Al to form typically one volume

percent of Fe-containing intermetallics [11]. During solidification, these intermetallics form at the edges of the aluminium dendrites by an eutectic reaction, which explains their plate-like shape. Most of these intermetallics are the plate-like β-AlFeSi phase while a small fraction of the phases can be the cubic α_c-Al(FeMn)Si phase with a so-called "Chinese-script-like" morphology. These Fe-containing intermetallics are also called "constituents" since they do not dissolve and remain as a separate phase in the Al-matrix even after long homogenisation times, although they may change in phase composition and phase morphology (See Figure 1.2).

Table 1.1 The structural variance of the prevalent intermetallic phases in 6xxx series.

Notation	stoichiometry	Bravais lattice/ Space group	Lattice parameters and space group	Density (δ) kg/m^3	References
β	$Al_{4.5}FeSi$ [14], Al_5FeSi [12]	Monoclinic	a = 6.12 Å b = 6.12 Å c = 41.5 Å β = 91°	3300-3350	[12-16]
α_h (α')	Al_8Fe_2Si	Hexagonal/ $P6_3$	$a = b$ = 12.3 Å c = 26.2 Å	3580	[12, 17,18]
α_c	(Fe containing) $Al_{12}Fe_3Si$ [19], $Al_{12-15}Fe_3Si_{1-2}$[23]	Cubic /Im_3	a = 12.56 Å	3640	[12, 19-23]
	(Fe+Mn containing) $Al_{12}(FeMn)_3Si$ [24], $Al_{15}(FeMn)_3Si_2$ [12]	Cubic/ Im_3- Pm_3	a = 12.56-12.68 Å	3640-3630	[12,13,18,22,24-27]
	(Mn containing) $Al_{12}Mn_3Si$ [24], $Al_{15}Mn_3Si_2$ [12], Al_9Mn_2Si [22]	Cubic /Pm_3	a = 12.68 Å	3630	[12,20,22,24,28,29]

Table 1.1 shows the characteristics of three most prevalent intermetallics in 6xxx Al series alloys: the monoclinic β-AlFeSi phase, the hexagonal α_h-AlFeSi and cubic α_c-Al(FeMn)Si [12-29]. In this table, the α_c phase is split up into three types: an α_c phase containing Fe, an α_c phase containing Fe and Mn, and an α_c phase containing Mn. The stoichiometry of each phase is different and further different phase properties are

reported by different authors. The molar volumes of the intermetallics are approximately the same as for aluminium ($V_m \cong$ 10 cm^3/mol), indicating that the atomic distances of the intermetallics are approximately the same as for aluminium. The densities of the intermetallic phases are somewhat higher than those of aluminium (δ_{Al}=2670 kg/m^3) due to heavier elements such as Fe and Mn which are present in the phases.

The monoclinic β phase

The β-AlFeSi has a monoclinic crystal structure. This is an important phase in as-cast aluminium 6xxx alloys, where it has a plate-like morphology with a length up to 20 μm and a thickness of 0.1-1 μm (See Chapter 4). The approximate stoichiometry of this phase is Al_5FeSi [12]. In contrast to the α_c phase, no Mn can be present in the β-phase. Figure 1.3 shows a TEM image on the β-AlFeSi/Al interface, which is a sharp interface. Mulazimoglu *et al.* [21] found that the β plates are highly faulted, with (001) planar defects lying parallel to the plane of the phase platelet

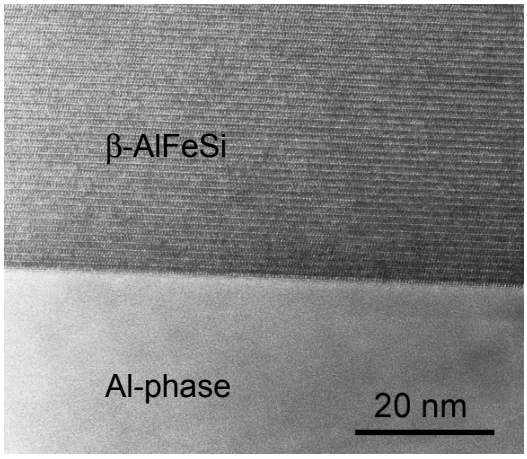

Figure 1.3 A high resolution TEM image of a β/Al interface. The image was made on cast 6005A.

The hexagonal α_h phase

Some authors also denote this phase as α′. The stoichiometry of this phase is approximately Al_8Fe_2Si with Fe concentrations ranging from 30-33 wt.% Fe and Si concentrations ranging from 5-12 wt.% Si [12]. The α_h forms in 6xxx alloys with Mn, V or Cr concentrations less than ~0.01 wt.% [4,8]. Higher concentrations of those elements lead to stabilisation of the cubic α_c phase, which is structurally related to the α_h phase. During homogenisation of high purity Al-Fe-Si cast alloys, it was found that the β-Al_5FeSi phase transforms to the stable α_h- Al_8Fe_2Si phase [30]. Since industrial

alloys mostly have small additions of Mn and or Cr, this transformation is rarely observed in industrial practice and usually the β-Al_5FeSi phase transforms to the stabilised α_c-$Al_{12}(FeMn)_3Si$ phase. Therefore, we will not further deal with the α_h phase.

The cubic α_c-phase

In typical Al-Fe-Si extrusion alloys small additions of V [19], Cr [31] and/or Mn [12] are required to form α_c during homogenisation. In this case, the α_c phase seems to be the thermodynamically stable phase since it is also observed after long homogenisation times [11]. It was found that approximately 1.5 wt.% Mn has to be present in the α_c phase to stabilise this phase [12]. In the α_c phase the Fe atoms are interchangeable with V, Cr and/or Mn atoms [24] causing a change in crystallographic space group and a small shift in lattice parameters, as indicated in Table 1.1. The Fe-containing α_c has approximately the $Al_{12}Fe_3Si$ stoichiometry [24]. The Mn-containing α_c phase has approximately the $Al_{12}Mn_3Si$ stoichiometry [24]. Various other stoichiometries of the Fe- and Mn-containing α_c phase were found in literature, of which some are presented in Table 1.1. As an approximation, the stoichiometry of the α_c phase is generally displayed by $Al_{12}(Fe_xMn_{1-x})_3Si$ [24]. Some literature indicates that the stoichiometry of the α_c phase changes slightly with the Mn content [32,12]. However, since these changes are small, the approximate $Al_{12}(Fe_xMn_{1-x})_3Si$ stoichiometry is utilised for all calculations and models presented in this thesis.

Unlike the monoclinic β-phase, the α_c-phase exhibits no faceting or twinning and has a rough or diffusive interface with the matrix [21]. In literature, gradients of Mn in the α_c particles were reported, probably caused by the inward diffusion of Mn during the homogenisation process [25].

Three different types of cubic α_c intermetallics phases can be present in AA 6xxx alloys: (a) formed during casting, (b) formed as dispersoids, (c) formed by the β-to-α transformation. Although the crystal structures of those types are all cubic, all three types have prominent differences in morphology, size and distribution:

(a) α_c formed during casting: The morphology of these α_c particles is often called "Chinese-script" morphology, since in two dimensional sections the eutectic has the morphology of the Chinese characters. The morphology is rounded, has a large variation in length and thickness and particles have a size of ~5 μm. Mostly the as-cast α_c phases have a high Fe/Mn ratio.

(b) α_c as dispersoids: These dispersoids are formed in the aluminium matrix during homogenisation. Alloys with a high Mn content will form α_c dispersoids that have sizes of 50-200 nm which are uniformly distributed. The dispersoids commonly

have a low Fe/Mn ratio and therefore the stoichiometry is approximately equal to that of α_c-$Al_{12}Mn_3Si$.

(c) α_c formed after the β-to-α transformation: The transformed α_c particles have a size of approximately ~1 μm and are present as a string of α_c particles located on the previous location of the original β particle. An example of these particles is given in Figure 1.2b. Mostly these particles have an intermediate Fe/Mn ratio, since Mn diffuses into the α_c particles during the homogenisation.

In this thesis we will only investigate the α_c phases of type (c) since the β-to-α transformation is the main focus point of this work.

Other phases

In addition to the common α and β phases, other rare Al-Fe-Mn-Si intermetallics in 6xxx series have been described in literature: Monoclinic β′, β* [26,15], Rhombohedral α_R [33], c-Centred orthorhombic $\alpha''(q_1)$ [26,34], c-Centred monoclinic α_T [17], Monoclinic q_2 [34] and Monoclinic α_v [24]. Since we did not observe them in this research, we only mention them here for the sake of completeness.

1.2.2 The β-to-α phase transformation

The morphology change, of the β-AlFeSi phase during the phase transformation in the 6005 series of alloys, is shown in Figure 1.2. The plate-like β particle transformed to a string of multiple smaller and more rounded cubic or hexagonal α particles. This thesis will mainly focus on this particular phase transformation and its kinetics. The literature found on the β-to-α transformation will be summarised below.

Morphological changes due to the transformation

Although many articles have been published that describe the change of intermetallic phase compositions during homogenisation, less is known about the kinetics and morphological changes of the β-to-α transformation. Some authors comment briefly on α_c particles that nucleate at the beginning of the transformation on the boundary of β phases [31,4]. Birol *et al* [31] observed that the β plates are gradually replaced by uniform strings of cubic and/or hexagonal α-AlFeSi particles. Zajec *et al* [4] observed that the long plate-like intermetallic particles break up into a necklace structure. They found that individual platelets, in the intermediate homogenisation state, exhibit partial transformation to the α phase. The islands of the α phase then coarsen and spheroidise at the expense of the remaining β-phase particles The remaining α particles coarsen when the homogenisation process takes longer than approximately 10 hours [4,23].

Influence of alloy content on the transformation rate

The chemical composition of the 6xxx alloy influences the β-to-α transformation rate as well as the stability of the intermetallic phases. For industrial processing it is crucial to find an alloy with a composition such that the as-cast β particles transform as quickly as possible to the α phase, leading to a short homogenisation time.

It was found that both Mn and Si have a significant effect on the transformation rate. Mn acts as a catalyst for the transformation, accelerating the β-to-α rate by nearly two orders of magnitude [1,4,9,35]. For alloys with a low Mn content (<~0.01 wt.%) it is observed that the β plates first transform to the cubic α_c-phase and subsequently transform to the hexagonal α_h–phase, which is the thermodynamic stable phase for this Mn content [8,12,23,30]. For high Mn contents (~0.02-0.10 wt.%) it is observed that the β plates transform to the thermodynamically stable cubic α_c phase only [1,4,35].

The Si content has a significant effect of the transformation rate too [1,4,36]. Zajac *et al* noticed that 6xxx alloys with 0.45 wt.% Si transform rather fast, whereas alloys with 0.80 wt.% Si hardly show any transformation. Kolby *et al* suggested that the β-AlFeSi phase is thermodynamic stable in alloys containing high Si levels (>~1 wt.%). Hence, for these alloys the as-cast β-AlFeSi phases will not transform.

It should be noted that in some articles the effects of addition of minor amounts of strontium was presented. In those investigations it was found that addition of about 30 ppm to 300 ppm strontium enhances the formation of the α_h-phase during casting, giving a coarser morphology to the intermetallics than otherwise reached with the β-phase [21, 37]. It has been suggested that strontium sticks to the growing interface of the α_h-phase [21,37]. Although the additions of strontium seemed very promising, it has several additional effects such as grain-refining and change in kinetics of the precipitation reactions of Mg-Si particles [38]. The fact that the additional effects are not well known delays its introduction in the commercial production process of aluminium extrusion alloys.

1.2.3 Improvement of extrudability by the β-to-α transformation

In the previous paragraphs we used the term “extrudability” [39,40]. This extrudability is qualitatively defined by the maximum production speed attainable for a given press capacity while still obtaining the desired mechanical properties, surface quality and geometric tolerances of the extrudate. As described earlier, the extrudability increases due to the β to α transformation. It is, therefore, useful to define a parameter that quantifies the degree of β-to-α transformation of a billet after homogenisation, since this parameter influences the extrudability of the billet. This parameter f_α is defined as the ratio of the α volume and the total volume of intermetallics. It has been found that a

relative α-fraction of at least f_α=0.85, but preferably f_α=0.95, is required to get an optimal extrudability [1]. The increase of extrudability with the relative α fraction is caused by both improvement of the ductility and improvement of the extrudate surface defects [2,41,42], which effects will be summarised below.

Improvement of ductility

Some papers dealing with ductility regarding the β-to-α transformation are found in refs. [4,43- 45]. The explanations are summarised below:

1. The coverage ratio, defined as the area of β particles on the grain boundaries divided by the total area of grain boundaries, correlates with the ductility in extrusion [43]. The β-to-α transformation leads to a lower coverage ratio of the dendrites and therefore leads to an improvement of the ductility. The β plates, with a high coverage of the dendrites, block dislocations by the interconnected network, making it difficult to deform the material, whereas the more rounded small α particles allow the dislocation to move around, making it easier for the material to change its shape.
2. It is not necessarily only the degree of β-to-α transformation that increases extrudability but also the associated improvement of the Mg_2Si phase distribution [4].

Reduction in surface defects

Various types of surface defects may occur during the extrusion process [41,42,46,47]. One type of these defects is the so-called “pick-up". During the extrusion process, the aluminium adheres locally to the extrusion die, collecting small deposit particles on the surface which shear the extrudate surface, leading to an eyesore scratch on the surface of the aluminium profile. Various hypotheses exist in literature that explain why insufficiently homogenised alloys, with many β particles, are prone to more pick-up defects than adequately homogenised alloys. So far, it is not yet clear which of these are the most plausible. The hypotheses are summarised below.

1. The weak adhesion of the β intermetallics to the Al matrix [43] causes the β particles to become loose from the matrix. During extrusion, these loose β particles stick to the die surface and scratch the aluminium surface. The transformed α particles are assumed to have a better adhesion, leading to a lower probability to de-bond from the Al matrix, and therefore giving less pick-up defects.
2. The sharp tips of the β particles initiate micro-cracks during the deformation, and therefore start cracking the aluminium surface. The transformed α_c particles are more rounded and therefore cause less local cracking at the surface.

3. Only local eutectic melting leads to pick-up at the surface of the aluminium matrix. Table 1.2 shows some relevant eutectic melting temperatures. A more extended list of eutectic melting temperatures has been published in [12]. The eutectic melting temperature of homogenised material containing α particles (~630°C) is higher than the temperature at the die, which will not result in the formation of pick up defects. However, insufficiently homogenised material still contains β particles and has a lower eutectic melting temperature (612°C) which might lead to pick-up at the surface of the matrix. It is also stated that local melting may occur as some Mg_2Si or Si phases are still present after homogenisation and re-heating, which promote eutectic melting at lower temperatures. If β-AlFeSi intermetallics are present, the ductility is limited by the ternary reaction Al+β-AlFeSi+Si/Mg_2Si → liquid, which occurs at lower temperatures than for α_h phases [4].

Table 1.2 Some eutectic melting temperatures in Al-Mg-Si alloys.

Melting Temperature	Reaction
~575°C [12]	Al+ β-AlFeSi+Si→Liquid
~576°C [12,48]	Al+ β-AlFeSi+Mg_2Si→Liquid +α_h-AlFeSi
~577°C [12]	Al+ Si→Liquid
~587°C [48]	Al+ Mg_2Si →Liquid
~612°C [12]	Al+ β-AlFeSi→Liquid+α_h-Al(FeMn)Si
~630°C [12]	Al+α_h-AlFeSi→Liquid +Al_3Fe

1.3 Background of modelling of intermetallic phase transformations

Many microstructural changes, such as dissolution of precipitates and transformation of intermetallics, which take place during heat-treatment of aluminium alloys are controlled by diffusion of the alloying elements. In this thesis the β-to-α transformation is modelled by a solid state diffusion of elements, *i.e.* Fe, Si and Mn, in the aluminium matrix. Diffusion is described in more detail in Section 1.3.1. The diffusive mass transport of elements is induced by a concentration gradient in the matrix between the interface of the α and β intermetallic. These matrix interface concentrations are described in Section 1.3.2. Due to the interfacial concentration difference, elements are injected by the β particles into the Al-matrix and diffuse through the aluminum matrix

towards the α particle. This leads to the growth of the α phase and the dissolution of the β phase. A general description of the derivation of moving boundaries of intermetallic phases is given in Section 1.3.3.

1.3.1 Diffusion

Table 1.3 presents a collection of diffusion coefficients of the main alloying elements in aluminium. The diffusion coefficient depends on the temperature according to the Arrhenius relation where D_0 is a pre-factor, and Q^d is the activation energy [49]. The experimentally determined values of the coefficients depend on the experimental techniques used and the temperature ranges investigated. Therefore there is some spread in the values of the diffusion coefficients found by the various authors.

Table 1.3 demonstrates that the diffusion coefficients of Mn and Fe are low when compared to the diffusion coefficients of Mg and Si. This indicates that the dissolution, growth or transformation of a Mn/Fe-containing intermetallic will proceed slower than the dissolution of precipitates that do not contain Mn or Fe, such as Mg/Si precipitates. The table also shows that Mn and Fe have higher activation energies for diffusion than Mg and Si, indicating that diffusion controlled intermetallic transformations have a stronger temperature dependence than the growth or dissolution of non-intermetallics.

Apart from diffusion in the matrix, there can also be some diffusion inside the intermetallics [50]. However, in most cases this intermetallic diffusion is negligible: *e.g.* the Fe diffusion coefficient in Fe_3Si is in the order of 10^{-18} m^2s^{-1} at 540°C and 10^{-17} m^2s^{-1} at 580°C [23].

Table 1.3 Diffusion coefficients of main elements in 6xxx aluminium series.

	Temperature range	Reference	D_0 (m^2s^{-1})	Q^d (kJ/mol)	D (m^2s^{-1}) 540°C	D (m^2s^{-1}) 580°C
Mg	394 °C - 655 °C	Rothman *et al.* [51]	$1.24 \cdot 10^{-4}$	130	$5.14 \cdot 10^{-13}$	$1.27 \cdot 10^{-12}$
	500 °C - 580 °C	Fujikawa. [52] (*)	$1.06 \cdot 10^{-4}$	133	$3.00 \cdot 10^{-13}$	$7.53 \cdot 10^{-13}$
Si	345 °C –631 °C	Bergner *et al.* [53]	$0.35 \cdot 10^{-4}$	124	$3.83 \cdot 10^{-13}$	$8.97 \cdot 10^{-13}$
	480 °C - 620 °C	Fujikawa. [54] (*)	$2.02 \cdot 10^{-4}$	136	$3.66 \cdot 10^{-13}$	$9.40 \cdot 10^{-13}$
Mn	500 °C -650 °C	Bergner *et al.* [53] (*)	$1.275 \cdot 10^{-1}$	229	$2.43 \cdot 10^{-16}$	$1.18 \cdot 10^{-15}$
Fe	520 °C-649 °C	Beke et al. [55] (*)	$5.3 \cdot 10^{-3}$	183	$8.73 \cdot 10^{-15}$	$3.07 \cdot 10^{-14}$
	550 °C –633 °C	Alexander *et al.*[56]	$1.35 \cdot 10^{-2}$	193	-	$2.13 \cdot 10^{-14}$
	519 °C –658 °C	Hood [57]	91	259	$2.13 \cdot 10^{-15}$	$1.28^{-}10^{14}$

(*) Diffusion coefficients used in the models presented in the thesis.

1.3.2 Solubility relations at the particle interface

Diffusion controlled growth and dissolution of particles in a solid matrix are based on the assumption that there is a thermodynamic equilibrium at the interface of the particle. Therefore, the interfacial matrix concentration is in thermodynamic equilibrium with the particle. For phases with a fixed stoichiometry (*e.g.* β-Al_5FeSi and Mg_2Si) in equilibrium with an ideal matrix it can be derived that the interfacial matrix concentrations of the alloying elements satisfy [58]:

$$\prod_{i=1}^{N} (c_i^s)^{n_i} = k_0 \exp\left(\frac{-Q^s}{RT}\right), \tag{1.1}$$

where N is the number of alloying elements, c_i^s is the equilibrium matrix concentration of element i (wt.%) at the interface, k_0 is a pre-factor, R is the gas constant, T the temperature and n_i is the stoichiometric composition of element i in the precipitate or intermetallic (atom fraction) *i.e.* for the β-$Al_5Fe_1Si_1$ phase, n_1=1/7 (Fe) and n_2=1/7 (Si).

The left hand side of Equation (1.1) is called the solubility product. Table 1.4 gives the parameters of the Arrhenius relation of the solubility product of some common intermetallic and precipitates in 6xxx alloys. These parameters were obtained from own fits with the results from thermodynamic software, such as MT-Data and Thermo-Calc. These programmes use databases which contain data of the Gibbs free energy relations of the phases, abstracted from experimental measurements. The fits were obtained over the temperature and concentration ranges indicated in table 1.4.

Table 1.4 Parameters in Equation (1.1) for some secondary phases in AA 6xxx alloys.

Phase	Stoichiometric parameters	Temperature range	Concentration range (wt.%)	k_0 (-)	Q^s (kJ/mol)
$Al_5Fe_1Si_1$ (**)	n_1=1/7, n_2=1/7	500°C-600°C	$0.01<c^s_{Fe}<0.1$	$8.4\cdot10^{30}$	15.9
α_H-$Al_8Fe_2Si_1$ (**)	n_1=2/11, n_2=1/11	500°C-600°C	$0.01<c^s_{Fe}<0.1$	5.7	18
Mg_2Si_1 (*)	n_1=2/3, n_2=1/3	400°C-600°C	$0.1<c^s_{Mg}<1.0$	$0.79\cdot10^3$	48.0
Si (**)	n_1=1	400°C-600°C	$0.1< c^s_{Si}<1.0$	$1.4\cdot10^3$	48

(*) determined by MTDATA (**) determined by TTAL in Thermo-Calc

An analytical relation of the interfacial matrix concentrations is difficult to achieve when phases have a variable stoichiometry, *e.g.* for the α_c-$Al_{12}(Fe_xMn_{x-1})_3Si$ intermetallic phase. In this case, the relations of the equilibrium matrix concentrations can be derived by numerical algorithms which use thermodynamical databases. By this

numerical method, the equilibrium concentrations are calculated by minimisation of the Gibbs-free energies.

1.3.3 Moving boundaries

During the dissolution or growth of a secondary phase, the interface ejects elements into the Al-matrix or absorbs them from the Al-matrix. The interface moves towards its equilibrium position, where it is in equilibrium with the matrix. In the case of diffusion controlled dissolution, a local mass-balance of a particular element can be made and its velocity at the interface ($v(t)$) can be expressed by a Stefan condition [59], which must apply for all elements:

$$(c_i^p - c_i^s)v(t) = D_i \frac{dc_i}{d\boldsymbol{n}}, \ for \ \ i \in \{1..N\}, \tag{1.2}$$

where $\boldsymbol{n}$ is the unit vector in normal (outward) direction on the moving interface, c_i^p is the particle concentration of element i (wt.%), c_i^s is the equilibrium matrix concentration of element i (wt.%) at the interface, and $\frac{dc_i}{d\boldsymbol{n}}$ is the normal derivative of the concentration at the interface. In this thesis the Stefan approach is used to derive the interface velocity.

For a multi-component diffusion problem, which is the case for the β-to-α_c transformation, it is assumed that the intermetallic interfaces are always in local thermodynamic equilibrium with the aluminium matrix. Therefore Equation (1.1) must be applied to the interface concentrations of both the α and β particles. Since the boundaries are moving, also Equation (1.2) must be valid. For a matrix concentration c_i^0 of element i (far from the interface) it can be derived that, in addition to equation (1.1), an extra condition to the *initial* interfacial matrix concentration of a phase [59] is given by:

$$\frac{c_i^0 - c_i^{s(t=0)}}{c_i^p - c_i^s} = f\left(\frac{k}{2\sqrt{D_i}}\right) \ for \ \ i \in \{1..N\}, \tag{1.3}$$

where c_i^0 is the matrix concentration of element i, far away from the interface. The function $f(x)$ equals $f(x) = x\sqrt{\pi} \cdot erfc(x) exp(x^2)$. For this function $f(0)=0$, $f(1)\approx 0.5$ and $f(2)\approx 1$. The parameter k originates from the solution equations of particle dissolution or growth in a planar unbounded domain [58,59]. It represents the rate parameter in the

equation $S(t) = S_0 + k\sqrt{t}$, where S(t) defines the interface position as a function of time.

For the models of intermetallic phase transformations it is often sufficient to derive the concentration field of the slowest diffusion element (*e.g.* Fe), since the transformation rate is determined by the element with the lowest diffusion coefficient.

1.4 Outline of thesis

This thesis consists of an experimental part (Chapter 2-5) and a modelling part (Chapters 6 and 7).

Chapter 2 gives an assessment to the experimental methods for the determination of the relative α_c fraction (f_α). In as-cast aluminium f_α will be close to zero and during homogenisation f_α increases to unity. A number of techniques was assessed and it was demonstrated that Scanning Electron Microscopy (SEM) in combination with Electron Dispersive X-ray (EDX) was the most accurate.

Chapter 3 presents the experimental description of α_c particles that are nucleted on β plates. These particles were observed by the Laser Confocal Microscope on deep-etched samples. The confocal microscope in combination with 3D sectioning is able to obtain 3-dimensional quantitative data of the α_c particles and of the β plates. Different types of α_c particles are investigated and described.

Chapter 4 presents SEM investigations of intermetallics in 2D cross sections. Using this experimental method the 2-dimensional morphological evolution of the α_c nuclei and β plates at different stages of the homogenisation are investigated. A general hypothesis is made to describe the different stages of growth of the α_c particles on the β plate during the homogenisation. This hypothesis is used for the models presented in Chapters 6 and 7.

Chapter 5 analyses further the 3-dimensional characteristics of the microstructures by serial sectioning of samples. The morphological features of the intermetallics are investigated at different stages of the homogenisation process and at different homogenisation temperatures. Interpretation of the local distribution function of surface curvature gives some additional information on the morphological changes during the homogenisation treatment.

Chapter 6 presents a diffusion-controlled model of the β-to-α_c transformation. A finite element model is constructed to mimic the morphological changes during the phase transformation. It predicts the increase of the relative α_c fraction during the isothermal transformation. Also, an analytical model for a simplified geometry is presented which gives qualitatively similar results as the finite element model. Various morphologies and temperatures are fed in the FEM model, to show their influence on

the transformation. Finally, the predictions of the model are compared to the measured relative α_c fractions.

In Chapter 7 the influence of the Fe, Mn and Si alloy contents on the β-to-α_c transformation is investigated both by experiments and by model calculations. Experimentally, the evolution of the relative α_c fraction during homogenisation is measured for different Mn alloy contents. An increase in the Mn content gives a significant increase of the β-to-α_c transformation rate. The model, presented in Chapter 6 is used to derive the effect of the alloy content on the β-to-α_c transformation rate. As a conclusion of this research it follows that the difference between the interface concentration of Fe at the α- and β-interface, which is evaluated for different Fe, Mn, Si contents, determines the transformation kinetics.

References

[1] N. C. Parson, J. D. Hankin and K. P. Hicklin: *Al-Mg-Si alloy with good extrusion properties.* US-patent (2002) 6,440,359.

[2] O. R. Reiso: *The effect of homogenization treatment on the microstructure properties of aluminium extrusion ingots*. Deutsche Gesellschaft für Metallkunde, Germany (1995) 199-208.

[3] N. C. W. Kuijpers: *Intermetallic phase transformations during homogenisation of 6xxx Al alloys, a literature review*. Internal report of the Netherlands Institute for Metals Research (NIMR), The Netherlands (2000).

[4] S. Zajac, B. Hutchinson, A. Johansson and L.O. Gullman: *Microstructure control and extrudability of Al-Mg-Si alloys microalloyed with manganese*. Mat. Sci. Tech. **10** (1994) 323-333.

[5] A. Valles, R. P. L. Orsetti and R. Tosta: *Homogenising of 6063 alloy.* Proc. of the International Conference on Aluminium Alloys, Toyohashi, Japan (1998) 2123-2128.

[6] O. Grong: *Metallurgical modelling of welding*. Published by the Institute of Materials, 1 Carlton House Terrace, London, Sw1y5DB, 303 (1994).

[7] S. Onurlu and A. Tekin: *Effect of heat treatment on the insoluble intermetallic phases present in an AA6063 alloy*. J. Mater. Sci. **29** (1994) 1652-1655.

[8] H. Tanihata, T. Sugawara, K. Matsuda and S. Ikeno: *Effect of casting and homogenizing treatment conditions on the formation of Al-Fe-Si intermetallic compounds in 6063 Al-Mg-Si alloys*. J. Mat. Sci. **34** (1999) 1205-1210.

[9] H. J. Lamb: *The Effect of trace additions of manganese and prior heat-treatment on the structure of dilute Al-Mg-Si Alloy extrusion ingot.* Proc. Conf. Institution of Metallurgist. **3V** (1979) 4-5.

[10] J. R. Davis: *Aluminium and Aluminium Alloys*. *ASM Specialty Handbook.* Publ. ASM international. ISBN 0-87170-496-X (1993).

[11] C. M. Allen, K. A. Q. O'Reilly, B. Cantor and P. V. Evans: *Intermetallic phase selection in 1xxx Al alloys.* Progress in Materials Science **43** (1998) 89-170.

[12] L. F. Mondolfo: *Aluminium alloys: structure and properties.* Published by Butter Worths & Co Ltd, London-Boston (1976).

[13] G. Phragmen: *On the phases occupying in alloys of aluminium with copper, magnesium, manganese, iron, and silicon.* J. Inst. Metals **77** (1950) 489-552.

[14] Chr. Rømming: *Crystal structure of β-$Al_{4.5}FeSi$*. Acta Cryst. B **50** (1994) 307-312.

[15] P. Skjerpe, *Intermetallic phases formed during DC-Casting of an Al-0.25 wt Pct Fe-0.13 Wt Pct Si Alloy*. Metall. Trans. A **18** (1987) 189-200.

[16] J. G. Zheng, R. Vincent and J. W. Steeds: *Crystal structure of an orthorhombic phase in β-(Al-Fe-Si) precipitates determined by convergent-beam electron diffraction*. Phil. Mag. A **80** (2000) 493-500.

[17] A. L. Dons: *AlFeSi-particles in commercial pure aluminium*. Z. Metallkde **75** (1984) 170-174.

[18] A. Griger, V. Stefániay, A. Lendvai and T. Turmezey: *Possible modification of cast structure by continuous casting technology in AlFeSi alloys Part III: Intermetallic phases*. Aluminium **65** (1989) 1049-1056.

[19] D. J. Skinner, R. L. Bye, D. Raybould and A. M. Brown: *Dispersion strengthened Al-Fe-V-Si alloys.* Scripta Met. **20** (1986) 867-872

[20] M. Cooper: *The crystal structure of the ternary alloy AlFeSi.* Acta Cryst. **23** (1967) 1106.

[21] M. H. Mulazimoglu, A. Zaluska, J. E. Gruzleski and F. Paray: *Electron microscope study of Al-Fe-Si intermetallics in 6201 aluminum alloy*. Metall. Mater. Trans. A **27** (1996) 929-936.

[22] P. Donnadieu, G. Lapasset and T. H. Sanders: *Mangenese-induced ordering in the α-(Al-Mn-Fe-Si) approximant phase*. Philos. Mag. Lett. **70** (1994) 319-326.

[23] Y. Birol: *Formation and transformation of intermetallic particles in strip-cast Al-0.8Fe-0.6Si Alloy*. Z. Metallkd. **89** (1998) 501-506.

[24] P. Donnadieu, G. Lapasset, B. Thanaboonsombut and T. H. Sanders: *α-phase particles in 6xxx aluminium alloys*, The 4th international conference on aluminum alloys, Atlanta, Georgia, USA (1994) 668-675.

[25] D. T. L. Alexander and A. L. Greer: *Solid-state intermetallic phase transformation in 3xxx aluminium alloys*. Acta. Mat. **50** (2002) 2571-2583.

[26] H. Westengen: *Formation of intermetallic compounds during DC Casting of a commercial purity Al-Fe-Si alloy*. Z. Metallkd. **73** (1982) 360-368.

[27] T. Turmezey: *AlFe and AlFeSi intermetallic phases in aluminium alloys*. Mater. Sci. Forum. **13-14** (1987) 121-132.

[28] K. Sugiyama, N. Kaji and K. Hiraga: *Re-Refinement of α-(AlMnSi)*. Acta Cryst. C **54** (1998) 445-447.

[29] M. Cooper and K. Robinson: Acta Cryst. **20** (1966) 614.

[30] H. Tanihata, K. Matsuda and S. Ikeno: *High resolution transmission electron microscope observation of the metastable phase in an aged commercial AA6063*. Mater. Sci. Forum. **217-222** (1996) 809-814.

[31] L. Lodgaard and N. Ryum: *Precipitation of chromium containing dispersoids in AL-Mg-Si alloys*. Mat. Sci. Technol. **16** (2000) 599-604.

[32] J. E. Tibballs, J. A. Horst and C. J. Simensen: *Precipitation of α-Al(Fe,Mn)Si from the melt*. J. Mat. Sci. **36** (2001) 937-941.

[33] P. Liu and G. L. Dunlop: *Long-range ordering of vacancies in bcc α-AlFeSi*, J. Mat. Sci. **23** (1988) 1419-1414.

[34] P. Liu, T. Thorvaldsson and G. L. Dunlop: *Formation of intermetallic compounds during solidification of dilute Al-Fe-Si alloys*. Mater. Sci. Technol. **2** (1986) 1009-1018.

[35] M. Ryvola and L. R. Morris: *Examination of insoluble intermetallic phases in aluminium alloys*. Microstruct. Sci. **5** (1977) 203-208.

[36] Y. Langsrud: *Silicon in commercial aluminium alloys –what becomes of it during DC-casting?* Key Engineering Materials. **44-45** (1990) 95-116.

[37] F. Paray, B. Kulunk and J. Gruzleski: *Effect of strontium on microstructure and properties of aluminium based extrusion alloy 6061*. Mater. Sci. Technol. **12** (1996) 315-322.

[38] M. H. Mulazimoglu, A. Zaluska, F. Paray and J. E. Gruzleski: *The effect of strontium on the Mg_2Si precipitation process in 6201 aluminum alloy*. Metall. Mater. Trans. A. **28** (1996) 1289-1295.

[39] J. Langerweger: *Influence of heat treatment practice on extrudability and properties of AlMgSi Alloy sections*. In: Aluminium Technology '86, London, UK (1986) 216-222.

[40] J. van de Langkruis. *The effect of thermal treatments on the extrusion behaviour of AlMgSi alloys*. Ph.D. Thesis, University of Technology Delft, The Netherlands (2000).

[41] M. P. Clode and T. Sheppard: *Extrusion limit diagrams containing structural and topological information for AA 6063 aluminium alloy*. Mater. Sci. Technol. **9** (1993) 313-318.

[42] M. P. Clode and T. Sheppard: *Surface generation and origin of defects during extrusion of aluminium alloys.* Proc. Aluminium Technology '86, The Institute of Metals, 1 Carlton House Terrace, London SW1Y 5DB, UK (1986) 230-239.

[43] S. Zajac, L. Gullman, A. Johansson and B. Bengtsson: *Hot ductility of some Al-Mg-Si alloys.* Mater. Sci. Forum. **217-222** (1996) 1193-1198.

[44] K. E. Nilsen and P. T. G. Koenis: *Quantitative analysis of the homogenizing heat treatment by means of AlFeSi particle analysis and the effect on productivity*. In: ET 2000: Seventh International Aluminum Extrusion Technology Seminar. Chicago, USA, Aluminum Extruders Council (2000) 69-75.

[45] N. C. Parson and H. L. Yiu: *The effect of heat treatment on the microstructure and properties of 6000 Series alloy extrusion ingots,* Proc. Light Metals, Las Vegas, Nevada, USA (1989) 713-724.

[46] G. Merk and S. E. Naess: *Pick-Up Formation on Aluminium Extrusions*. Z. Metallkde **68** (1977) 683-687.

[47] T. Minoda, H. Hayakawa and H. Yoshida: *A mechanism of pick-up formation on 6063 aluminium alloy extrusions*. Mater. Sci. Techn. **7** (1998) 13-17.

[48] N. Chakraborti and H. L. Lukas: *Thermodynamic optimalization of the Mg-Al-Si Phase diagram*. Calphas **16** (1992) 79-86.

[49] D. A. Porter and K. E. Easterling: *Phase transformations in metals and alloys.* Published by Chapman & Hall, 2-6 Boundary Row, London SE1 8HN, (1992).

[50] H. Mehrer: *Diffusion in Intermetallics.* Mater. Trans. **37** (1996) 1259-1280.

[51] S. J. Rothman, N. L. Peterson, L. J. Nowicki and L. C. Robinson: *Tracer diffusion of magnesium in aluminum single crystals.* Phys. Status Solidi (b) **63** (1974) K29-33.

[52] S. I. Fujikawa: *Diffusion of magnesium in Al-Mg-Si Alloys*. Defect and Diffusion Forum **143-147** (1997) 403-308.

[53] D. Bergner and E. Cryrener: *Diffusion of impurities in Al solid solutions. Pt. 3. Diffusion of Si in Al*. Neue Hütte **18(6)** (1973) 356-361.

[54] S. Fujikawa, K. Hirano and Y. Fukushima: *Diffusion of silicon in aluminum*, Metall. Trans. A, **9A** (1978) 1811-1815.

[55] D. L. Beke, I. Gödény, I. A. Szabó, G. Erdélyi and F. J. Kedves: *On the diffusion of ^{59}Fe into aluminium and Al Mn solid solutions.* Philos. Mag. **A5** (1987) 425-443.

[56] W. B. Alexander and L. M. Slifkin: *Diffusion of solutes in aluminum and dilute aluminum alloys*. Phys. Rev. B **1** (1970) 3274.

[57] G. M. Hood: *The diffusion of iron in aluminium.* Philos. Mag. **21** (1970) 305-328.

[58] F. J. Vermolen: *Mathematical Models for Particle Dissolution in Extrudable Aluminium Alloys*. Ph.D. Thesis, University of Technology Delft, The Netherlands (1998).

[59] F. J. Vermolen and C. Vuik: *A mathematical model for the dissolution of particles in multi-component alloys*. Comput. Appl. Math. **126 (**2000) 233-25.

Chapter 2

Assessment of different techniques for quantification of α-Al(FeMn)Si and β-AlFeSi

In this chapter, several quantitative methods to determine the relative volume fraction of α-Al(FeMn)Si and β-AlFeSi, are compared and an assessment of each method is made. The methods used are: optical microscopy, scanning electron microscopy (SEM) in combination with Electron Dispersive X-ray (EDX) using polished samples, and X-Ray Diffraction (XRD) on intermetallics, extracted through selective dissolution of the Al-matrix. The highest accuracy is obtained by using SEM/EDX analysis and applying two criteria.

2.1. Introduction

In order to analyse the extrusion quality of homogenised 6xxx alloys, it is useful to have an accurate method for the quantification of the amount of α and β particles inside the material. Also, for this thesis, an accurate quantification method is an important tool for the analysis of the kinetics of the β-to-α transformation. Therefore it is of general interest to assess the accuracy of different quantification methods of the α and β intermetallics.

In the past, various techniques, such as optical microscopy [1], Electron Dispersive X-ray (EDX) analysis [2,3], X-Ray Diffraction (XRD) [4,5] and Mössbauer analysis [6] have been used to determine the concentration of the intermetallics in AA 3xxx or AA 6xxx alloys. In most analyses, however, only one method was applied and proper calibrations or use of standards were not applied. In contrast, in this study several quantitative methods are compared and an assessment of each method will be made. Studies are performed on a representative AA 6005A alloy, subjected to different heat

treatments in order to get different relative fractions of β-AlFeSi and cubic α-Al(FeMn)Si intermetallics. The methods used are optical microscopy, scanning electron microscopy (SEM) in combination with EDX, and x-ray diffraction (XRD) on intermetallics extracted through selective dissolution of the Al-matrix *i.e.* extracted using the Sibut method [7].

2.2 Experimental

2.2.1 Material and material preparation

The chemical composition of the AA 6005A alloy was 0.83 wt.% Si, 0.27 wt.% Fe, 0.70 wt.% Mg, 0.18 wt.% Mn and 0.02 wt.% Zn. Other elements were present in amounts smaller than 0.01 wt.%. The material was DC-cast as a billet with a diameter of 254 mm. All samples were taken from a region of 20 mm to 30 mm away from the edge of the billet in order to get comparable starting microstructures and compositions.
Samples with different relative α-fractions were prepared by homogenising at 540°C for times up to 32 h. A range of relative α-fractions between approximately 0.05 and 0.75 (with respect to the total volume of α-Al(FeMn)Si and β-AlFeSi) was obtained.

For calibration purposes three reference samples labelled A, B1 and B2 were prepared. Sample A was homogenised at an elevated temperature of 590°C for 32 h. In this sample all β-AlFeSi was transformed to α-Al(FeMn)Si. Sample B1 was an as cast sample. In this sample mainly β-AlFeSi, a trace of α-Al(FeMn)Si and some Mg_2Si precipitates, formed during casting, were present. Sample B2 was homogenised at 540°C for 20 min. In this sample all Mg_2Si precipitates formed during casting were dissolved, while the transformation from *β*-AlFeSi to α-Al(FeMn)Si was negligible.

2.2.2 Experimental techniques

After polishing the samples were investigated using an Olympic BX60M microscope equipped with an oil immersion lens. On each sample 10 micrographs were recorded randomly over a sample area of approximately 100 mm^2. In optical micrographs the Al matrix appears very light grey whereas the intermetallics are dark grey. The contrast difference between the α-Al(FeMn)Si and the β-AlFeSi was too small to be able to distinguish the phase type by an automated system. Therefore only the particle shape has been used for quantitative analysis. A digital image analysis system was used to measure the particle area A and aspect ratio R of 30 randomly selected particles in each micrograph.

SEM in combination with EDX was used on polished samples, with a relatively high accelerating voltage of 20 kV to improve the contrast between the intermetallics (bright) and the matrix (grey). Analogously to the optical measurements, the contrast between α-Al(FeMn)Si and β-AlFeSi was too low to be able to distinguish the phases in a reliable way. Therefore for quantification purposes only the particle shape and particle composition were used. Spot size during the EDX measurements was approximately 4 μm, which was in most cases larger than the size of the intermetallics. Therefore also some Al x-ray signal from the matrix was detected. 16 regions of 50 μm × 50 μm, were selected randomly on a polished plane of approximately 100 mm^2. In each region a maximum of 20 particles was detected. For each particle the particle area A, the aspect ratio R, and the relative x-ray intensities of Al, Mg, Si, Mn and Fe were measured. The relative intensity of an element, for example Mn, is defined by

$$I_{Mn} = I'_{Mn} / (I'_{Al} + I'_{Fe} + I'_{Mn} + I'_{Mg} + I'_{Si}) \tag{2.1}$$

where I'_{Al}, I'_{Fe}, I'_{Mn}, I'_{Mg} *and* I'_{Si} are the intensities of the characteristic peaks in the EDX pattern. These relative intensities are closely correlated with the local concentrations of the elements. In order to eliminate particles which might be incorrectly identified as α-Al(FeMn)Si or β-AlFeSi intermetallics, particles for which the x-ray intensities of minor elements such as Ti, V, Cr, Co, Ni, Cu and Pb were higher than 10 % of the sum of the Si, Mn and Fe intensities, are rejected. Also, particles with x-ray intensities of Si, Mn and Fe below the noise level (0.5 % of the Al intensity) are eliminated. On average two percent of the detected particle area is rejected by this procedure. The non-rejected particles were considered to be α-Al(FeMn)Si or β-AlFeSi intermetallics.

For the x-ray diffraction experiments the intermetallic particles in the material were extracted from the metallic matrix using the Sibut method, developed by Sintef, Norway [7]. During the extraction a sample of about 0.35 g is processed by dissolving the Al matrix without chemically attacking the intermetallics. The intermetallics (~2 mg) were then collected on a Teflon filter with pore size of 0.4 μm. After extraction the particles were wetted with acetone and gently scraped from the filter onto a glass plate using a scalpel. When dried, the intermetallics were milled in some ethanol for about 5 min. After milling and then drying the intermetallics were dispersed in propanol and transferred to a glass tube and its content was ultrasonically stirred for one minute, leading to a fine suspension of the intermetallics. The suspension was poured into a copper cylinder with an internal diameter of 21 mm which is put on a Si substrate. The Si wafer was heated at 40 ^{o}C and the propanol evaporated in a few hours leaving behind

a thin layer of the extracted intermetallics. The Si wafer was weighed before and after the deposition to give the weight of the intermetallics.

X-ray diffraction measurements on the prepared powder samples were performed with a Siemens D5005 diffractometer, equipped with a Cu_α source. For all samples, diffraction patterns were determined with diffraction angles 2θ ranging from 15° to 50°. Figure 2.1 shows the measured and calculated x-ray diffraction patterns of α-Al(FeMn)Si and β-AlFeSi intermetallics. The calculated pattern was based on crystallographic data for α-Al(FeMn)Si and β-AlFeSi [8,9], and a random orientation. The measured peak positions of the diffraction patterns correspond well to the calculated positions. However, measured peak intensities differ from the intensities calculated. This might be due to a preferred orientation of the intermetallics on the substrate. The differences in intensities are largest for the β-AlFeSi intermetallic, which indeed has a planar morphology, promoting alignment on the substrate.

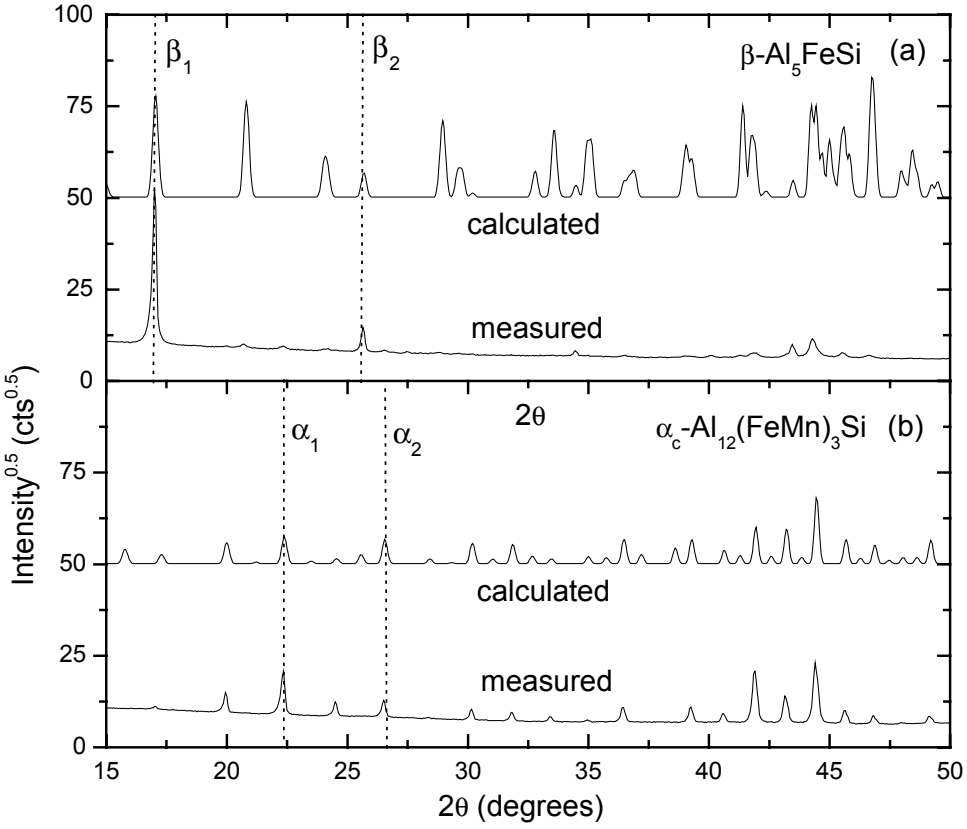

Figure 2.1 (a) Diffraction pattern of β-AlFeSi (reference sample B2). (b) Diffraction pattern of α-Al(FeMn)Si (reference sample A). The peaks used for analysis, are indicated in the figure.

The integrated intensity was determined for two main characteristic peaks in the diffraction pattern, $J_{\alpha 1}$ and $J_{\beta 1}$, which correspond to the {3 1 0} reflection (lattice parameter: 0.3981 nm) in α-Al(FeMn)Si and to the (0 0 8) reflection (lattice parameter: 0.5208 nm) in β-AlFeSi, respectively. To investigate the effect of orientation of the intermetallics on the Si-substrate, the peak intensities of secondary peaks $J_{\alpha 2}$ and $J_{\beta 2}$ were also measured. These peaks correspond to the {3 2 1} reflection (0.3360 nm) in α-Al(FeMn)Si and to the (1 1 7) reflection (0.3469 nm) in β-AlFeSi, respectively.

2.2.3 Quantification of the relative α-Al(FeMn)Si and β-AlFeSi fraction

A. Analysis by optical microscopy or SEM

Since the optical method cannot distinguish between the colour of β-AlFeSi and α-Al(FeMn)Si intermetallics, the discrimination between α-Al(FeMn)Si and β-AlFeSi is made only from the aspect ratio *R*. The aspect ratio is defined as the maximum length of the particle divided by the thickness. The plate-like β-AlFeSi intermetallics have a high mean aspect ratio of about 10, whereas the spheroidised α-Al(FeMn)Si intermetallics have a mean aspect ratio of near unity. We define a critical aspect ratio R_{crit}. If $R > R_{\text{crit}}$, the particle is classified as a β-AlFeSi particle and otherwise as an α-Al(FeMn)Si particle.

Discrimination between β-AlFeSi and α-Al(FeMn)Si particles and quantification was also performed with an automated SEM system by observing the following parameters: aspect ratio *R*, Mn intensity I_{Mn}, and S-ratio defined as $S = (I_{Fe} + I_{Mn})/I_{Si}$. Discrimination on aspect ratio was performed similarly to that in optical microscopy. Furthermore, since Mn is present in α-Al(FeMn)Si and not in β-AlFeSi, discrimination was possible on the basis of the measured x-ray intensity I_{Mn}. We now define a critical intensity $I_{crit\,Mn}$. If $I_{Mn} < I_{crit\,Mn}$, the particle is considered to be a β-AlFeSi particle and otherwise to be an α-Al(FeMn)Si particle. Finally, the S-ratio of each particle is monitored. The S-ratio is ~3 for α-Al(FeMn)Si and ~1 for β-AlFeSi particles. We now define a critical intensity S_{crit}. If $S < S_{crit}$, the particle is classified as a β-AlFeSi particle and otherwise as an α-Al(FeMn)Si particle.

Having specified the classification criteria we can now analyse the degree of transformation. The true relative intermetallic α-Al(FeMn)Si volume fraction (f_α) is defined as

$$f_\alpha \equiv \frac{v_\alpha}{v_\alpha + v_\beta} \tag{2.2}$$

where v_α and v_β are the total volumes occupied by the α-Al(FeMn)Si and the β-AlFeSi particles respectively. The true relative fraction of β-AlFeSi, f_β, is equal to $f_\beta = 1 - f_\alpha$.

Now we want to get a close estimate of the true relative α-fraction f_α from the data provided by the measurements. To do so, first an apparent relative α-fraction $f_{\alpha\ \mathrm{apparent}}$ is determined by

$$f_{\alpha\ apparent} = \frac{A_\alpha}{A_\alpha + A_\beta}, \tag{2.3}$$

where A_α and A_β are the total measured areas of allocated α-Al(FeMn)Si and β-AlFeSi particles as found by application of one of the criteria. Since the allocation of α-Al(FeMn)Si or β-AlFeSi depends on the precise values selected for R_{crit}, $I_{Mn\ crit}$ or S_{crit}, the value of $f_{\alpha\ apparent}$ depends on the critical value and will generally differ from the true relative α-fraction f_α. The error is defined as:

$$\Delta f_\alpha^{app} = | f_\alpha - f_{\alpha\ apparent} | \tag{2.4}$$

To get an accurate estimate of the true α-fraction transformed, the following procedure was applied. First the distributions of parameters R, I_{Mn} and S were measured for the calibration samples containing purely α-Al(FeMn)Si or purely β-AlFeSi. The values for the criteria R_{crit}, $I_{Mn\ crit}$ or S_{crit} for the allocation of α-Al(FeMn)Si and β-AlFeSi were chosen such that for a hypothetical 50%-50% mixture of the reference samples the fraction α-Al(FeMn)Si incorrectly assigned to be β-AlFeSi equals the fraction β-AlFeSi incorrectly assigned to be α-AlFeSi. For such values of the criteria, a minimised error of the apparent fraction at a true fraction of f_α=0.5 is obtained. For a sample with an arbitrary ratio of β-AlFeSi to α-Al(FeMn)Si the α-Al(FeMn)Si fraction closest to the true relative fraction f_α is given by:

$$f_{\alpha\ meas} = \frac{f_{\alpha\ apparent} - 1 + c_\beta}{c_\alpha + c_\beta - 1}, \tag{2.5}$$

where c_α is the fraction of α-Al(FeMn)Si particles allocated correctly for a reference sample of purely α-Al(FeMn)Si, and c_β is the fraction of β-AlFeSi particles allocated correctly for a reference sample of purely β-AlFeSi. In this procedure the determined relative fraction, $f_{\alpha\ meas}$, is corrected for errors due to incorrect allocation, and therefore only the statistical error remains. The total error is expressed by:

$$\Delta f_\alpha = | f_\alpha - f_{\alpha\, meas} | = \left| \frac{\Delta f_\alpha^S}{c_\alpha + c_\beta - 1} \right| \tag{2.6}$$

where Δf_α^S is the statistical error in the apparent relative α-fraction. Note that in the case when all particles are allocated correctly, c_α and c_β will be unity. In general c_α and c_β values approaching 1 are an indication of non-overlapping distributions and secure assignments. For the current procedure where errors are cancelled at $f_\alpha = f_\beta = 0.5$, c_α is equal to c_β.

B. Analysis by x-ray diffraction

From the diffraction patterns, the integrated peak intensities $J_{\alpha 1}$ and $J_{\beta 1}$ were determined (see Section 2.2) and the determined relative fraction $f_{\alpha\, apparent}$ is derived by [10]:

$$f_{\alpha\, apparent} = \frac{J_{\alpha 1} / R_{\alpha 1}}{J_{\alpha 1} / R_{\alpha 1} + J_{\beta 1} / R_{\beta 1}} = \frac{J_{\alpha 1}}{J_{\alpha 1} + \xi J_{\beta 1}} \tag{2.7}$$

where $R_{\alpha 1}$ and $R_{\beta 1}$ are the relative intensity coefficients of the $J_{\alpha 1}$ and $J_{\beta 1}$ peaks respectively. ξ is a calibration factor, defined by $\xi = R_{\alpha 1} / R_{\beta 1}$. In this case there are no allocation problems, and therefore $f_{\alpha\, meas} = f_{\alpha\, apparent}$.

The constant ξ was calibrated with a standard, prepared from pure α-Al(FeMn)Si and β-AlFeSi intermetallics and mixtures. Intermetallics of reference samples A and B2 were extracted and weighed by a Satorius balance, mixed and prepared on a silicon wafer in a similar procedure as described in Section 2.2. Weights were 2.17 mg α-Al(FeMn)Si and 1.78 mg β-AlFeSi intermetallics respectively; and taking into account the densities of both phases [11], a value of f_α equal to 0.53 was obtained. Applying equation (2.7) leads to $\xi = 0.18$.

2.3. Results

2.3.1 Optical and SEM micrographs

Figure 2.2 shows the optical micrographs of three samples. The first is reference sample B1, which contains β-AlFeSi intermetallics and β-Mg_2Si precipitates, mainly precipitated onto the surface of the β-AlFeSi; the second is reference sample B2, which still contains the β-AlFeSi intermetallics but the β-Mg_2Si precipitates are now dissolved; and the third is reference sample A, which contains the α-Al(FeMn)Si

intermetallics. The transformation from β-AlFeSi to α-Al(FeMn)Si, during which the β-AlFeSi phase breaks up into beads of rounded α-Al(FeMn)Si particles can be clearly seen. Also, some α-Al(FeMn)Si particles are nucleated in the matrix with sizes smaller than 0.5 μm, but these were not analysed in this study. Similar features are visible in the SEM micrographs in Figure 2.3.

Figure 2.4 presents two SEM images of the intermetallics obtained after extraction by the Sibut method, showing interconnected plate-like β-AlFeSi intermetallics in the as cast structure (Figure 2.4a) and the transformed structure after homogenisation (Figure 2.4b). Clearly the coherent β-AlFeSi structure lost its coherency during the transformation to α-Al(FeMn)Si as analysed in more detail in Chapter 5.

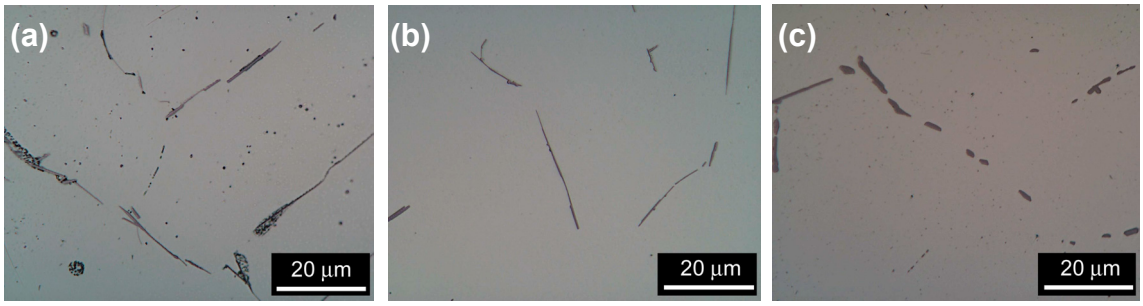

(a) (b) (c)

Figure 2.2 Optical micrographs. (a) Reference sample B1, as cast. (b) Reference sample B2, slightly homogenised. (c) Reference sample A, fully homogenised.

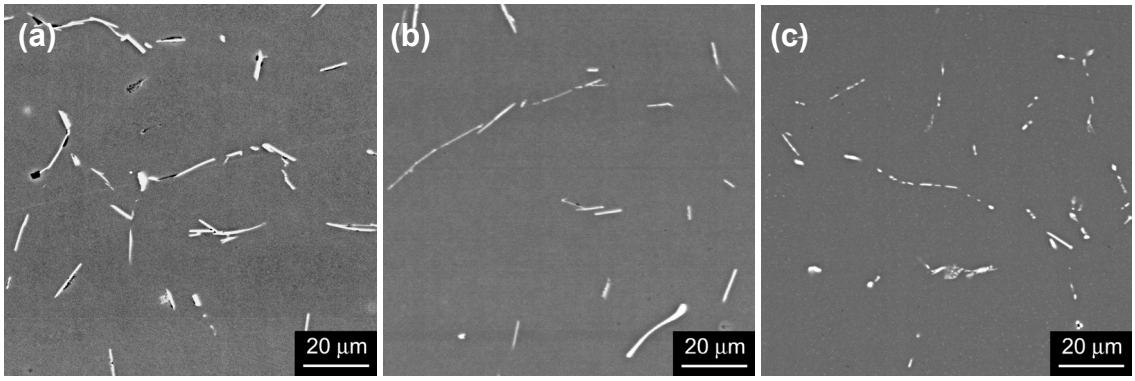

(a) (b) (c)

Figure 2.3 SEM micrographs. (a) Reference sample B1, as cast. (b) Reference sample B2, slightly homogenised. (c) Reference sample A, fully homogenised.

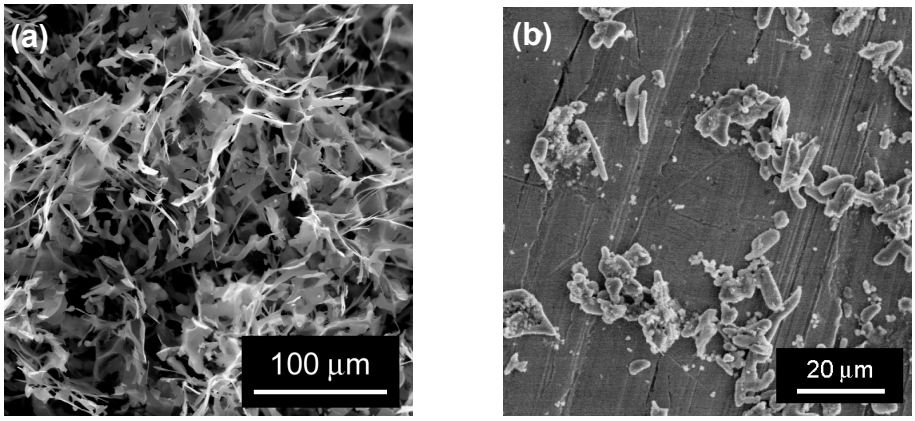

Figure 2.4 (a) SEM image of extracted β-AlFeSi intermetallics from reference sample B1. (b) SEM image of extracted α-Al(FeMn)Si intermetallics from reference sample A.

2.3.2 Quantification by optical microscopy and SEM

Figure 2.5 presents the results of the error analysis, based on the aspect ratio of SEM data, obtained for the reference samples A and B1. Plotted is the absolute value of the error of the apparent relative α fraction, Δf_α^{app}, made by incorrect allocation of α-Al(FeMn)Si or β-AlFeSi particles, versus the critical aspect ratio R_{crit}. Let us consider a critical aspect ratio $R_{crit} = 3$ for sample A (curve a), which contains only α-Al(FeMn)Si particles. This leads to a measured relative α-fraction of $f_{\alpha\,\mathrm{meas}} = 0.6$ and therefore $\Delta f_\alpha^{app} = 0.4$. For larger values for R_{crit}, more particles are counted as α-Al(FeMn)Si particles and Δf_α^{app} will be reduced. A contrasting curve (b), with an opposite trend is found for reference sample B1.

It is clear that increasing the chosen value of R_{crit} reduces the error, made by incorrect allocation, in $f_{\alpha\,meas}$ in α-Al(FeMn)Si-containing specimens, whereas at the same time it increases the error in $f_{\alpha\,meas}$ in β-AlFeSi containing specimens. Therefore the best compromise is offered by a value for R_{crit} which equalises the errors of the α-Al(FeMn)Si and β-AlFeSi containing specimens, and thus minimises the error (see curve (c)) of a hypothetical specimen which contains equal volume fractions of α-Al(FeMn)Si and β-AlFeSi particles. Curve (c) demonstrates that a minimised Δf_α^{app} is found for $R_{crit} = 3.7$, corresponding to $c_\alpha = 0.75$. Similar curves, also based on aspect ratio, were obtained after analysis of optical data. In this case a minimised Δf_α^{app} was found for $R_{crit} = 3.5$, corresponding to $c_\alpha = 0.75$. The close similarity of the R_{crit} values is an indication of the stability of the procedure and a comparable instrumental error.

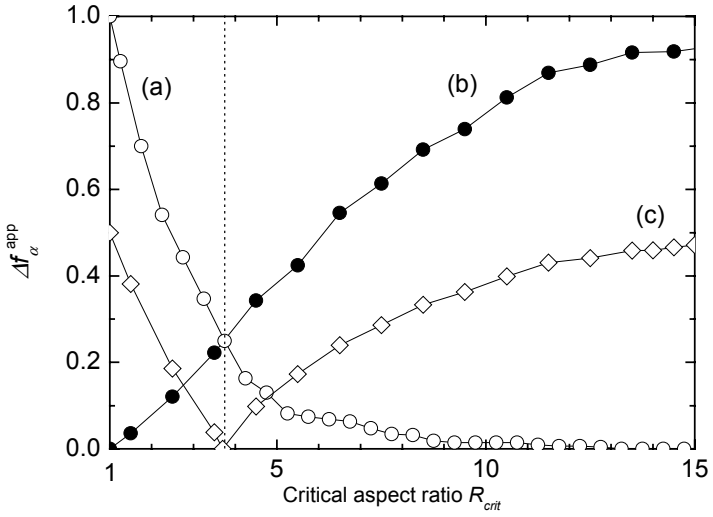

Figure 2.5 Absolute error of $f_{\alpha\ apparent}$, made by incorrect allocation of α-Al(FeMn)Si or β-AlFeSi particles, as a function of the critical aspect ratio in SEM measurements. (a) Reference sample A (mainly α-Al(FeMn)Si particles); (b) Reference sample B1 (mainly β-AlFeSi); (c) A hypothetical mixture (f_α=0.5). The dotted line indicates the optimal R_{crit}.

Figure 2.6 presents the results of the SEM/EDX analysis, where Δf_α^{app} is plotted as a function of $I_{Mn\ crit}$. Curve (a) presents the results for reference sample A. When $I_{Mn\ crit}$ increases, more particles are incorrectly assigned to be β-AlFeSi, and the error increases. Curve (b) of reference sample B1 shows an opposite trend. In the B1 sample an appreciable Mn signal is still detected even at large values of I_{Mn}. This trend is ascribed to some large α-Al(FeMn)Si particles which were present in the as-cast condition. Curve (c) shows the calculated error Δf_α^{app} for a (hypothetical) specimen which contains equal amounts of α-Al(FeMn)Si and β-AlFeSi. A minimised Δf_α^{app} is found for $I_{Mn\ crit} = 9\times10\text{-}3$, corresponding to $c_\alpha = 0.78$.

Figure 2.7a shows relative x-ray intensities I_{Fe} and I_{Si} versus I_{Al} of particles in reference sample B1. Data points are scattered, which is attributed to the influence of β-Mg_2Si particles present in sample B1 and situated at the boundaries of the β-AlFeSi particles. In order to eliminate this effect, only those measurements for which $I_{Mg} < 5\times10\text{-}3$ were selected to build Figure 2.7b. This data set was also used in all other analyses in this article. It clearly shows that the ratio of I_{Fe} and I_{Si} is approximately unity, which corresponds to the β-Al_5FeSi stoichiometry. Figure 2.7c shows the relative intensities $I_{Fe} + I_{Mn}$ and I_{Si} of reference sample A. The ratio between $I_{Fe} + I_{Mn}$ and I_{Si} is close to three, which corresponds to the α-$Al_{12}(FeMn)_3Si$ stoichiometry.

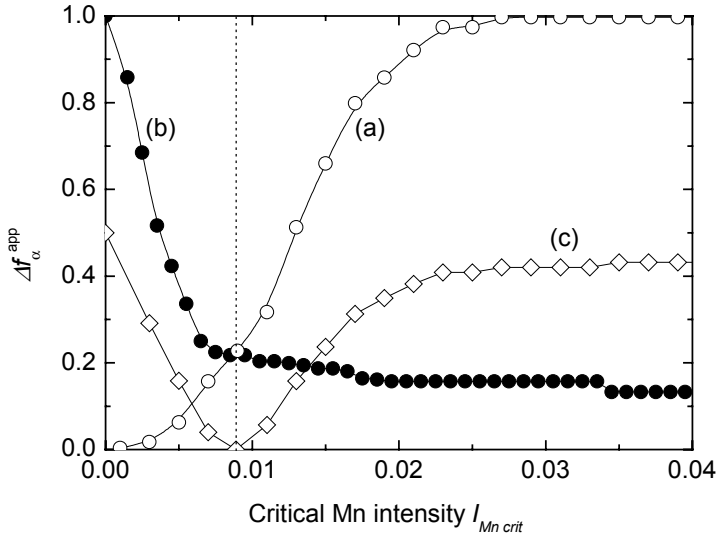

Figure 2.6 Absolute error of $f_{\alpha\ apparent}$, made by incorrect allocation of α-Al(FeMn)Si or β-AlFeSi particles, as a function of critical Mn intensity $I_{Mn\ crit}$. (a) Reference sample A (mainly α-Al(FeMn)Si particles); (b) Reference sample B1 (mainly β-AlFeSi); (c) A hypothetical mixture (f_α=0.5). The dotted line indicates the optimal $I_{Mn\ crit}$.

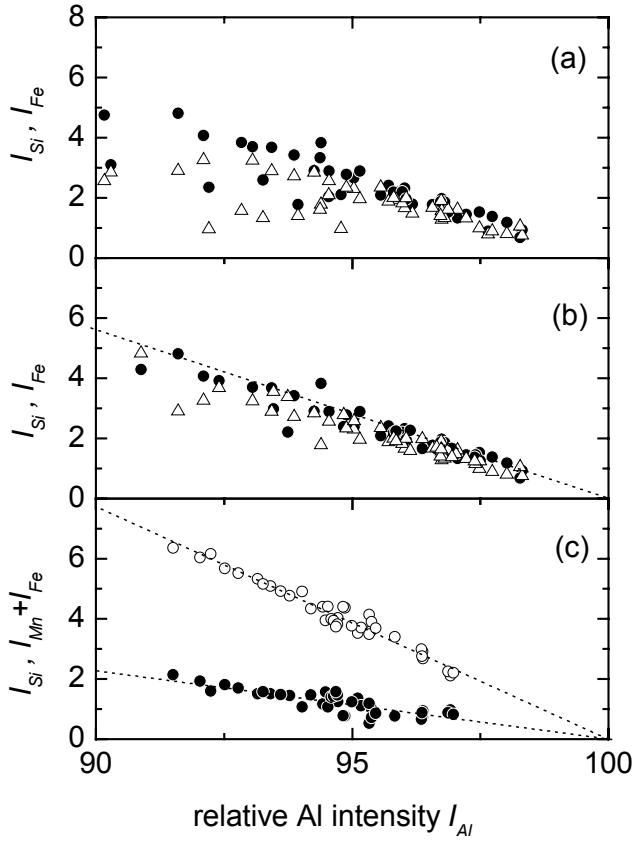

Figure 2.7 Assembly of EDX measurements on (a) an as cast sample, B1; (b) an as cast sample, B1, where measurements on particles which contain Mg are rejected; (c) an fully homogenised sample, A. ●, Si; ○, Fe ; △, Fe+ Mn.

Figure 2.8 presents the results of the SEM/EDX analysis, based on the measured S-ratio. The value Δf_{α}^{app} is plotted as a function of S_{crit}. Curve (a) presents the results for reference sample A. Curve (b) corresponds to reference sample B1. Curve (c) shows the calculated error Δf_{α}^{app} for a (hypothetical) specimen which contains equal amounts of α-Al(FeMn)Si and β-AlFeSi. It shows that a minimised Δf_{α}^{app} is found for $S_{crit} = 1.8$, corresponding to c_{α}=0.91.

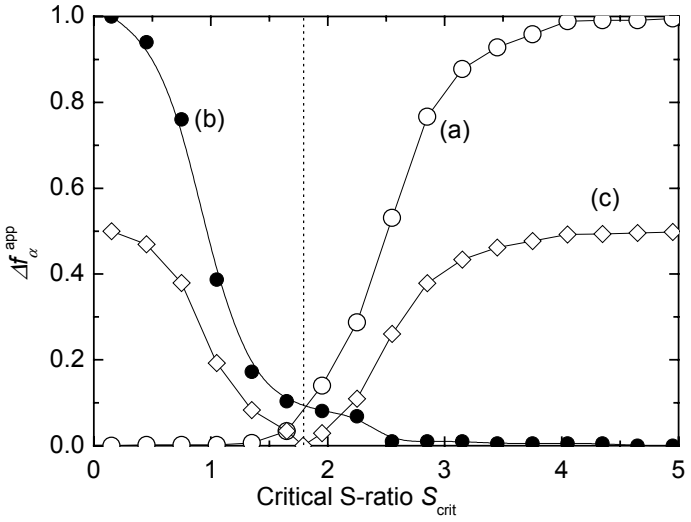

Figure 2.8 Absolute error of $f_{\alpha\ apparent}$, made by incorrect allocation of α-Al(FeMn)Si or β-AlFeSi particles, as a function of the critical S-ratio S_{crit}. (a) Reference sample A (mainly α-Al(FeMn)Si particles); (b) Reference sample B1 (mainly β-AlFeSi); (c) A hypothetical mixture (f_{α}=0.5). The dotted line indicates the optimal S_{crit}.

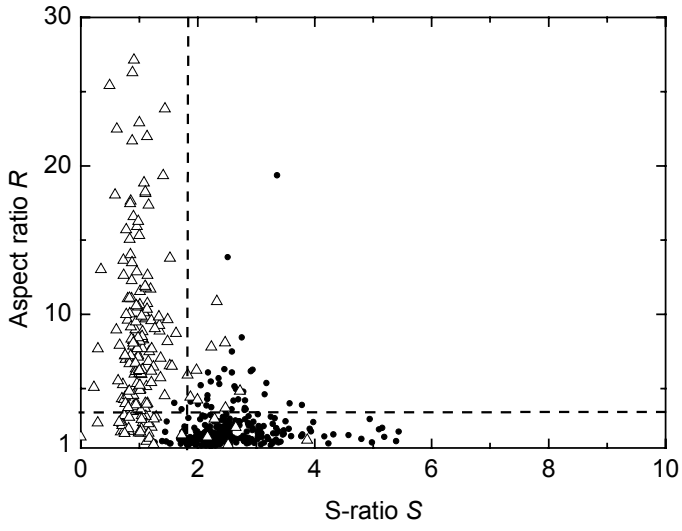

Figure 2.9 A plot of the aspect ratio (SEM) and S-ratio (SEM/EDX) of a collection of individual particles of reference samples: ●: α-Al(FeMn)Si, △: β-AlFeSi.

From the values of c_α obtained via the four techniques (optical, SEM, SEM.EDX-$I_{Mn\ crit}$, SEM/EDX S-ratio) it can be deduced that discrimination by the S-ratio is rather accurate whereas discrimination by the aspect ratio is less reliable. This is also shown in Figure 2.9 where the aspect ratio and S-ratio of individual particles of reference samples A and B1 are plotted.

2.3.3 Quantification using combined methods in SEM analysis

In Section 3.2 it was seen that single criteria may be applied in order to discriminate between α-Al(FeMn)Si and β-AlFeSi intermetallics, but that allocation is subject to a certain error. It might likely that a combination of methods in principle will provide a better strategy for discrimination between α-Al(FeMn)Si and β-AlFeSi intermetallics. In such a procedure the first classification is on one parameter and then data close to the cut off criterion are re-evaluated on the basis of an overruling second criterion. The principle is demonstrated in Figure 2.10a. For reference sample A a combination of S and I_{Mn} are taken as the first and second criteria respectively. As indicated in Figure 2.10a, this method leads to a relative fraction Δf_1, initially incorrectly assigned and a relative fraction Δf_2 to be subjected to the second criterion. In Figure 2.10b the error Δf_α^{app} is given as a function of window size for reference samples A and B1. The value of Δf_α^{app} at window size zero corresponds with that of using only the S-ratio as discrimination, whereas the values of Δf_α^{app} for large window size approach those found after using only the second criterion as discrimination. An optimum window size ($2\cdot\Delta S$=0.35) is found for which Δf_α^{app} becomes minimal.

Table 2.1 summarises c_α and c_β values obtained by this approach for several combinations of criteria. This table indicates that the combined method of S-ratio as first criterion, and Mn intensity I_{Mn} as second criterion, gives the smallest error.

Table 2.1 The various combined methods in SEM/EDX analysis. Indicated are optimum window size and c_α and c_β values.

First criterion	second criterion	optimum window size	c_α	c_β
Aspect ratio	Mn intensity	$2\cdot\Delta R=3$	0.81	0.84
Aspect ratio	S-ratio	$2\cdot\Delta R=3$	0.87	0.88
Mn intensity	Aspect ratio	$2\cdot\Delta I_{Mn}=0.004$	0.80	0.79
Mn intensity	S-ratio	$2\cdot\Delta I_{Mn}=0.004$	0.83	0.79
S-ratio	Aspect ratio	$2\cdot\Delta S=0.35$	0.93	0.90
S-ratio	Mn intensity	$2\cdot\Delta S=0.35$	0.94	0.91

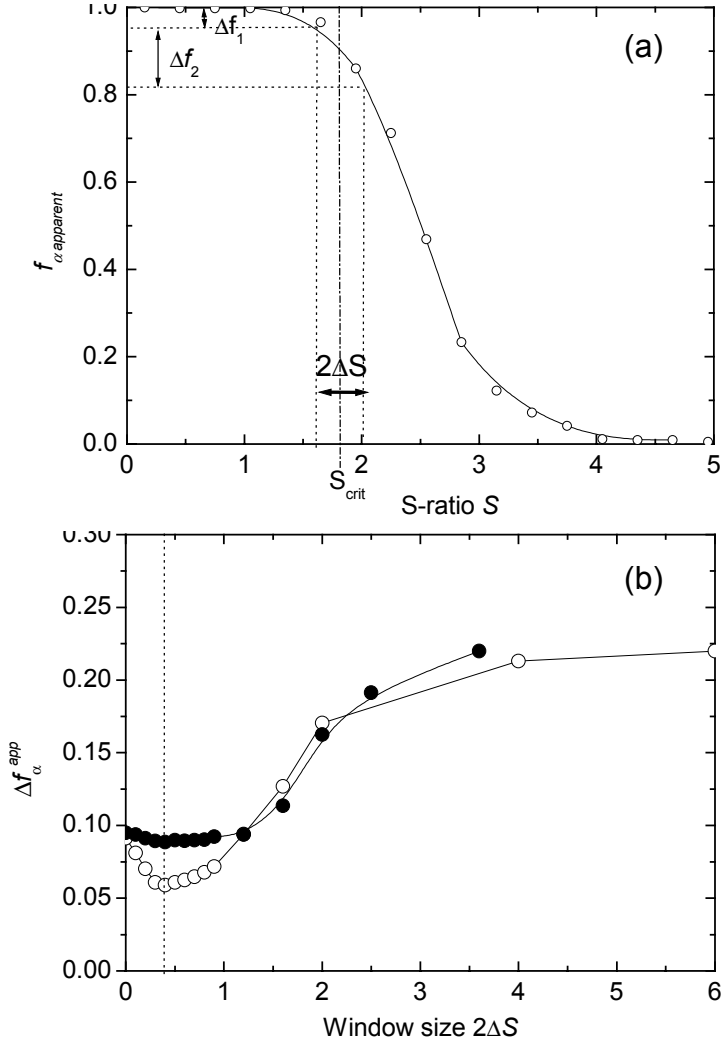

Figure 2.10 (a) Principle of combined method, where allocation by the S-ratio is the first method and data falling in window 2Δ*S* will be selected by a second method. The figure presents the relative fraction c_α determined in reference sample A as a function of S_{crit}. (b) Error, made by incorrect allocation of α-Al(FeMn)Si and β-AlFeSi particles, as a function of window size 2Δ*S*, where allocation by Mn is the second method.

2.3.4 Quantification using x-ray diffraction

The measured x-ray intensities for various samples with different relative volume fractions f_α are given in Figure 2.11. In Figure 2.11a it is seen that the ratios of β_2 and β_1 intensities reflected from β-AlFeSi particles scatter around an average value. The same is observed for the ratios of α_2 and α_1 intensities reflected from α-Al(FeMn)Si particles (Figure 2.11b), but the scatter is considerably lower. The high scatter observed for the β-AlFeSi particles is attributed to differences in the preferred average orientation of the β-AlFeSi particles on the Si substrate after the extraction procedure. Owing to the plate-like morphology the orientation effects are strong, and even after careful extraction and

milling there are variations in average orientation. This effect is much less for α-Al(FeMn)Si particles, which are more globular. As indicated in Figure 2.11a, variations of 25% of the intensity of the major β1 peak are found, leading to a maximum variation of the determined relative α-fraction of Δf_α =0.13. This is a possible source of error in the quantification.

2.4 Discussion

In Section 3.2 it was shown that α-Al(FeMn)Si and β-AlFeSi intermetallics can be discriminated by using two different methods (optical or SEM/EDX) and observing certain characteristics of the particles (aspect ratio and/or x-ray intensities such as Fe, Mn, Si, Mg and Al). Figure 2.8 shows that discrimination is the most accurate when observing the S-ratio defined as the ratio of the Fe plus Mn x-ray intensities and the Si x-ray intensity. For the quantification a considerable improvement is obtained by measuring reference samples containing known relative volume fractions of α-Al(FeMn)Si and β-AlFeSi. This allows determination of the values of c_α and c_β and the use of equation (2.5). Accuracy is further improved in SEM/EDX analysis when a combined method is applied, such as described in Section 3.3. Values of c_α and c_β then approach unity, and according to equation (2.6) error Δf_α becomes smaller and is primarily determined by statistical errors. In Section 3.4 x-ray diffraction performed on the extracted intermetallics was applied. This technique requires calibration using reference samples. The combined use of these techniques in combination with the calibration procedures applied has not been previously reported in the literature, and this quantification study provides a strong improvement when compared with earlier work [1-5]. However, in this study certain experimental factors are ignored. These factors and the effects they may have on the quantification will be discussed in the following section.

2.4.1 Accuracy considerations

Despite the high accuracy obtained by applying Eqs (2.5) and (2.7) some errors are not accounted for. A first type of inaccuracy is induced by particles being in intimate contact, which may occur for instance when an α-Al(FeMn)Si particle grows on the surface of a β-AlFeSi intermetallic [12]. Such a two-phase particle will be allocated as either a purely α-Al(FeMn)Si or a purely β-AlFeSi particle in the optical or SEM analysis. Another type of inaccuracy may be found with the discrimination of the intermetallics using the Mn x-ray intensity. Discrimination is based on whether Mn is present (α-Al(FeMn)Si) or not present (β-AlFeSi) in the particle, but reference sample A contained particles in which Mn levels were present after long diffusion times. In the

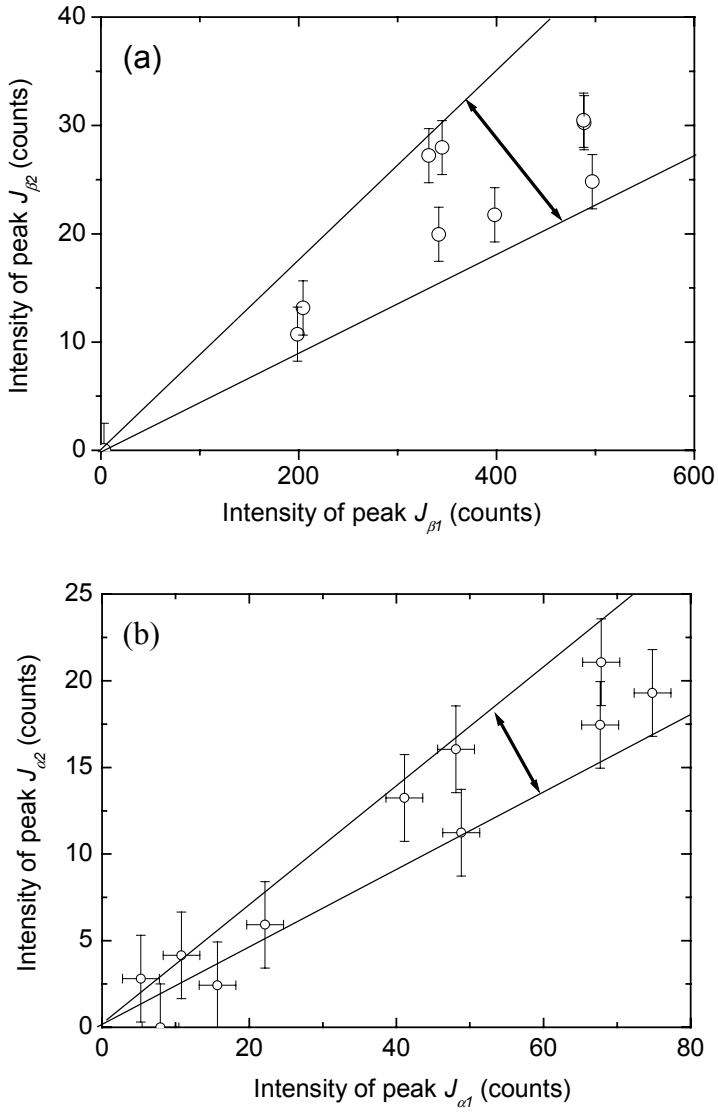

Figure 2.11 XRD measurements of several specimens containing different relative volume fractions of α-Al(FeMn)Si. Intensities of (a) peaks β_1 and β_2; (b) peaks α_1 and α_2. Lines indicate maximum and minimum linear dependence between $J_{\beta 1}$ and $J_{\beta 2}$, and $J_{\alpha 1}$ and $J_{\alpha 2}$.

beginning of the transformation, Mn levels in the α-Al(FeMn)Si particles are expected to be lower, which increases the possibility of a wrong assignment of such particle. Another type of inaccuracy is found in the analyses using particle extraction and XRD. X-ray intensity depends on orientation, and the average orientation in a particular sample is somewhat influenced by the preparation technique. The scatter which results was shown in Figure 2.11. Finally, in the optical and SEM analyses it is assumed that reference samples B1 and B2 contain only β-AlFeSi intermetallics. This is not fully correct since the XRD measurements indicated that in these samples about 6% relative

volume fraction of α-Al(FeMn)Si was present. Apart from the inaccuracies mentioned above, errors may find their origin in limited counting statistics. Considering all these effects, we estimate the error Δf_α as follows: measuring the aspect ratio (both optical and SEM), Δf_α = 0.15; using XRD, Δf_α = 0.13; measuring the Mn x-ray intensity (SEM), Δf_α = 0.07; measuring the S-ratio (SEM), Δf_α = 0.06; and using the combined method of S-ratio as first criterion and Mn x-ray intensity as second criterion (SEM), Δf_α = 0.05. We conclude that use of the combined method, although leading to the best allocation of particles, gives only a marginal improvement compared to the separate Mn x-ray intensity and S-ratio methods. We also conclude that the values of Δf_α are rather independent of the relative volume fraction.

2.4.2 Comparison of the analysis results in a transformation experiment

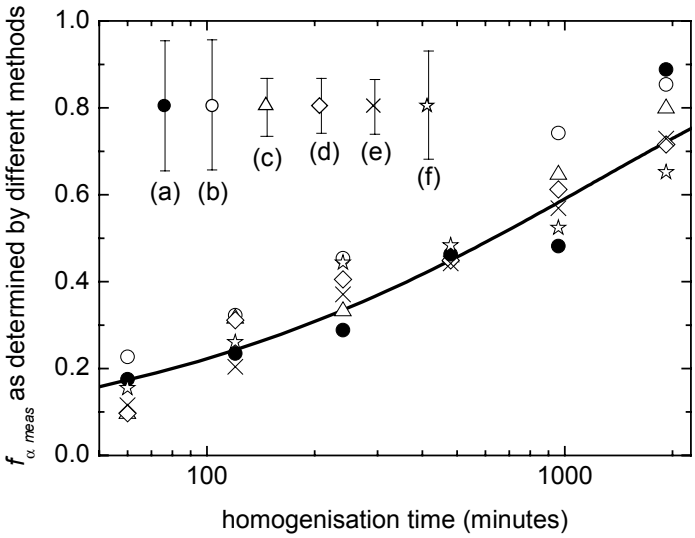

Figure 2.12 Quantitative determination of $f_{\alpha\ meas}$ by (a)●, aspect ratio (optical measurements); (b)○, aspect ratio (SEM measurements); (c) △, Mn x-ray intensity (SEM/EDX); (d) ◇, S-ratio (SEM/EDX); (e) ×, combined method of S-ratio and Mn x-ray intensity. (f)☆, x-ray diffraction. The curve gives an Avrami fit through data points ×. All presented samples were homogenised at 540°C for different times.

Figure 2.12 shows the relative volume fractions of α-Al(FeMn)Si, determined for all techniques applied, during a homogenisation treatment at a fixed temperature of 540°C. During such a treatment a transition from β-AlFeSi to α-Al(FeMn)Si takes place. All methods show a similar trend. In the figure error bars indicate the maximum error of each technique, estimated in the previous section. From the figure it appears that the individual data points fall within these errors. The line in the figure is an Avrami fit of

the data obtained with the best combined method (first criterion: S-ratio; second criterion: Mn x-ray intensity). For the Avrami fit the equation $f_{\alpha\,meas}$= 1-exp(-kt^n) was used [13], with the coefficients k=0.020 and n=0.55, where t is the homogenisation time in minutes. When we apply the Avrami analysis to a particular technique, the transformation rates found do not differ much for the various methods. Important for industrial practice is the time when the transformation is nearly - about 80-90% - completed. In Figure 2.12 it is seen that some methods, including those based upon aspect ratio, seem to overestimate the amount of α-Al(FeMn)Si and therefore underestimate the minimum homogenisation time needed.

2.4.3 Application to other 6xxx alloys

All analyses were performed on an AA 6005A alloy and the results given apply to this alloy. However, we think all the methods can also be used for other 6xxx alloys (possibly with some modifications) although the amount, size, morphology and chemical composition of the intermetallic phases may alter with alloy composition. The amount of intermetallics will affect the counting statistics in all methods in a similar way. The size of the intermetallics will not have a great influence on any technique. Moreover, the size of the β-AlFeSi phase is rather constant in industrial alloys. The aspect ratio of the β-AlFeSi phase will vary to some extent from one alloy to the other. Such variation influences the allocation potential between β-AlFeSi and α-Al(FeMn)Si intermetallics. The composition of the α-Al(FeMn)Si intermetallics may differ due to the exchange of Mn by Fe. Discrimination based on Mn x-ray intensity will be strongly influenced by this effect, whereas the discrimination on the basis of S-ratio will remain unchanged. In summary, size, morphology and chemical composition of the intermetallics will not have an appreciable influence on the analyses, based on S-ratio or particle extraction and XRD. Quantification using these methods will be rather independent of the condition of the β-AlFeSi and α-Al(FeMn)Si intermetallics and of the particular alloy. Therefore, it is assumed that these methods are directly applicable to other 6xxx alloys, once calibration with reference samples of known composition has been performed for a particular alloy such as the present alloy.

2.5 Conclusions

In this paper we describe a critical comparison of five methods to determine quantitatively the degree of transformation of β-Al_5FeSi intermetallics to α-$Al_{12}(FeMn)_3Si$ in an aluminium AA 6005A extrusion alloy. Four of these methods are based on classification of individual particles as either α-Al(FeMn)Si or β-AlFeSi and averaging the results by searching a sufficiently large surface area. For this

classification we used either the geometrical aspect ratio or the local chemical composition of the intermetallics. In addition quantitative x-ray diffraction measurements on the intermetallics as extracted from the matrix were performed. For all methods a procedure was developed on the basis of a simple error analysis which yielded a reasonably good estimate (typically 13% variation) of the relative α-fraction transformed. The best estimate of the relative fraction transformed (typically 5 % variation) was obtained by using a combination of two classification criteria (the (Mn+Fe)/Si ratio and the absolute local Mn concentration) applied to individual intermetallic particles. The method is applicable to other AA 6xxx extrusion alloys, can be fully automated and is relatively labour unintensive.

References

[1] A. Vallés, P. L. Orsetti Rossi and R. Tosta: *Homogenising of 6063 alloy*. In: Proceedings of the 6th International Conference on Aluminium Alloys, vol 4. Toyohashi, Japan: Japan Institute of Light Metals (1998) 2123-2128.

[2] K. E. Nilsen and P. T. G. Koenis: *Quantitative analysis of the homogenizing heat treatment by means of AlFeSi particle analysis and the effect on productivity*. In: J. Adams *et al.*, editor. Proceedings of 7th International Aluminum Extrusion Technology Seminar, vol 2. Chicago: Aluminum Extruders Council (2000) 69-75.

[3] D. T. L. Alexander and A. L. Greer: *Solid-state intermetallic phase transformations in 3XXX aluminium alloys.* Acta Mater. **50** (2002) 2571-2583.

[4] G. Sha, K. O'Reilly, B. Cantor, J. Worth and R. Hamerton: *Effect of grain refiner on intermetallic phase formation in directional solidification of 6xxx series wrought Al alloys.* Mat. Sci. For. **304-306** (2000) 253-258.

[5] T. Minoda, H. Hayakawa and H. Yoshida: *The quantitative analysis of α-AlFeSi ratio in a 6063 aluminum alloy billet by x-ray diffraction.* In: T. Sato, editor. Proceedings of 6th International Conference on Aluminium Alloys (ICAA-6)-Their Physical and Mechanical Properties. Toyohashi, Japan: The Japan Institute of Light Metals (1998) 339-344.

[6] S. D. Forder, J. S. Brooks, A. Reeder and P. V. Evans: *Fe-57 Mossbauer spectroscopy of intermetallic phases in DC cast aluminium.* Script. Mat. **40** (1998) 45-48.

[7] C. J. Simensen, P. Fartum and A. Andersen: *Analysis of intermetallic particles in aluminium by dissolution of the sample in butanol.* Fresenius Z. Anal. Chem. **319** (1984) 286-292.

[8] G. L. Song and L. A. Bursill: *Electron diffraction study of α-AlMnSi crystals along non-crystallographic zone axes.* Int. J. Mod. Phys. B **12** (1998) 2279-2303.

[9] V. Hansen, B. Hauback, M. Sundberg, C. Rømming and J. Gjønnes: *β-$Al_{4.5}FeSi$: A combined synchroton powder diffraction, electron diffraction, high-resolution electron microscopy and single-crystal x-ray diffraction study of a faulted structure.* Acta Cryst. **B54** (1998) 351-357.

[10] C. F. Jatczak, J. A. Larson and S. W. Shin: *Retained austenite and its measurements by x-ray diffraction.* Warrendale, PA: Society of Automotive Engineers (1980).

[11] L. F. Mondolfo: *Aluminum Alloys: Structure and Properties.* London UK: Butterworth & Co Ltd (1976).

[12] L. Lodgaard and N. Ryum: *Precipitation of chromium containing dispersoids in Al-Mg-Si alloys.* Mat. Sci. Tech. **16** (2000) 599-604.

[13] J. W. Christian: *The theory of transformations in metals and alloys.* Oxford, UK: Pergamon Press (1965).

Chapter 3

Characterisation of α-Al(FeMn)Si nuclei on β-AlFeSi intermetallics by Laser Scanning Confocal Microscopy

Laser Scanning Confocal Microscopy (LSCM) in combination with a deep etching technique to isolate the intermetallics from the matrix is used to obtain 3D images of α-Al(FeMn)Si nuclei on β-AlFeSi plate-like intermetallics in a partially homogenised 6005A Al alloy. Quantitative topological information of the α nuclei is deduced from the data. This information is crucial in building and validating future physical models for the kinetics of the transformation of β-AlFeSi plates into α-Al(FeMn)Si particles.

3.1 Introduction

As cast billets of aluminium extrusion alloys of the 6xxx Al alloys family require a homogenisation treatment to make the material suitable for hot extrusion [1]. During this homogenisation treatment several processes take place such as the transformation of interconnected plate-like monoclinic β-Al_5FeSi intermetallics into more rounded discrete cubic α-$Al_{12}(FeMn)_3Si$ particles [2-4], the dissolution of Mg_2Si [5-8] and Si precipitates [8] and the precipitation of elements still in supersaturated state [9-10]. Of these processes the phase transformation of the intermetallics and the accompanying shape change is deemed to be the most important for obtaining a good extrudability and in particular a good surface quality in the extruded product. However, little

microstructural and topological information is available concerning the details of this transformation process and in the absence of such information realistic modelling of the kinetics of this transformation on a physical basis is not possible [11]. To enable the construction of such physical models quantitative information concerning the position of the α particles on the β plates, their 3D shape during early and later stages of growth, and their site density is required.

In principle such information can be obtained by standard optical microscopy in combination with stepwise (step size < 0.2 μm) sectioning, Scanning Electron Microscopy (SEM) on deep etched samples, or Transmission Electron Microscopy (TEM).

Whilst the SEM offers the advantage of an extremely high depth of field which enables deepetched samples to be readily imaged, this technique does not allow quantitative data regarding 3D topography to be obtained.

This chapter describes the very first results of a 3D characterisation of such α-Al(FeMn)Si particles on β-AlFeSi plates in a partially homogenised 6005A Al alloy using Laser Scanning Confocal Microscopy (LSCM) in combination with a deep etching technique to isolate the intermetallics from the matrix. The advantage of LSCM over the methods mentioned earlier is that a sufficient lateral and vertical resolution (typically 190 nm lateral and 300 nm in the z direction) is obtained possible and this yields the required accuracy of topological detail. This topology can be described quantitatively in 3 dimensions using commercial software.

3.2 Experimental

The material used in this work is a commercial DC cast 6005A series Al alloy the composition of which is given in Table 3.1.

Table 3.1 Chemical composition (wt.%) for the investigated 6005A Al series.

Al	Si	Mg	Fe	Mn	Zn	Other
balanced	0.83	0.70	0.27	0.18	0.02	<0.01

The as-cast material contained interconected plate like β-AlFeSi intermetallics, with a typical length of a few tens of microns and a mean thickness of half a micron. Using conventional optical microscopy on as-cast polished samples, no signs of α-Al(FeMn)Si particles on the β-AlFeSi plates were observed. The as-cast material was homogenised at 540 ^{0}C for 8 hours followed by rapid quenching. From the analysis in Chapter 2 it is known that this annealing treatment transforms approximately half the volume of

monoclinic β-Al_5FeSi into cubic α-$Al_{12}(FeMn)_3Si$. The advantage of using a sample with such a degree of transformation is that the initial network of β–AlFeSi plates is still more or less intact and the original position of the α particles with respect to the parent phase can still be determined. The annealed samples were subsequently etched in an electrolytic solution of 78 mL percloric acid, 300 mL H_2O, 730 mL ethanol, and 100 mL butylglycol at 10 volts for one minute. This etching procedure resulted in the removal of a layer of matrix material to a depth of approximately 10 μm below the original surface. No signs of attack of the surface of the β-AlFeSi intermetallics were observed. The deep etched samples were subsequently studied using LSCM. To this aim a Leica TCS NT was used with an appropriate software package for image reconstruction. The measurements were performed using a 150× objective and monochromatic laser light with a wave length of 488 nm. For reconstruction of the 3D image a stack of images was recorded using a z-step size of 40 nm. Most of the β plates protruded perpendicularly above the surface however a number of plates were inclined to the surface in such a way as to enable detailed observation of the plate surfaces.

3.3 Results and conclusion

Thirty β–AlFeSi intermetallic plates were examined in detail to build a general picture concerning the formation of α-Al(FeMn)Si particles on these β-AlFeSi plates. Figure 3.1 shows the topographic view of a characteristic β–AlFeSi plate containing several α–Al(FeMn)Si nuclei.

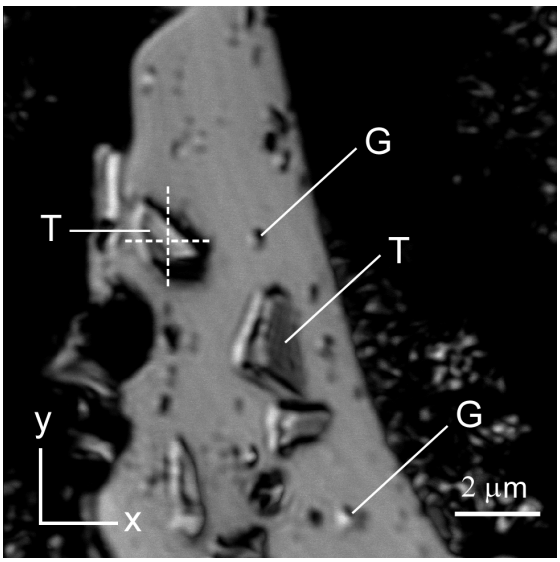

Figure 3.1. Perpendicular topographic view of a β-AlFeSi plate containing α-Al(FeMn)Si particles. The different types of α particles are indicated on some particles in the figure: T: triangular nuclei; G: globular nuclei. The dotted lines indicate the direction and the length of the profile scan show in Figure 3.2a and b.

The figure clearly reveals the presence of several α-particles on a single β-plate. Formation of α nuclei was observed both on the plate edges and on the broad faces. Nuclei were distributed more or less uniformly over the surface of the β plate. Two distinctly different particle shapes were encountered: triangular and globular. These different particle morphologies are illustrated in the figure (labelled 'T' and 'G' respectively). Figures 3.2a and b show two cross sectional profiles over a large α particle in Figure 3.1. Figure 3.2c shows a complete 3D reconstruction of this particle.

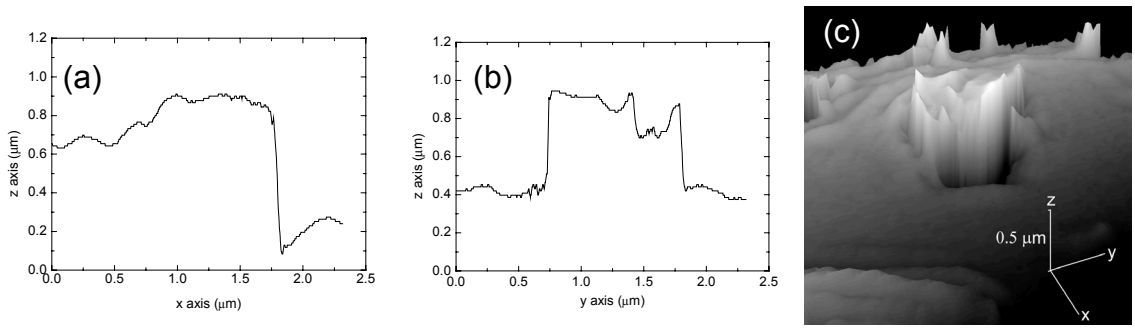

Figure 3.2 A facetted α particle which was shown in Figure 3.1 in greater detail. (a) Cross-sectional profile in x direction. (b) Cross sectional profile in y direction. (c) 3D view of reconstructed image.

The profiles show that the α-Al(FeMn)Si particle in Figure 3.2 is facetted. Taking into account the large difference in inclination angle with respect to the surface of the β-plate, it is likely that the particle has grown by an epitaxial growth mechanism however additional TEM work is required to obtain solid evidence of epitaxy. The height of the particle is approximately 0.4 μm. No signs of preferential attack of either the α-Al(FeMn)Si particle or the β-AlFeSi plate near the interface was observed. Furthermore, due to the sharpness of the transition it seems safe to assume that all aluminium matrix material at the surface of the observed α and β intermetallics has been removed in the etching process.

A second example of a β-AlFeSi plate containing α-Al(FeMn)Si particles revealing similar features is shown in Figure 3.3.

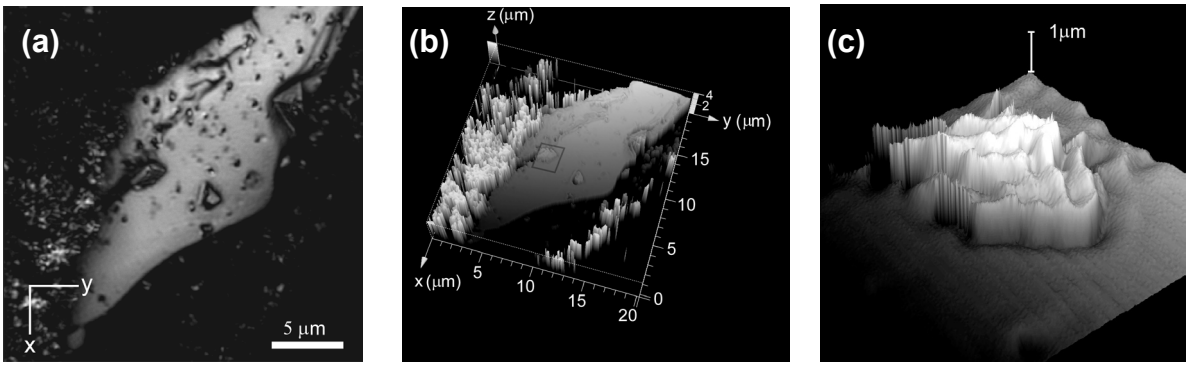

Figure 3.3 A LSCM image of a β-AlFeSi plate with α-Al(FeMn)Si nuclei on its surface. (a) Topographical image. (b) 3D image of the same spot. (c) 3D image of one α nucleus for which position is indicated in (b).

The results of all topological measurements on α particles larger than 0.1 μm have provided the general information on the characteristic dimensions of the various α particles, which is listed in Table 3.2.

Table 3.2 Characteristics of α particles observed on 30 investigated β-plates.

Particle type	Max lateral dimension (μm)	Max vertical dimension (μm)	Estimated site density (μm^{-2})	Number of α particles observed
triangular	5.4	1	0.03	88
globular	0.5	0.3	0.16	524

The quantitative topological information as provided in Table 3.2 has not been reported before but is crucial in building and validating physical models for the kinetics of the transformation of β-AlFeSi plates into α-Al(FeMn)Si particles (see Chapter 6 and 7).

References

[1] S. Zajac, L. O. Gullman, A. Johansson and B. Bengtsson: *Hot ductility of some Al-Mg-Si alloys*. Mater. Sci. For. **217-222** (1996) 1193-1198.

[2] S. Zajac, B. Hutchinson, A. Johansson, and L. O. Gullman: *Microstructure control and extrudability of Al-Mg-Si alloys microalloyed with manganese.* Mater. Sci. and Tech. **10** (1994) 323-333.

[3] H. Tanihata, T. Sugawara, K. Matsuda and S. Ikeno: *Effect of casting and homogenizing treatment conditions on the formation of Al-Fe-Si intermetallic compounds in 6063 Al-Mg-Si alloys.* J. Mater. Sci. **34** (1999) 1205-1210.

[4] S. Onurlu and A. Tekin: *Effect of heat-treatment on the insoluble intermetallic phases present in an AA-6063 alloy*. J. Mater. Sci. **29** (1994) 1652-1655.

[5] S. P. Chen, M. S. Vossenberg, F. J. Vermolen, J. van de Langkruis and S. van der Zwaag: *Dissolution of beta particles in an Al-Mg-Si alloy during DSC runs*. Mater. Sci. and Eng. A **272 (**1999) 250-256.

[6] F. J. Vermolen, C. Vuik and S. van der Zwaag: *Modelling the microstructural changes during the homogenisation of extrudable aluminium alloys.* J. Mech. Behav. Mater. **9** (1998) 115-120.

[7] F. J. Vermolen, C. Vuik and S. van der Zwaag: *A mathematical model for the dissolution kinetics of Mg_2Si phases in Al-Mg-Si alloys during homogenisation under industrial conditions.* Mater. Sci. Eng. A. **254** (1998) 13-32.

[8] F. J. Vermolen, H. M. Slabbekoorn and S. van der Zwaag: *The apparent activation energy for the dissolution of spherical Si-particles in AlSi-alloys.* Mater. Sci. Eng. A **231 (**1997) 80-89.

[9] L. Lodgaard and N. Ryum: *Precipitation of chromium containing dispersoids in Al-Mg-Si alloys*. Mater. Sci. Tech. **16 (**2000) 599-604.

[10] H. Hirasawa: *Precipitation Process of Al-Mn and Al-Cr Supersaturated Solid Solution in Presence of Age Hardening Phases*. Scripta Metall. **9** (1975) 955-958.

[11] Y. van Leeuwen, S. I. Vooijs, J. Sietsma and S. van der Zwaag: The effect of geometrical assumptions in modeling solid-state transformation kinetics. Metall. Mater. Trans. **29A (**1998) 2925-2931.

Chapter 4

2D Characterisation of morphological evolution of α and β particles during homogenisation

In this chapter, the 2D morphological evolution of both the α particles and β particles during the homogenisation process is investigated by Scanning Electron Microscopy (SEM) in combination with a delicate electro-polishing method. The types of α particles are classified at various stages of the homogenisation of a representative AA 6005A alloy. For the characterisation of α particles we use a classification scheme which distinguished several types of α particles by their position and morphology. Additionally, we investigate the evolution of the morphology of the β-intermetallics during homogenisation. Finally a generalised picture of the morphological changes of the β and α particles is deduced from the measurements.

4.1 Introduction

The previous chapters showed that during the homogenisation process of 6xxx alloys, the β constituents dissolve gradually while the α particles grow. Therefore, it is expected that the position and morphology of the α particles, relative to the β plates, must change during homogenisation. It is interesting to investigate these changes quantitatively, since this will give a better perception of the β to α kinetics.

Some publications were found that describe the change in intermetallic morphology during homogenisation of 6xxx alloys [1-4]. However, no literature was found which make a distinction between the morphological evolution of the separate α phase and separate β phase at various stages of the transformation. Probably, this is due to the difficulty to find suitable experimental techniques to distinguish the α and β particles.

In Chapter 3 we already observed α particles on the faces of the β-plates on deep-etched samples by Laser Scanning Confocal Microscopy (LSCM). In those experiments we measured interesting features of the α-particles, such as facetting, size distributions, and nucleation densities. Despite the interesting results, it was not possible to investigate different stages of the β-to-α transformation. Also, the deep-etched samples did not reveal some of the important morphological features of the α particles, such as the β/α interface and the α particles at the rim of the β plates. Therefore, by the deep-etched observations, we still miss some crucial information required for the modelling of the kinetics of the β-to-α transformation.

Another optional technique for the determination of α particles is Transmission Electron Microscopy (TEM). A TEM observation was published [5] which present a α-Al(FeCr)Si particles situated on β particles, that had similar features as presented in this thesis. TEM images of α and β particles have a high resolution, however, with TEM, it is difficult to depict a statistically reliable distribution of the type of α-particles, because only a few α particles can be observed on one TEM sample. Another disadvantage of TEM is that it is difficult to determine the position of the α particle relative to the β plate, because in most cases the β plates are too long to be observed completely.

Another optional technique to obtain a distribution of the type of α particles is by optical microscopy. By etching with HF it is possible to distinguish between α and β particles by their differences in grey scale [3]. Optical measurements should give a reliable statistical distribution of the type of α particles, since multiple α particles can be detected by their difference in grey scale. But, in our preparatory experiments we found that in most cases the resolution of this method is too low to distinguish all α particles from β particles.

Because of the disadvantages of deep-etching, TEM and optical microscopy, in this chapter Scanning Electron Microscopy (SEM) in combination with a delicate electro-polishing method was used to classify several types of α particles at different stages of the homogenisation. By the SEM analysis we still have a high resolution, enough to distinguish between α and β phases by the etching and morphology. This feasibility was verified by Electron Diffractive X-ray (EDX) measurements. By the SEM analysis we were able to get statistically reliable results, e.g. we were able to classify hundreds of α particles during our experiments. For the characterisation of α particles we used a classification scheme which distinguished several types of α particles by their position and morphology. Additionally, we investigated the evolution of the morphology of the β-intermetallics during homogenisation. In this chapter, such studies were performed on a representative AA 6005A alloy.

4.2 Experimental

4.2.1 Materials and homogenisation treatments

A representative Al-Mg-Si alloy (AA 6005 A) with an alloy composition of 0.70 wt.% Mg, 0.83 wt.% Si, 0.27 wt.% Fe, and 0.18 wt.% Mn was used for our investigations. The investigated alloy was DC-cast with a diameter of 254 mm.

Samples were taken from the billet at locations between 10 mm and 30 mm from the rim of the billet. The microstructure of these samples represents the typical microstructure of the billet. An air circulation oven, in which the maximum temperature deviation over all locations was 3°C, was used to homogenise the samples. Series of samples were homogenised at a temperature of 540°C for various times ranging between 30 minutes and 32 hours. By this, we obtained a set of samples with various transformed relative α fractions. This relative α fraction is defined such that in the case of f_α=0, only β intermetallics are present, and in the case of f_α=1 the β intermetallics are completely transformed.

The relative α-fraction of each sample was determined experimentally by using automatic SEM measurements in combination with Electron Dispersive X-ray Spectography (EDX) on a personal SEM at BOAL B.V. Figure 4.1 shows the relative α fraction as function of homogenisation time of the samples, as described in Chapter 2.

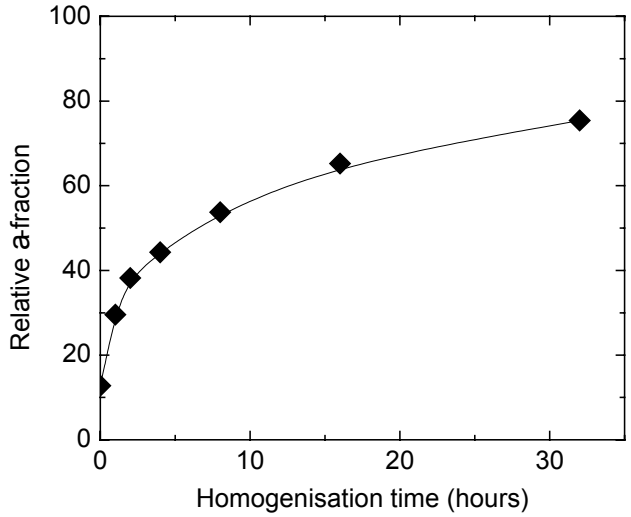

Figure 4.1 The relative α fraction as a function of homogenisation time.

4.2.2 Characterisation of intermetallics

A JEOL 6500F SEM at the TU-Delft was used to determine the morphology and spacial distribution of the α and β particles of a sample. For those examinations, we used samples which were polished with ¼ μm silica and subsequently electro-etched at 20 V

during 20 seconds in a mixture of 78 mL perchloric acid, 90 mL water, 730 mL ethanol and 100 mL butylglycol (commercial Struers reagent II). This electro-polish method will give a smooth surface, will avoid smearing of the intermetallic polished plane into the matrix, and will slightly etch the surfaces of the β and α particles, making it possible to distinguish between α and β particles. For the morphology measurements a voltage of 2 kV and a working distance of 15 mm was used. The compositions of some α and β particles were determined by Electro Dispersive X-ray (EDX). For those measurements a voltage of 15 kV and a working distance of 25 mm was used.

For the classification of various types of α particles in the samples we used the scheme of Table 4.1. For each sample a large number of α particles were classified in various types, labelled A, B, C, and D. α-Particles of type A were located on top of a face of the β plate. α-Particles of type B were located close to the rim of the β plate. α-Particles of type C were located at the rim of the β plate, or grew around the rim of the β plate. Particles of type D were located separately in the Al-matrix. Those particles may be located close to the β particle, close to other α particles, or separately in the matrix.

Table 4.1 Scheme of the type of α-particles used for the classification.

Type	Schematic drawing of the position of the α particle:	Brief description:
(A)	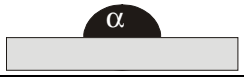	**on the β surface:** α particle on the flat surface (face) of the β particle.
(B)		**touch the rim of β plate:** the α particle touch the rim of the β plate
(C)	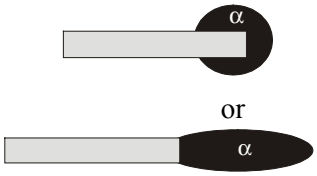	**on the rim:** the α-particle grows around or on the rim of the β-particle.
(D)	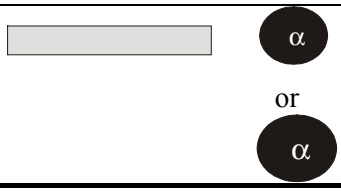	**Separate:** α particle separate in the Al-matrix.

The average thickness of the β-plates in the samples was determined with the JEOL on electro-polished samples. For each sample, 50 individual β plates were determined. The thickness was measured perpendicular to the length of the β-plates.

Also the average length of the β-plates in the samples were determined. Since the length of the β plate (~10 μm) is in another scale than the thickness (~0.2 μm) of a β plate, we used the automatic SEM (see Chapter 2) which has a lower resolution than the JEOL, but is less laborious.

4.3 Results

4.3.1 Qualitative characterisation of α and β particles

Figure 4.2a shows an example of two facetted α particles on top of a face of a β particle. Some small pitting (~10 nm) occurs on both the α and the β particles however this does not affect the quality of the observations. The pitting is even an advantage since the pitting on the α phase is slightly heavier than that on the β particle, which facilitates the discrimination between the two phases.

Table 4.2 shows the results of the EDX measurements on the indicated spots in Figure 4.2a (α1, β1 and β2). Since we do not know which part of the Al-matrix is measured in an EDX measurements (see Chapter 2), it is only justified to compare the composition ratios of the other elements. For the analysis we use the S-ratio (defined as the Si content divided by the Fe and Mn content) and the Mn-ratio (defined as the Mn content divided by the Fe and Mn content). Of the α phase both, the S-ratio and Mn-ratio, were higher than those of the β phase. This reflects the expected properties of the α phase. We therefore conclude that we found a feasibility to classify α and β particles by the observed differences in etching and morphology.

Also some EDX measurements were performed on five different β plates and 5 separate α particles. The average figures of those measurements also confirm a pronounced difference of the S-ratio and of the Mn-ratio between the α and the β particles. Some annotations can be made on the average EDX figures. The S-ratio of the β phase was approximately unity, which was expected from the stoichiometry of the β particle. However the S-ratio for the α particle (~2) was somewhat lower than expected (~3). This slight deviation is probably caused by the influence of neighbouring β plates close to the α particles. Also a low Mn concentration was found in the β particles, which was not expected since no Mn is present in the β particles. Probably this minor artefact was caused by the presence of the α particles just below the polished plane.

Table 4.2 EDX results with α-Al_5FeSi and β-$Al_{12}(FeMn)Si$ particles.

location	c_{Al} (at.%)	c_{Fe}(at.%)	c_{Mn}(at.%)	c_{Si} (at.%)	S-ratio	Mn-ratio
α1	Balanced	4.2	2.3	4.2	1.5	0.4
β1	Balanced	4.7	0.6	5.8	0.9	0.1
β2	Balanced	5.8	0.4	6.5	1.0	0.1
average α*	Balanced	4.3	2.0	3.6	1.8	0.3
average β*	Balanced	4.2	0.3	4.9	0.9	0.1

* average of 5 different spots

Figure 4.2 gives examples of various morphologies of α particles for a sample homogenised for 8 hours (f_α = 0.5). For this homogenisation time we saw all types of the α particles described in table 4.1, with both facetted and non-facetted morphology. In Figure 4.2a, we see that the α particles grows on a face of the β particle and that the β/α interface stays unaffected. For all observed α particles that lay on a face of the β plate, we saw similar characteristics. Also, Figure 4.2a shows that the rims of the β plate is rounded, which is a characteristic of the β plate seen with most plates during homogenisation. Figure 4.2b presents two α particles touching the rim of the β particles, which were classified as type B. We classified this type of α particle only when the distance to the β particle was less than 50 nm. However, in most cases, the α particle apparently touches the β particle, i.e. the distance was within the resolution of the SEM visualisation. Figure 4.2c shows an α particle that has grown around the β particle. This α particle was classified as type C. Also α particles were observed that completely encapsulated the β particles. Figure 4.2d shows an apparently isolated α particle. Due to the limitations of 2D it is yet hard to say whether those α particles are connected to the β particles or not. During the homogenisation more and more particles become of type D. After 32 hours of homogenisation, most of the particles were of type D and the number of β plates was drastically reduced.

It is interesting to investigate the nature of growth of α particles and the dissolution of β particles (particles of type A) in more details. Figure 4.3 illustrates three types of hypothetical morphological growths of the α particle on a face of a β particle. Figure 4.3a shows the hypothetical situation of the dissolution of the β plate near an α particle. This morphology is expected when the β plate dissolves at all β/Al interfaces (the rims and the faces). At the positions close to the α particle, the concentration gradients are higher and therefore dissolution is expected close to the α particle. In none of our micrographs we did see such a behaviour of dissolution. Figure 4.3b shows the hypothetical situation that the α particle grows into the β particle. In this case there is

diffusion from the β particle towards the α particle at the β/α interface. This implies that there is diffusion inside the β and the α particles. In none of our micrographs we did see such a behaviour in growth via the interface. Figure 4.3c shows the situation of a straight interface between the α and the β particle. In this case the α particle stays on top of the β plate and the main faces of the β plates are not affected. The α particle grows towards the edges of the β particle and the β particle dissolves only at the rim of the β plates.

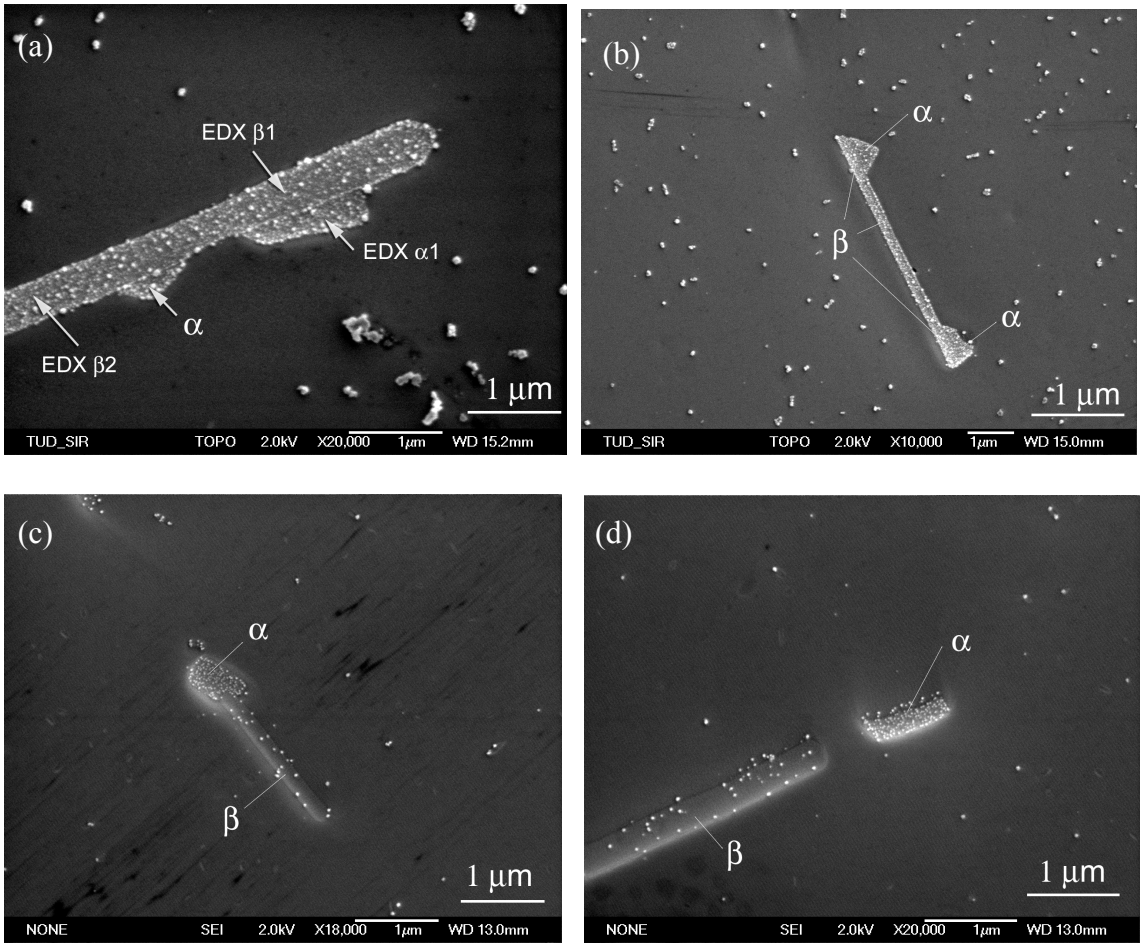

Figure 4.2 Observations of various types of α particles (a) Type A: α nuclei on top of β. The spots of the EDX measurements are indicated and labelled by α1, β1 and β2. (b) Type B: two α particles on the edges of the β particle. (c) Type C: an α particle growing over the rim of the β particle. (d) Type D: separate α particle close to a β particle. All pictures were taken of a sample homogenised for 8 hours at 540°C. Some pits in the aluminium matrix are small artefacts, induced by the electro-polish method.

With almost all experimental observations with α particles on the face of the β particles (Type A particles, e.g. Figure 4.2a) we observed the situation as presented in Figure 4.3c. This implies that there is no dissolution from the main face of the β-plates,

both on the β/Al and β/α interface. Since the β/α interface is not affected, there is no direct mass-transport diffusion in the intermetallics from the β plates towards the α particle. The only mechanism left for the growth of the α particles is by transport of elements from the rims of the β plates through the Al-matrix towards the α particle. Note that, next to Fe and Si diffusion, there is also Mn diffusion from the Al-matrix towards the α particles. This aspect also promotes the α particle to grow like Figure 4.3c.

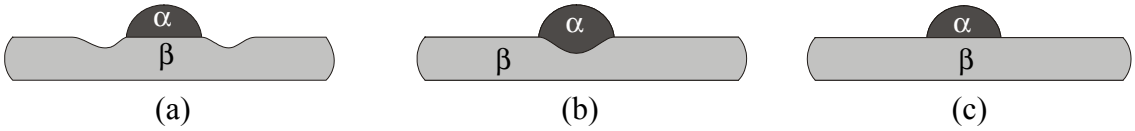

Figure 4.3 Three hypothetical morphological growths of the α on the β particles. (a) β plate dissolves close to the α particles (b) α particles "digs" in the β particle. (c) α particle stays on top of the β plates and the faces of the β plates are unaffected.

4.3.2 quantitative characterisation of the evolution of α and β particles

Figure 4.4 depicts the quantitative evolution of the morphology of the β-AlFeSi particles during homogenisation at 540°C. In this figure the evolution of the length and the width of the β plate are plotted, which were measured as described in Section 4.2.2. The figure shows a rapid decrease of the length of the β plates in the first 10 hours of the homogenisation (f_α=0-0.5). This indicates that the β plates breaks up into smaller plates at the beginning of the homogenisation. In contrast, the width of the β plates does not change significantly during time, and remains ~0.4 μm. It was not possible to get quantitative thicknesses at later homogenisation times than 10 hours, since most of the β plates were dissolved at these times. The observation corresponds with the conclusion in Section 4.3.1, where it was also found that the β face was not affected during homogenisation and the β plates only dissolve at the rims of the β particles.

The evolution of the α particles during homogenisation is also investigated for samples that were homogenised lightly, (for 2 hours, f_α=0.20), intermediately (for 8 hours, f_α=0.50) and heavily (for 32 hours, f_α=0.70). During the homogenisation the average α particle cross sectional area increases from ~0.25 μm^2 towards approximately ~1 μm^2 indicating a growth of α particles. For the lightly homogenised sample we rarely saw α particles which were separate from the β plate (type D of table 4.1). For longer homogenisation times, these separate particles increases in number very rapidly. Most of the α particles in the heavily homogenised samples were separate in the matrix.

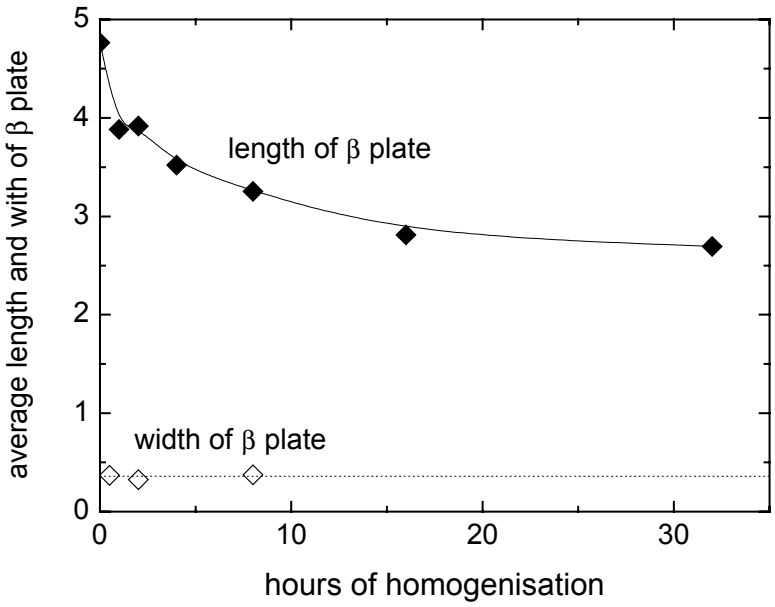

Figure 4.4 Evolution of the average length and thickness of the β particles during the homogenisation process at 540°C.

It is interesting to investigate the evolution of the α-particles which are still connected to the β-particle. This will give a picture of the evolution of the growth of the α particle during time. On the three samples we counted 80 α-particles each which were connected to the β particle, and classified them of type A, B or C, as indicated in Table 4.1. Figure 4.5 presents the evolution of the number fraction of particles of type A, B and C at various homogenisation times. E.g. the number fraction of type A is given by $n_A/80$ where n_A is the number of α particles count of type A. The figure can be briefly interpreted as follows: In the lightly homogenised samples, (f_α=~0.2), the α particles have started to nucleate and are present mainly on the faces of the β plates. Therefore we see a lot of particles of type A. In the intermediate stage, (f_α=~0.5), more α particles are situated close at the rim. This indicates that the β plates have dissolved at their edges, and the α particles have grown. At the final stage (f_α=~0.8) most of the α particles have grown around the β plate. Please note that at this stage most of the α particles are individual particles fully surrounded by the matrix (type D). The data presented in figure 4.5 only pertain to particles yet connected to relatively rare β plates.

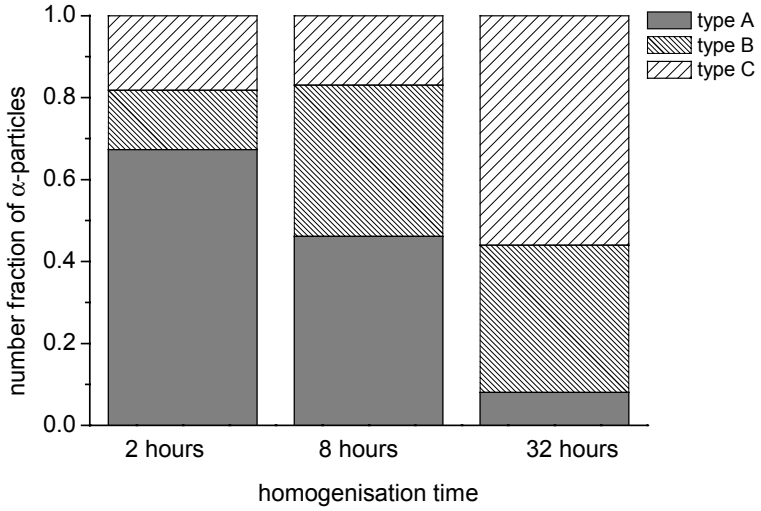

Figure 4.5 Evolution of the type of α particles during homogenisation at 540°C.

4.4 Discussion

The previous results showed that during homogenisation the β particles are dissolving and nuclei of α particles are growing on the β particles. It was found that the β particles dissolves only at their rims, and the α particle grows on all α/Al interface. A gradual evolution of type of α particle was found.

From the obtained results a generalised picture of growth morphology can be deduced, which is visualised by schematic cross sections in Figure 4.6. For the sake of simplicity, in this figure only one α particle is situated on a β particle. The various stages of the growth, indicated by the roman numbers in Figure 4.6, will be expounded as follows. (*i*) f_α=~0.2: In the early stage α particles nucleate on the face of the α particle. (*ii*) f_α=~0.3: The α particle starts to grow towards the most close rim of the β particle and the β particle starts to dissolve at its rims. (*iii*) f_α=~0.5: The α particle grows until the rim. (*iv*) f_α=~0.7: The α particle starts to grow over the β rim. (*v*) f_α=~0.8: The α particle also grows towards the other side of the β plate. (*vi*) f_α=~0.9: No observations were made which give clear insight into the very last stages of β plate dissolution. Full encapsulation of β plates by α has not been observed. (*vii*) f_α=~1.0: The β particle is completely transformed to an α particle. The final α particle is thicker and more rounded than the initial β particle.

The morphological development as observed formed the basis of the diffusion controlled β-to-α transformation model presented in Chapters 6 and 7.

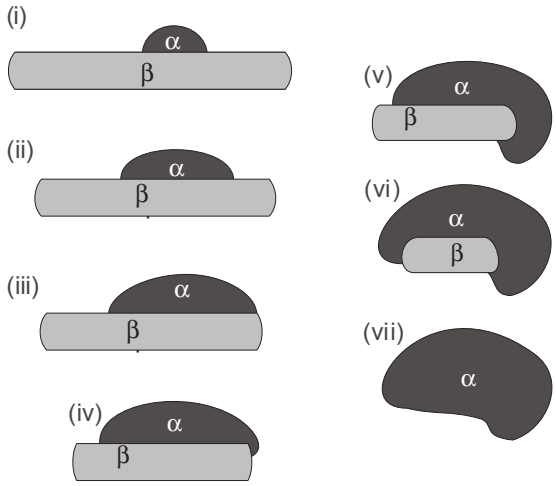

Figure 4.6 Schematic pictures of the growing of the α particle on the β particle. The order of the steps of evolution are indicated by the roman numbers.

4.5 Summary

The morphological evolution of both the α particles and β particles during the homogenisation process were investigated by SEM. It was obtained that the β particles dissolves only at the rims, and their faces are not affected during homogenisation. Already in the beginning of the transformation these β plates breaks up into smaller plates. For the morphology evolution of the α particles we saw some interesting new features. In the early stages of the homogenisation (f_α=0.2) α particles start to nucleate on the main surfaces of the β plate. In later stages (f_α=0.5) those nucleated α particles grow closer to the rims of the β particles. At later stage (f_α=0.8) the α particles will grow over the rims of the β particle and encapsulate the β particles. During homogenisation there is a mass transport of Fe and Si from the rim of the β particles towards the α particles, leaving the β plates to dissolve and the α particles to grow. The rounded shape of the rims of the β particle and α particles gives indications of a diffusion controlled transformation. The obtained information about the growth kinetics will be used as a basis for the Finite-Element Model in Chapter 6 and 7.

References

[1] S. Onurlu and A. Tekin: *Effect of heat-treatment on the insoluble intermetallic phases present in an AA 6063 alloy.* J. Mater. Sci. **29** (1999) 1652-1655.

[2] M. H. Mulazimoglu, A. Zaluska, J. E. Gruzleski and F. Paray: *Electron microscope study of Al-Fe-Si intermetallics in 6201 aluminum alloy.* Metall. Mater. Trans. A **27** (1996) 929-936.

[3] S. Zajac, L. O. Gullman, A. Johansson and B. Bengtsson: *Microstructure control and extrudability of Al-Mg-Si alloys microalloyed with manganese.* Mat. Sci. Forum **217-222** (1996) 1193-1198.

[4] H. Tanihata, T. Sugawara, K. Matsuda and S. J. Ikeno: *Effect of casting and homogenizing treatment conditions on the formation of Al-Fe-Si intermetallic compounds in 6063 Al-Mg-Si alloys.* J. Mat. Sci. **34** (1999) 1205-1210.

[5] L. Lodgaard and N. Ryum: *Precipitation of dispersoids containing Mn and/or Cr in Al-Mg-Si alloys*. Mater. Sci. Eng. A **283** (1999) 144-152.

Chapter 5

The evolution of the 3D intermetallic structure during a homogenisation treatment

During homogenisation of AA 6xxx alloys a phase transformation occurs and the intermetallic structure evolves from an interconnected network of plate-like structures into a more discrete distribution of particles. The morphology of these intermetallics has been the subject of many studies employing conventional 2D characterisation. However, recently it has been shown that 2D analyses can be misleading and that techniques suitable for quantification of 3D structures can provide more reliable information.

In this chapter serial sectioning and 3D reconstruction techniques were used to reveal the three-dimensional morphology, connectivity and distribution of the intermetallic microstructure, and the evolution of these parameters during homogenisation. The qualitative and quantitative analysis of the reconstructed intermetallic microstructures is discussed, with particular reference to the determination of the spatial distribution of the absolute, mean and Gaussian curvature.

5.1 Introduction

For commercial aluminium extrusion alloys a homogenisation heat treatment of the as-cast material is required to improve ductility and enable efficient extrusion [1]. The optimisation of such extrusion processes will depend on a thorough understanding of the reactions occurring during homogenisation and, in particular, the morphological evolution of the intermetallics during the homogenisation process.

The principle processes which occur during this homogenisation are a phase transformation from monoclinic β-Al_5FeSi to cubic α_c-$Al_{12}(FeMn)_3Si$, and a gradual morphological change from interconnected plate structures to more discrete, globular structures [2-4]. The morphology of these intermetallics has been the subject of many studies employing conventional 2D characterisation. Such two dimensional metallographic techniques are usually used to provide information regarding morphology, connectivity or distribution of the intermetallic microstructure. However, it has recently been shown that 2D analyses [5-6] can be misleading and that techniques for a proper quantification of 3D structures need to be employed. The focus of this chapter is on obtaining detailed 3D information regarding the evolution of the microstructural morphology during homogenisation heat treatment.

5.2 Experimental Techniques

5.2.1 Alloy composition and heat treatment

The alloy under investigation is an industrial DC-cast 6005A aluminium alloy. The chemical composition for this alloy is shown in Table 5.1. Material was received in the form of an as cast billet with a diameter of 254 mm. To ensure the same starting as-cast microstructure for each sample, all metallographic samples were sectioned from locations approximately 25 mm from the edge of the billet.

Table 5.1 The chemical composition (wt.%) of the 6005A Al alloy under investigation.

Al	Si	Mg	Fe	Mn	Zn	Other
Balance	0.83	0.70	0.27	0.18	0.02	≤0.01

Table 5.2 Conditions and fraction transformed from β-Al_5FeSi to α_c-$Al_{12}(FeMn)_3Si$ for the investigated samples.

Homogenisation time	cast	30min	8 h	1 h	32 h	32 h
Temperature of homogenisation (°C)	None	540	540	590	540	590
Relative fraction transformed from β-Al_5FeSi to α_c-$Al_{12}(FeMn)_3Si$ (%)	5	20	50	80	80	100

For the 3D reconstructions presented in this report, six conditions at different stages of homogenisation were produced, using two different homogenisation temperatures. Table 5.2 shows the homogenisation conditions and fraction transformed from β-

Al_5FeSi to α_c-$Al_{12}(FeMn)_3Si$ as determined using Scanning Electron Microscopy and Electron Dispersive X-ray analysis for the samples under investigation (see Chapter 2).

5.2.2 Sample preparation, serial sectioning and 3D image reconstruction

A sample of each condition under investigation was metallographically prepared in the usual manner to a ¼ μm colloidal silica polished finish. Each sample was then etched in 0.5% HF solution for 4 seconds in order to enhance the contrast between the intermetallics and the aluminum matrix.

For the 3D reconstruction a rectangular region of interest was chosen on each metallographic section and labelled using Vickers microhardness indentations. The size of the region of interest was 200 μm × 200 μm in the x- and y-directions. Micrographs of the regions of interest were then taken using a Leica TCS SP laser scanning confocal microscope (LSCM) equipped with a digital image capture facility. The confocal microscope was preferred for this application over conventional instruments since, in addition to affording a significant extension of resolution, imaging at a discrete wavelength was found to provide sharp contrast without the need for heavy etching in HF [7]. Samples were then lightly re-polished using ¼ μm colloidal silica in order to remove a thin surface layer. The microhardness indentations were then used to relocate the area of interest and photomicrographs of the region were again taken. This process was repeated approximately 40 times to create a vertical stack of serial 2D sections at regular intervals along the z-axis. The LSCM software enabled a topographical analysis of each of the sections in order to check parallelism and to correct for tilt between sections. This also enabled the depth of material removed between sections to be established, since the remaining depth of the hardness indents could be accurately measured. The total depth sectioned in this manner was approximately 40 μm in the z-direction for each sample. The serial sections were then used for 3D reconstruction of the intermetallics. The 3D reconstruction of the intermetallics was created using a medical tomography software package (surfdriver©) which processed the 2D serial sections.

5.2.3 Numerical method for the local, Gaussian and mean curvature

The surface curvature is an important factor in the transformation, since it provides an indication of local variations in surface energy. The local curvature at one point corresponds to the reciprocal of the radius of a sphere which best conforms to the surface at this point.

A 3D surface has two principal curvatures. They are defined as the minimum and the maximum of the curvatures of the intersection between a plane containing the normal

and the surface, and are called k_1 and k_2 respectively. The principal curvatures are equal to the eigenvalues of the determinant of the differential of the normal to the surface. The absolute curvature (A) is defined by the maximal absolute principal curvature. The Gaussian curvature is the product of the two principal curvatures:

$$\mathrm{K} = k_1 k_2 \tag{5.1}$$

The mean curvature, as the name suggests, is the mean value of the curvature over all possible directions:

$$\mathrm{H} = \frac{1}{2}\left(k_1 + k_2\right) \tag{5.2}$$

The Gaussian (K) and mean curvature (H) are coupled according to the following equations [8]:

$$\begin{aligned} \frac{\partial H}{\partial t} &= -(2H^2 - K)v - \frac{1}{2}\left(\frac{\partial^2 v}{\partial_2 x_1} + \frac{\partial^2 v}{\partial_2 x_2}\right) \\ \frac{\partial K}{\partial t} &= -2HKv - H\left(\frac{\partial^2 v}{\partial_2 x_1} + \frac{\partial^2 v}{\partial_2 x_2}\right) + \sqrt{H^2 - K}\left(\frac{\partial^2 v}{\partial_2 x_1} - \frac{\partial^2 v}{\partial_2 x_2}\right) \end{aligned} \tag{5.3}$$

where t is the time, v the velocity of the surface along the surface normal and x_1, x_2 represent the two principal directions along the surface. The coupling of the mean and Gaussian curvatures implies that the signs of both Gaussian and mean curvatures describe the morphology of the intermetallic microstructure. Together, the Gaussian and mean curvatures provide an essential measure of the morphology since they enable saddle-shaped, convex and concave surfaces to be distinguished.

The signs of the Gaussian and mean curvature enable a qualitative classification of morphological character. Table 5.3 shows that the morphologies fall into 6 basic classes: saddle morphologies, trough, flat ,concave cylindrical, pit and spheroid [9]. When the Gaussian curvature for a given discrete location (point) on the surface under analysis is negative, the form of the surface is approximately hyperbolic, and the local surface is saddle-like (i.e. the point is bounded by regions exhibiting both convex and concave curvatures). When the Gaussian curvature is zero, the surface surrounding the point is only cylindrical if the mean curvature is non-zero. If, on the other hand, the mean curvature is zero then the surrounding surface is planar.

Table 5.3 Surface interpretation of Gaussian curvature (K) and the mean curvature (H). The intermetallic surface is in all cases the upper surface depicted in the diagrams.

	K<0	K=0	K>0
H<0	**Concave saddle** In one orthogonal axis the slope increases rapidly (concave) whilst in the other the slope slightly falls away. 	**Trough** Negative shape of cylinder: In one orthogonal direction there is an increase of slope (concave) whilst in the other there is no slope. 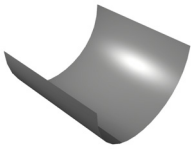	**pit** Negative of spheroid shape. Form is concave. The slope increases in all directions 
H=0	**symmetric saddle** 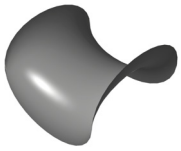	**flat surface** 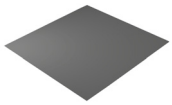	-
H>0	**convex saddle** In one orthogonal axis the slope falls away rapidly (convex) whilst in the other direction the slope slightly increases. 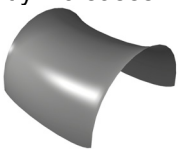	**convex cylindrical** Cylindrical shape. In one orthogonal direction the slope falls away (convex) and in the other orthogonal direction there is no slope. 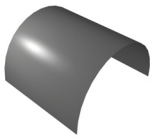	**spheroid** Form is convex. The slope falls away in all directions. 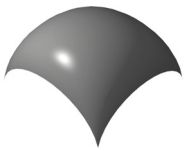

5.3 Results

5.3.1 3D qualitative observations

3D reconstructions of the intermetallic microstructure were produced from the 2D cross sections. Example of 2D images taken from a stack used for such a 3D reconstruction are shown in Figure 5.1. Two of the microhardness indents used to adjust alignment and to measure the thickness of materials removed are visible in these figures.

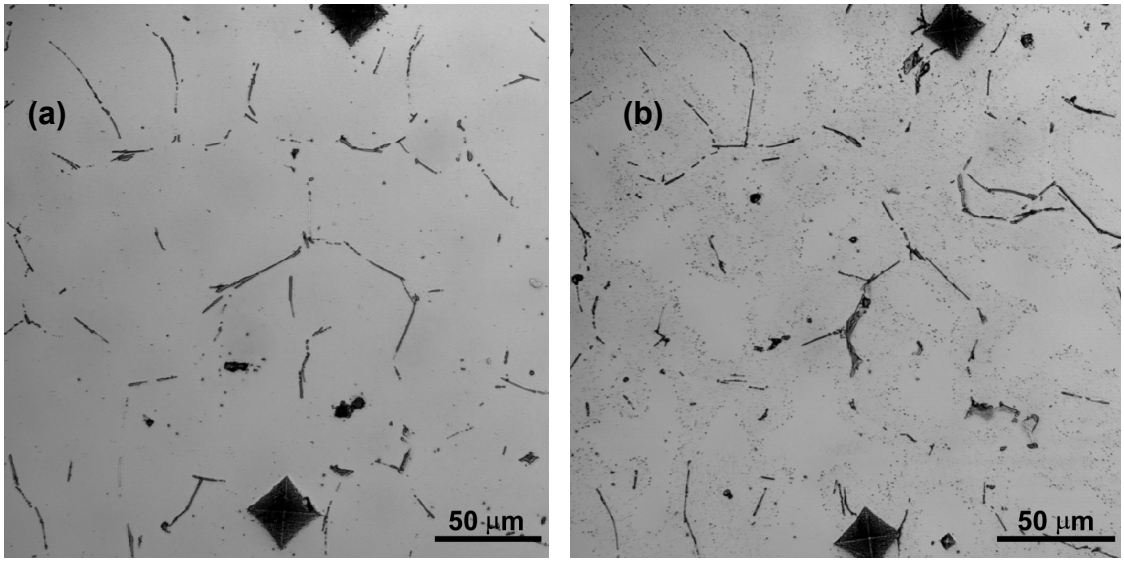

Figure 5.1 Two examples of 2D serial sections used for 3D reconstruction. (a) z=1 μm, (b) z=30 μm. The photomicrographs show the microstructure after 30 minutes homogenisation at 540°C. Note the Vickers microhardness indentations used for alignment of the micrographs are also visible.

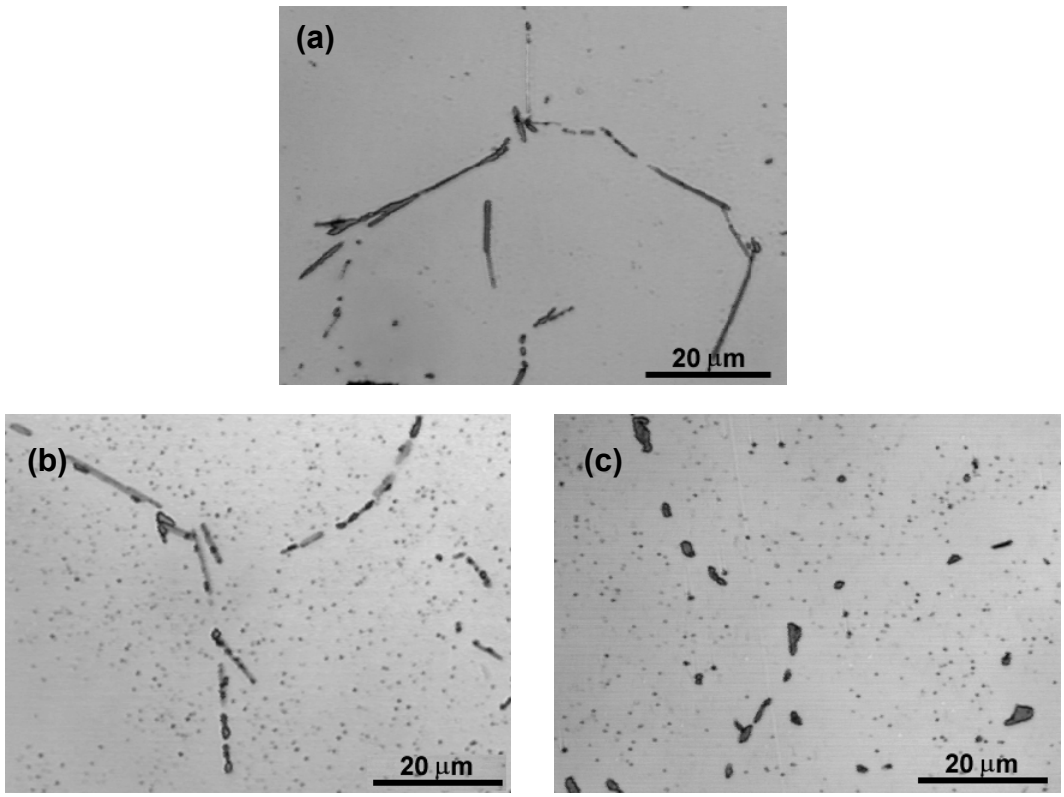

Figure 5.2 Photomicrographs showing the intermetallic structure (a) lightly homogenised for 30 minutes, (b) partially homogenised for 8 hours and (c) heavily homogenised for 32 hours at 540°C.

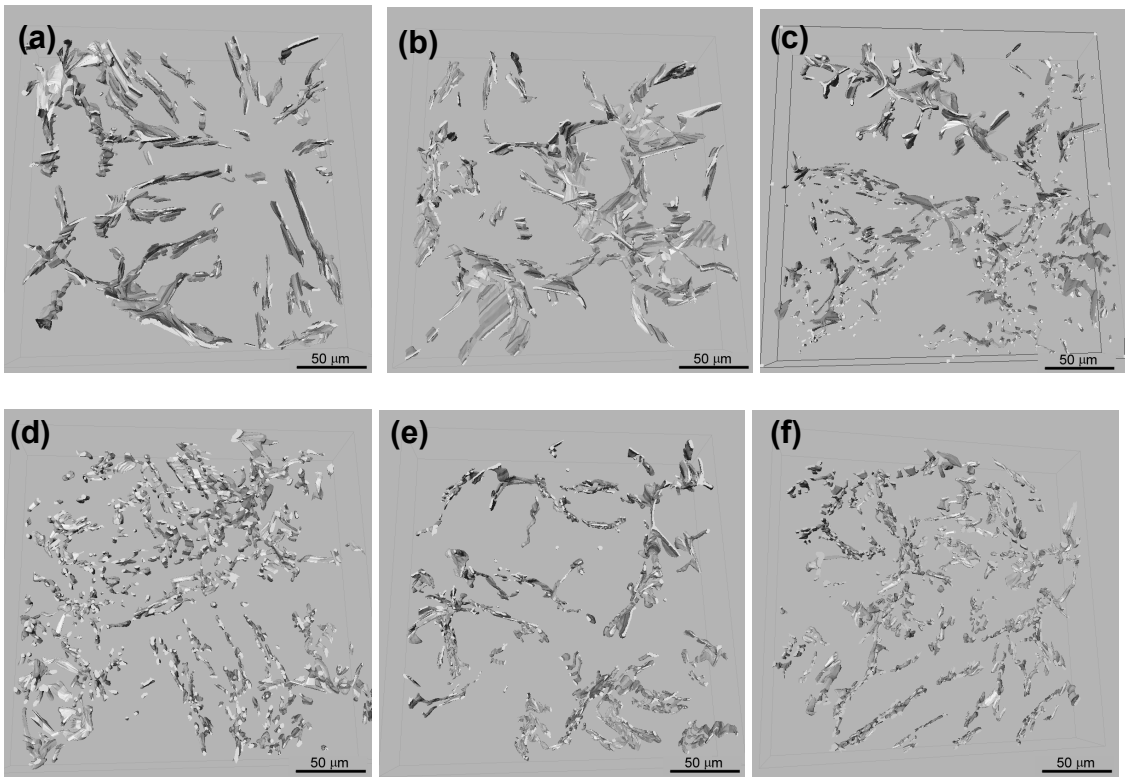

Figure 5.3 Surface-rendered 3D reconstructions of aluminium alloy intermetallic microstructure after heat treatment. (a) as-cast, (b) 30 minutes homogenised at 540°C, (c) 8 hours homogenised at 540°C, (d) 32 hours homogenised at 540°C, (e) 1 hour homogenised at 590°C , (f) 32 hours homogenised at 590°C. The indicated boxes have a dimension of 200×200×40 μm for all pictures.

Figure 5.2 shows an overview of the conventional 2D micrographs produced for the three extreme states: lightly homogenised, partially homogenised and heavily homogenised. For the partially transformed sample the etching produced contrast between the β-Al_5FeSi phase, which appears light grey, and the α_c-$Al_{12}(FeMn)_3Si$ phase, which appears dark grey.

Figure 5.3 shows the 3D reconstructions of the intermetallic for the 6 conditions studied. These images reveal that the coarse planar interconnected β-Al_5FeSi intermetallics break up into more discrete α_c-$Al_{12}(FeMn)_3Si$ particles. The 3D image in Figure 5.4 shows that the morphology of the intermetallics in the heavily homogenised structure is more cylindrical than spherical. Furthermore, the 3D analysis provides detailed information regarding the spatial distribution of the intermetallics. The interconnectivity of the intermetallics is high when the β-Al_5FeSi phase is the dominant

phase, and this connectivity decreases as the transformation from β-Al_5FeSi to α_c-$Al_{12}(FeMn)_3Si$ proceeds. However, the particle distribution remains spatially inhomogeneous even at long homogenisation times, with α particles remaining distributed in stringers along the length of the prior β network.

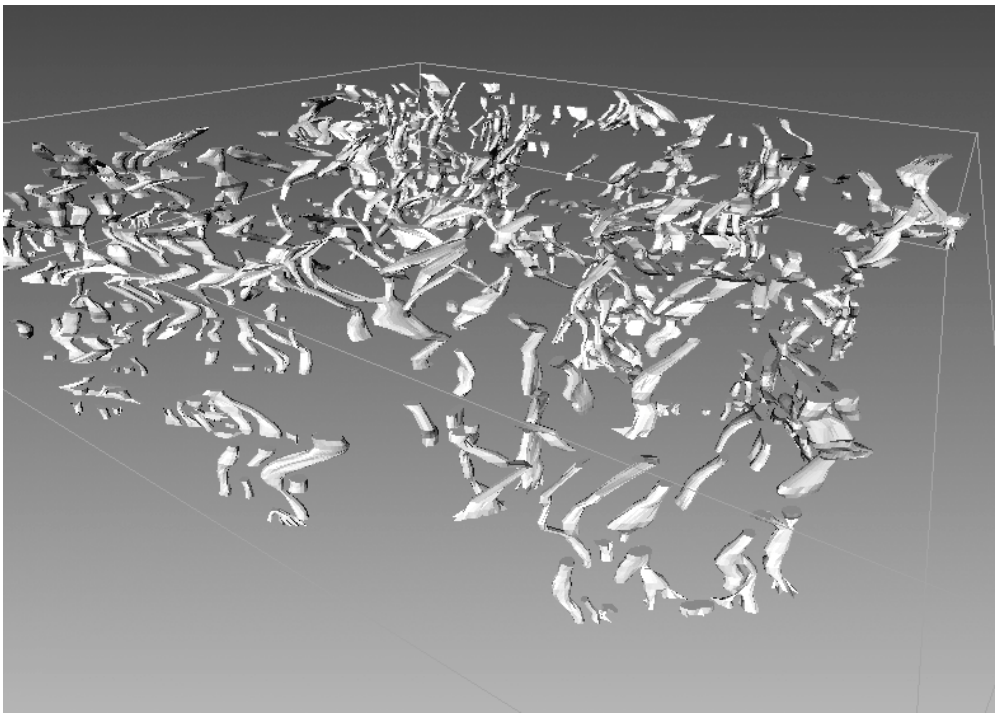

Figure 5.4 Cylindrical shaped α-particles in the surface-rendered 3D reconstruction of aluminium alloy intermetallic microstructure after heat treatment of 32 hours homogenised at 590°C. The indicated box has a dimension of 200×200×40 μm.

Table 5.4 Quantitative values as calculated from the 3D reconstruction.

Homogenisation time (hours)	0	0.5	8 (α phase)	8 (β phase)	1	32	32
Temperature of homogenisation (°C)	none	540	540	540	590	540	590
Fraction transformed from β-Al_5FeSi to α_c-$Al_{12}(FeMn)_3Si$ (%)	5	20	50	50	80	80	100
Volume/Surface (μm)	0.23	0.20	0.04	0.11	0.21	0.25	0.22

5.3.2 Area to volume ratio analysis

Table 5.4 shows the volume-to-surface ratio obtained from the 3D reconstructions by image analysis. The very small intermetallic particles, which are close to the limit of the resolution of the technique (<0.5 μm) are not measured in the 3D reconstruction, therefore the intermetallic volume fraction measured from the 3D reconstructions is lower than the total volume fraction measured from 2D micrographs. From the 3D observations it can be deduced that the morphology for the as-cast sample and the sample homogenised for 30 minutes at 540°C is plate-like. The volume-to-surface ratio can be calculated from the following equation:

$$\frac{V}{S} = \frac{l\omega\delta}{2(\omega l + l\delta + \omega\delta)}, \tag{5.4}$$

with l the length of the plate, ω the width and δ the thickness. If we assume that the thickness is negligible compared to the length and width, we obtain:

$$\frac{V}{S} = \frac{\delta}{2} \tag{5.5}$$

From this equation and the volume to surface ratio an average thickness of the plate can be calculated. For the as-cast and 30 minutes homogenised at 540°C conditions this yields thicknesses equal to 0.46 μm and 0.40 μm respectively.

Based on the 3D observations the intermetallics observed in samples homogenised for 32 hours at 540°C, 1 hour and 32 hours at 590°C appear to have a cylindrical morphology. The volume-to-surface ratio can be calculated from:

$$\frac{V}{S} = \frac{\pi R^2 l}{2\pi R l} = \frac{R}{2}, \tag{5.6}$$

where l is the length of the cylinder and R the radius. Using this equation and the volume to surface ratio measured, the average radius of the cylinder was calculated to be 0.50 μm, 0.44 μm and 0.42 μm for the three samples respectively.

The 2D analysis on the same samples gives radii of 0.70 μm, 0.67 μm and 0.74 μm. The 2D measurements leads to tilted sectioning which may be expected to yield a larger value of R.

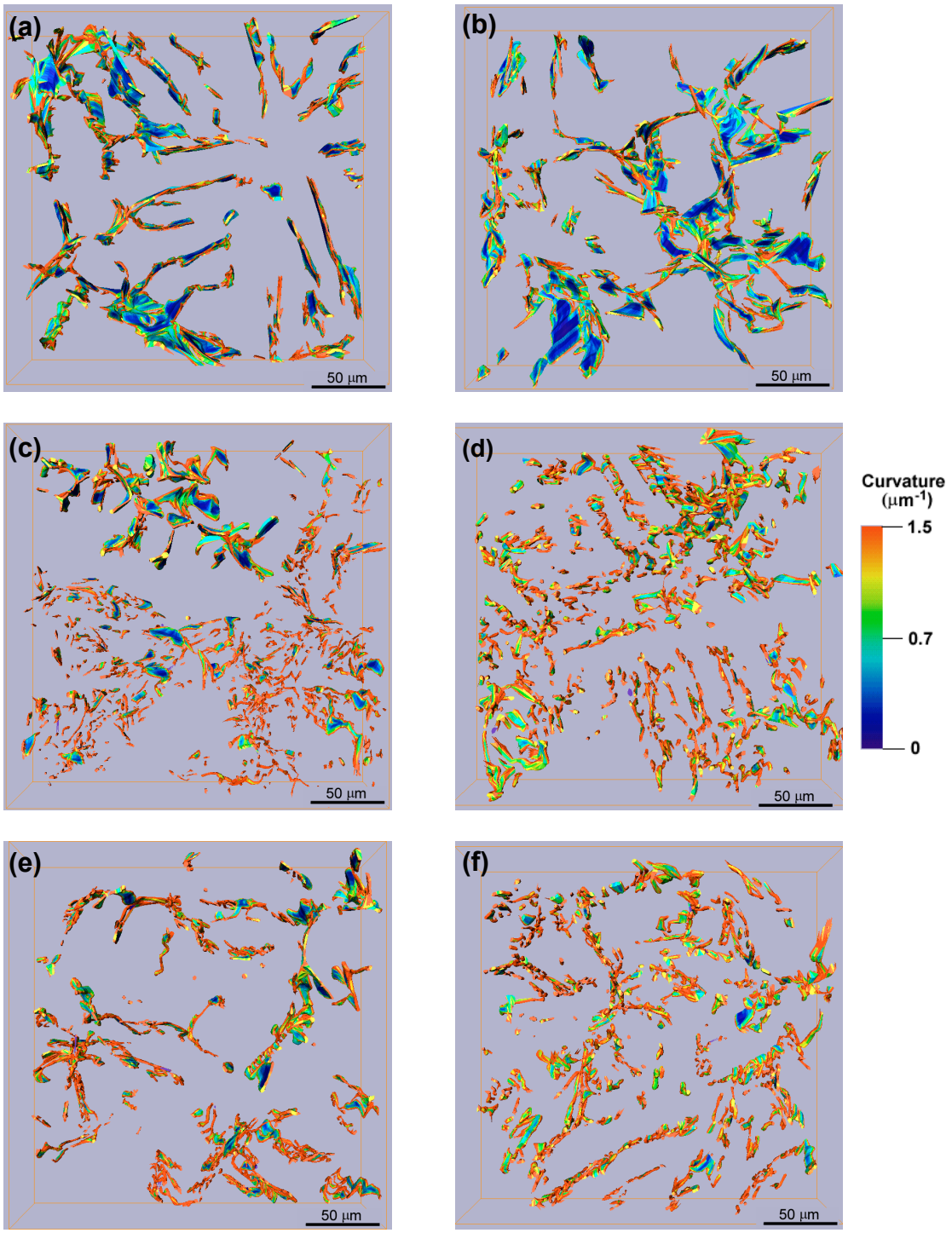

Figure 5.5 Colour coded images showing curvatures for the structures shown in Figure 5.3. (a) as-cast, (b) 30 minutes homogenised at 540°C, (c) 8 hours homogenised at 540°C, (d) 32 hours homogenised at 540 °C, (e) 1 hour homogenised at 590 °C, (f) 32 hours homogenised at 590 °C. The indicated boxes have a dimension of 200×200×40 µm for all pictures.

5.3.3 Quantification using local curvature

Figure 5.5 shows the 3D reconstructions of the structures in Figure 5.3 after quantification of the local curvature. The variations in local curvature are denoted by a

colour scale. These figures show a change of the intermetallic curvature distribution during the homogenisation process. The blue colour corresponds to a flat surface (low curvature) whereas the red colour indicates a round surface (high curvature).

Figure 5.6 compares the frequency distribution of absolute curvatures as determined for five samples. This figure shows, with the exception of the sample homogenised for 8 hours at 540°C, that the density of high curvature increases and the density of low curvature decreases at longer homogenisation times. The peak shift to the right and change in distribution (less skewed) indicates an increased curvature and a new curvature distribution. Also, the maximum curvature of the intermetallics for the cast homogenised state is not equal to zero, but equal to approximately 0.4 μm^{-1}. This implies that on average the β plates are not truly flat, but show local curvature fluctuations, as would be expected. The curvature distribution of the two first states, as-cast and 30 minutes homogenised at 540°C, is equivalent, which indicates that only a limited morphological change occurs during the early stage of transformation from β-Al_5FeSi to α_c-$Al_{12}(FeMn)_3Si$. At intermediate homogenisation times, which yield partial transformation, a more complex distribution, showing two maxima, is obtained. This can be explained by contribution from the curvatures of both α_c-$Al_{12}(FeMn)_3Si$ and β-Al_5FeSi phases in a normal distribution. Figure 5.7 shows the absolute curvatures for the β-Al_5FeSi phase, the α_c-$Al_{12}(FeMn)_3Si$ phase, and the addition of curvatures of β-Al_5FeSi and α_c-$Al_{12}(FeMn)_3Si$, in a sample homogenised for 8 hours at 540°C.

The distribution of the curvature for the β-Al_5FeSi phase presents two peaks centred on 0.4 μm^{-1} and 1.6 μm^{-1} respectively. The first peak indicates a low curvature which corresponds to the mean value found previously for the absolute curvature of the as-cast

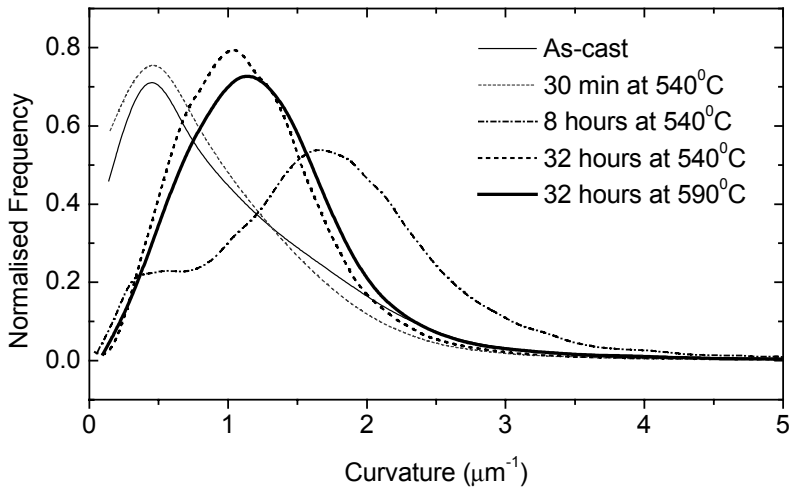

Figure 5.6 Frequency plot of the absolute curvature for the complete homogenised series.

and 30 minutes homogenised at 540°C samples. The second peak indicates a high mean curvature which is characteristic for a cylindrical or spherical morphology. Therefore, the first peak of the β-Al_5FeSi particles in a partially transformed sample corresponds to the β-Al_5FeSi intermetallics which remain untransformed. The second peak corresponds to the β-Al_5FeSi plates which have broken up to form more cylindrical shapes during the phase transformation of β-Al_5FeSi to α_c-$Al_{12}(FeMn)_3Si$.

The distribution of the absolute curvature for the α_c-$Al_{12}(FeMn)_3Si$ phase reveals one single peak centred on approximately 1.6 μm^{-1}, which is characteristic of a spherical or cylindrical shape. This curvature is higher than the curvatures observed for the completely transformed α particles (see Figure 5.6). Probably the initial small sizes of the α_c-$Al_{12}(FeMn)_3Si$ phase yield a higher curvature of the α particles.

Figure 5.8 provides a comparison of the absolute curvature distributions for two samples with the same fraction transformed but obtained for different homogenisation conditions: one sample has been homogenised for 1 hour at 590°C whereas the other has been homogenised for 32 hours at 540°C. The distribution of the absolute curvature for these samples is slightly different. The maximum peak of the absolute curvature is centred, in both cases, on approximately 1 μm^{-1}. However, the sample homogenised for 1 hour at the higher temperature of 590°C exhibits a shift in the distribution to higher absolute curvatures than the sample homogenised for 32 hours at 540°C.

5.3.4 Quantification using Gaussian and mean curvatures

Figure 5.9a and b show the distribution of the Gaussian and the mean curvatures for the homogenised series investigated. From these graphs and based on the surface interpretation of the Gaussian and the mean curvature (Table 5.3), the pattern of morphological evolution of the intermetallic phases can be determined in greater detail.

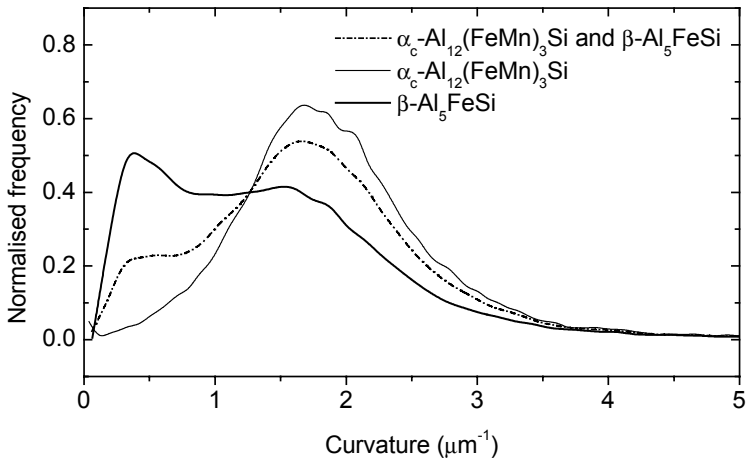

Figure 5.7 Frequency plot of the absolute curvature for the sample partially homogenised for 8 hours at 540°C.

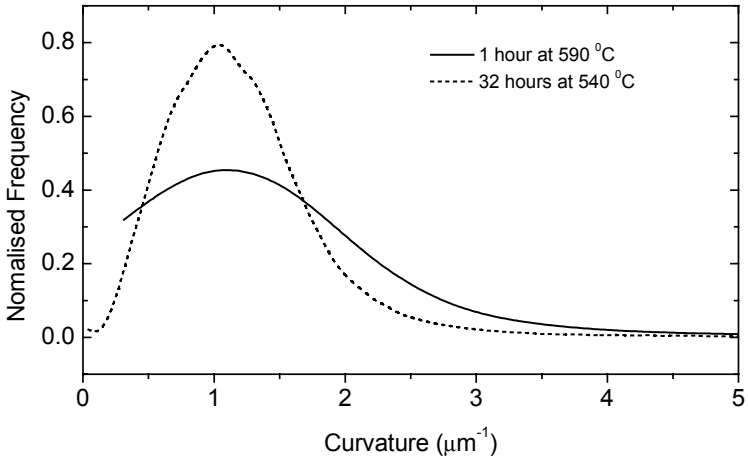

Figure 5.8 Frequency plot of the absolute curvature for the sample homogenised for 1 hour at 590 °C and 32 hours at 540°C.

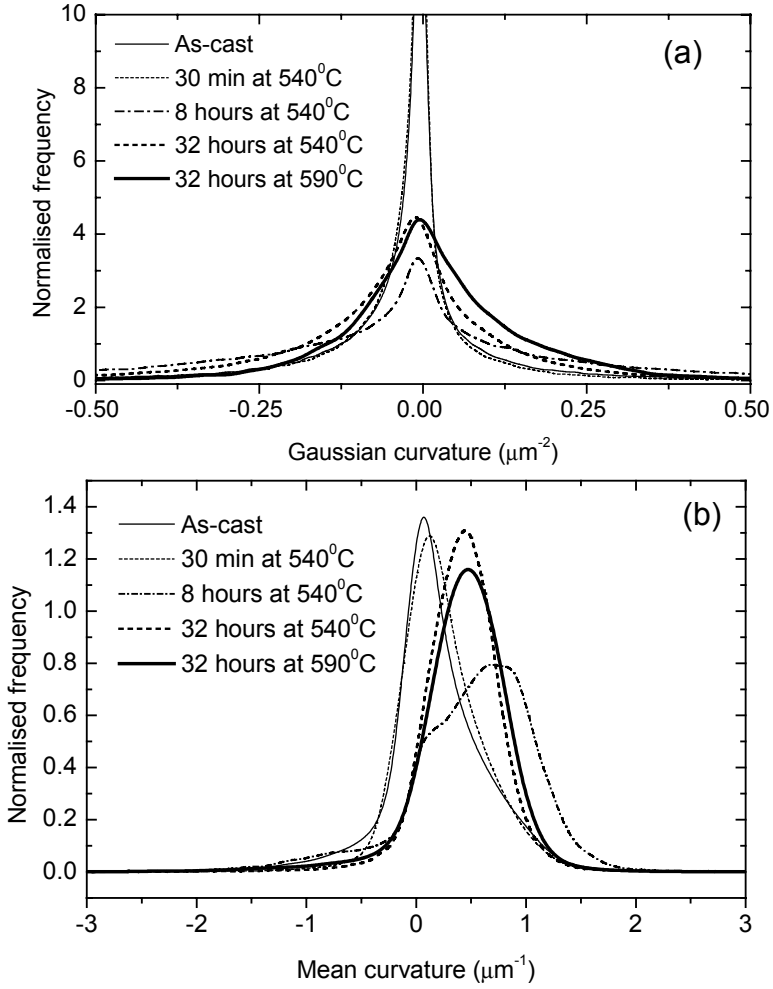

Figure 5.9 Frequency plot of (a) the Gaussian curvature, (b) the mean curvature for the complete homogenised series.

The distribution of the Gaussian curvature (Figure 5.9a) is centred almost on zero for all the samples investigated which implies that the average morphology for the intermetallics is planar if the mean curvature is also equal to zero or cylindrical if it is not. The distribution of the mean curvature (Figure 5.9b) changes with the degree of homogenisation and the homogenisation temperature. The as-cast sample and the sample lightly homogenised for 30 minutes at 540°C have a symmetrical mean curvature distribution centred on zero, which suggests an elongated surface which is slightly rippled, as was expected from the plate-like morphology of the β-Al_5FeSi. The distribution is biased towards the positive scale for the heavily homogenised (32 hours at 590°C and 540°C) and partially homogenised samples (8 hours at 540°C), which implies an average convex surface. These observations indicate that a major morphological change of the intermetallics occurs during homogenisation for between 30 minutes and 8 hours at 540°C.

Table 5.5 shows an evaluation according to the sign of the Gaussian and the mean curvature of the intermetallic morphology for the samples homogenised under different conditions

Table 5.5 Surface interpretation of the homogenised series according to the sign of the Gaussian and mean curvature.

Sample	mode of Gaussian curvature (K)	mode of mean curvature (H)	Morphology According the sign of K and H
As cast	0.0 μm^{-2} (strong peak)	0.0 μm^{-1}	strongly plate-like
30 minutes at 540°C	0.0 μm^{-2} (strong peak)	0.0 μm^{-1}	strongly plate-like
8 hours at 540°C	0.0 μm^{-2} (low peak)	1.0 μm^{-1} (low intensity)	cylindrical with a widespread distribution of radii
32 hours at 540°C	0.0 μm^{-2}	0.5 μm^{-1}	cylindrical
32 hours at 590°C	0.0 μm^{-2}	0.5 μm^{-1}	cylindrical

Figure 5.10a and 5.10b show the distribution of the Gaussian and mean curvatures for the sample partially homogenised for 8 hours at 540°C. The contributions of phases β-Al_5FeSi and α_c-$Al_{12}(FeMn)_3Si$, have been separated and analysed separately. The maximum in the distribution of the mean curvature for the β-Al_5FeSi phase is centred on zero, whereas the distribution for the α_c-$Al_{12}(FeMn)_3Si$ phase is positively biased and centred on 0.75μm^{-1}. These observations allow us to conclude that the morphology of the β-Al_5FeSi phase in this state is still plate-like whereas the morphology of the α_c-$Al_{12}(FeMn)_3Si$ phase appears to be convex due to growth of the α_c-$Al_{12}(FeMn)_3Si$ nuclei.

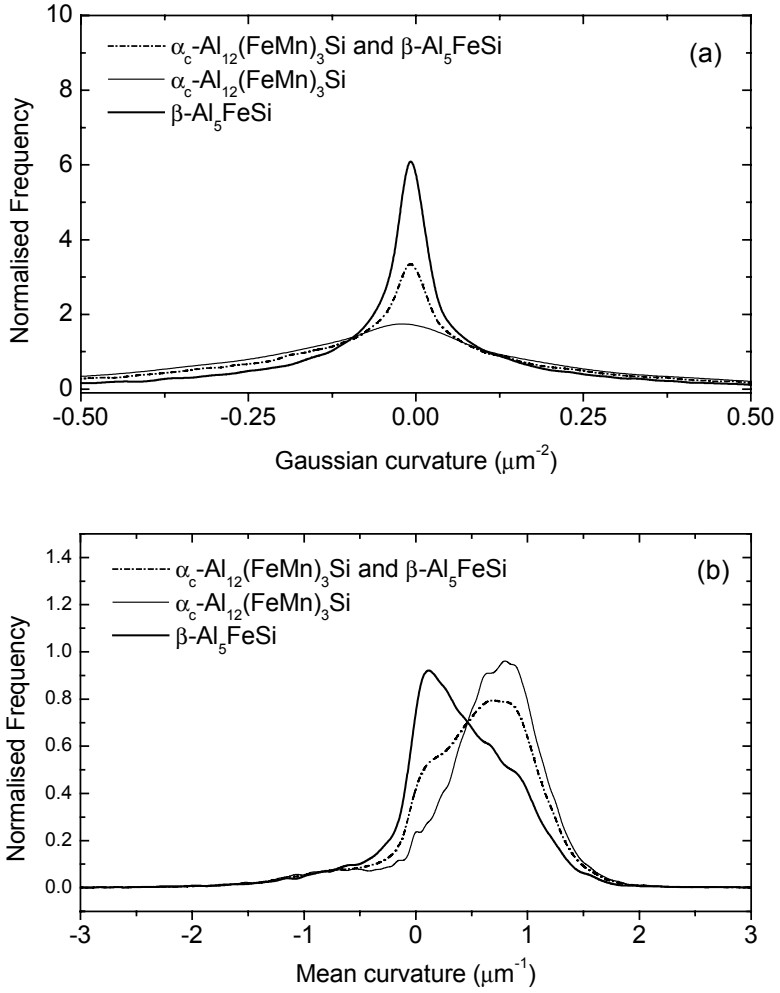

Figure 5.10 Frequency plot of (a) the Gaussian curvature, (b) the mean curvature for the sample homogenised for 8 hours at 540°C.

Table 5.6 Surface interpretation of the Gaussian and the mean curvature signs for the sample partially homogenised for 8 hours at 540°C.

	mode of Gaussian curvature (K)	**mode of mean curvature (H)**	**Morphology according to the sign of K and H**
β-Al_5FeSi phase	0.0 μm^{-2} (strong peak)	0.0 μm^{-1}	plate-like
α_c-$Al_{12}(FeMn)_3Si$ phase	0.0 μm^{-2} (low peak)	1.0 μm^{-1}	cylindrical-like

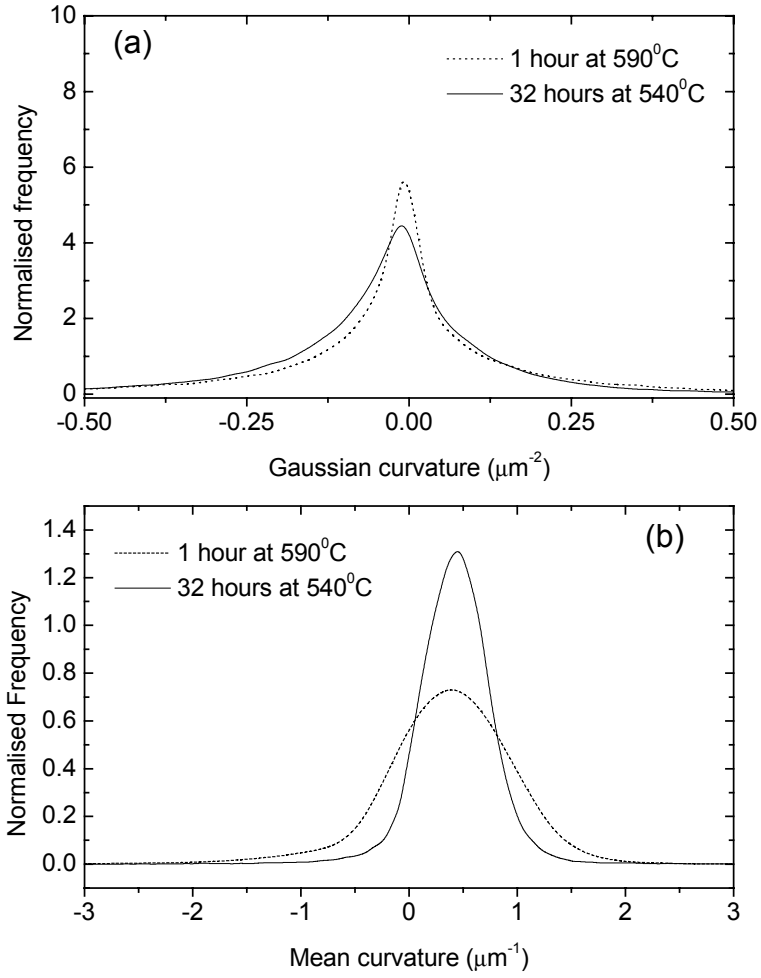

Figure 5.11 Frequency plot of (a) the Gaussian curvature, (b) the mean curvature for the samples homogenised for one hour at 590°C and 32 hours at 540°C.

Table 5.7 Surface interpretation for samples heavily homogenised at different temperatures

Sample	Gaussian curvature with highest appearance (K)	mean curvature with highest appearance (H)	Morphology According the sign of K and H
Homogenised for 1 hour at 590°C	0.0 μm^{-2}	0.5 μm^{-1} (strong peak)	cylindrical-like with wide spread radius- distribution
Homogenised for 32 hours at 540°C	0.0 μm^{-2}	0.5 μm^{-1} (low peak)	cylindrical-like with narrow radius distribution

Table 5.6 shows an evaluation of the intermetallic morphology for the sample partially homogenised for 8 hours at 540°C according to the sign of the Gaussian and mean curvatures. The average morphology corresponding to the α_c-$Al_{12}(FeMn)_3Si$ phase is cylindrical, whereas for the β-Al_5FeSi phase the morphology is strongly plate-like.

Figure 5.11a and 5.11b show the mean and the Gaussian curvature for the samples heavily homogenised for 1 hour at 590°C and 32 hours at 540°C, respectively. These samples correspond to two different homogenisation conditions which lead to the same fraction transformed, 80%.

Table 5.7 represents the interpretation of the morphology according to the sign of the Gaussian and mean curvature for these two samples. The sample homogenised at 540°C and 590°C both have a cylindrical morphology. However, at 590°C the intermetallics have a narrower radius distribution.

5.4 Discussion

If the different observations, quantifications and calculations are linked together, the morphological evaluation of the intermetallic microstructure for each homogenised state can be made with a high accuracy. The phase transformation from β-Al_5FeSi to α_c-$Al_{12}(FeMn)_3Si$ phase, which occurs during heat treatment, plays an essential role in the overall morphological change of the microstructure. The morphological evolution of the intermetallics during the homogenisation heat treatment give some indication of the stages occurring during the transformation process. Such data are crucial as input transformation models and model validation.

The results showed that for homogenisation at 540°C the transformation occurs in a three stages, indicated by (A), (B) and (C):

(A) In as-cast samples, plate-like intermetallics are present and, in the early stages of transformation (up to 20%) the plate-like shape of the intermetallics is still pronounced. The calculation of the area-to-volume ratio gives valuable information regarding the morphologies in the lightly and heavily homogenised states. The thickness of the plates for the as-cast and 30 minutes homogenised at 540 ºC conditions is approximately the same (0.46 and 0.40 μm), which indicates that the β-plates break up only at the edges during the β-Al_5FeSi to α_c-$Al_{12}(FeMn)_3Si$ phase transformation. The plate-like morphology of the β–Al_5FeSi plates for the partially transformed sample is in line with previous recorded LSCM observations on deep etched samples which showed plate-like β-Al_5FeSi intermetallics with rounded nuclei of α on the edges and on the faces (see Chapter 3).

(B) At an intermediate transformation stage (50%), the small α nuclei start to grow on top of the β-Al_5FeSi plates. Observations showed that those α particles have a mode absolute curvature of 1.6 μm^{-1}, corresponding to diameters of 0.6 μm. The results in Figure 5.10 showed that those α_c-$Al_{12}(FeMn)_3Si$ phases are already cylindrical at this stage of transformation, however the weak peak in the Gaussian curvature distribution in Figure 5.10a reveals that the cylindrical shapes remains a wide range of morphologies.

(C) Late in transformation the α_c-$Al_{12}(FeMn)_3Si$ particles become clearly cylindrical and the connectivity decreases. The mode of absolute curvature of the α particles decreases to 1 μm^{-1}; thus the radius of the particles increases. For the heavily homogenised (80% transformed) and fully homogenised samples it can be see that the diameters of the cylinders are comparable, which indicates that the morphology of the intermetallics does not change for the range of 75-100% transformed.

The effect of the temperature on homogenisation was shown in Figure 5.11 for two samples with the same fraction transformed. Although the peak positions of the frequencies of mean curvature are approximately the same for both temperatures, the radius distribution is narrower for the lower temperature (540°C). This is also clearly visible in the 3D Figure 5.11d and e, showing that the structure at 540°C is finer and less connected than at 590°C. Although this is an observation based on limited data, it nevertheless implies that homogenisation temperature has an influence on the morphological evolution during heat treatment.

5.5 Conclusions

The 3D characterisation technique by serial sectioning provides qualitative and quantitative data regarding the morphology of the metallic microstructure that would be impossible to obtain by 2D analysis.

The morphology of the intermetallics at the early stages of the transformation of β-Al_5FeSi to α_c-$Al_{12}(FeMn)_3Si$ is predominantly plate-like and interconnected. Nucleation of the α_c-$Al_{12}(FeMn)_3Si$ phase occurs on the initial β-Al_5FeSi plates. In the first half of the transformation these nuclei grow and the β-Al_5FeSi plates break up at their edges. This will lead to both growth of the α_c-$Al_{12}(FeMn)_3Si$ and morphological evolution of the β-Al_5FeSi.

In the second half of the transformation the initial α_c-$Al_{12}(FeMn)_3Si$ nucleus become more cylindrical and the connectivity decreases dramatically. Nevertheless, the morphology has stabilised to a cylindrical morphology for the α_c-$Al_{12}(FeMn)_3Si$ particles. The spatial distribution of the α_c-$Al_{12}(FeMn)_3Si$ cylinders still closely reflects the spatial distribution of the original β-Al_5FeSi plates.

References

[1] S. Zajac, B. Hutchingson, A. Johanssons and L. O. Gullman: *Microstructure control and extrudability of Al-Mg-Si Alloys microalloyed with manganese.* Mat. Sci. Tech. **10** (1994) 323-333.

[2] H. Tanihata, T. Sugawara, K. Matsuda and S. Ikeno: *Effect of casting and homogenizing treatment conditions on the formation of Al-Fe-Si intermetallic compounds in 6063 Al-Mg-Si alloys.* J. Mater. Sci. **34** (1999) 1205-1210.

[3] A. Griger and V. Stefaniay: *Equilibrium and non-equilibrium intermetallic phases in Al-Fe and Al-Fe-Si alloys.* J. Mater. Sci. **31** (1996) 6645-6652.

[4] S. Onurlu and A. Tekin: *Effect of heat-treatment on the insoluble intermetallic phases present in an AA-6063 alloy.* J. Mater. Sci. **29** (1994) 1652-1655.

[5] J. Alkemper and P. W. Voorhees: *Three-dimensional characterization of dendritic microstructures.* Acta Mater. **49** (2001) 897-902.

[6] M. V. Kral and G. Spanos: *Three-dimensional analysis of proeutectoid cementite precipitates.* Acta Mat. **47** No. 2 (1999) 711-724.

[7] D. N. Hanlon, I. Todd, W. M. Rainforth and S. van der Zwaag: *The application of laser scanning confocal microscopy to tribological research.* Wear. **251** (2001) 1159-1168.

[8] D. A. Drew: *Evolution of geometric statistics.* J. Appl. Math. **50** (1990) 649-653.

[9] R. W. I. Yarger and F. K. H. Queck: *Surface parameterization in volumetric images for feature classification.* In: IEEE International Symposium of Bio-Informatics and Bio-Engineering, BIBE 2000, Washington D.C. (2000) 297-303.

Chapter 6

A model of the β-to-α transformation in Al-Mg-Si alloys

In this chapter a finite element model is presented which models the development of α-fraction during the first stage of the β-to-α transformation as a function of homogenisation temperature, as-cast microstructure and concentration of alloying elements. We treat the β-to-α transformation mathematically as a Stefan problem, in which the position of the moving boundaries of the α and β particles are determined. To define the appropriate boundary conditions at the interfaces, thermodynamic databases are used. The influence of several process parameters, such as the temperature and initial thickness of the β plates, on the modelled transformed fraction is investigated. The finite element model and a simplified analytical model are compared, and the model is validated against experimental data.

6.1 Introduction

Chapter 2 to 5 showed experimentally that during the homogenisation process, plate-like monoclinic intermetallic β-Al_5FeSi particles transform to multiple rounded α-$Al_{12}(Fe_xMn_{(1-x)})_3Si$ particles [2-4]. Many process parameters, such as homogenisation temperature [7], as-cast microstructure [8], and chemical compostion [9] influence the β-to-α transformation rate. It is interesting to make a model that describes the morphological evolution of the interemetallic transformation and which is able to derive the influence of those process parameters on the transformation rate.

The morphological change of the intermetallics during the homogenisation treatment has been described in a few papers and was also invesigated in this thesis. In Chapter 3 and 4 it was found that, in the early stage of transformations, α particles were nucleated on top and also on the rim of the β-plates [10,11]. Small α nuclei, with an average size

of half a micrometer, are observed on top of the β particles with a site density of approximately 0.2 μm^{-2}. Some of the particles observed were facetted whereas others exhibited a more rounded morphology. During the transformation, the β-AlFeSi phase is observed to remain plate-like with an approximately constant thickness [4], leading to the conclusion that the β plate only dissolves at the rim, injecting Fe and Si into the Al-matrix. At a later stage of the transformation, the α particles will grow as spheres with possibly fingering as a side-effect [4]. In Chapter 4 it was showed that the interface between the α-particle and β-plate, does not move. Hence, there is no mass transport across the interface between the α-particle and β-plate. Since the α particles grow by adsorption of Si, Mn and/or Fe, those elements must have been transported through the Al-matrix.

Until now, no physically based models have been found in the literature which predict the fraction transformed of the β-to-α transformation. Hence, modelling this transformation and looking at the influence of the process parameters poses a new challenge.

The β-to-α transformation can be mathematically treated as a Stefan problem [12], where the concentration satisfying the diffusion equation and the position of the moving boundaries of the α and β particles are determined. The model is based on the conservation of mass. Some papers that study particle dissolution and growth by determination of the solution of a Stefan problem are due to, among many others, Whelan [13], Aaron and Kotler [14], and Tundal and Ryum [15]. In these papers it is assumed that the interface moves due to diffusion of one alloying element only, i.e. binary alloys. Furthermore these models are restricted to one space dimension and one moving interface. During the β-to-α transformation which is studied here, the interface movement is derived by the simultaneous diffusion of several alloying elements with two moving interfaces. This gives a "vector-valued" Stefan problem, where the concentration fluxes of consecutive alloying elements are such that all the alloying elements are conserved. This is explained in more detail by Reiso *et al.* [16], Hubert [17], Vitek *et al.* [18] and Vermolen *et al*. [19,20]. The ideas from the model of Vermolen,[20] are used to obtain the boundary conditions of the alloying elements at the interfaces.

A different numerical approach for the β-to-α transformation is the phase-field approach, which is derived form a minimisation of the free energy functional. This approach has been used by Kobayashi [21] to simulate dendrite growth. A recent extension to multi-component alloys phase-field computation has been done by Grafe *et al.* [22], where solidification and solid state transformation are modelled. However, a disadvantage of the phase-field approach is that physically justifiable parameters in the

energy functional are not easy to obtain. Some of these quantitatives have to be obtained by using fitting procedures that link experimental and numerical computations.

In this Chapter, a model is proposed based on the hypothesis that the transformation is diffusion controlled. This model can only be used in the beginning of the transformation. The reasons for this are: firstly, in the beginning the overall morphology is still stable, whereas the intermetallics break up to cylindrical shapes at later stages. Secondly, if the dissolving β-rim meets the growing α-particle, our model is no longer applicable. Despite this limitation, the model could provide some idea of the homogenisation-time towards higher fractions (up to ~ 50%).

In this chapter, a finite element and an analytical approach are presented which model the development of fraction transformed with time, by simulating the growth of an α particle on a β plate. For the boundary conditions of the model thermodynamic calculations are used (Thermo-Calc). The transformation fraction is calculated for several input parameter values estimated from experimental observations. The influence of some process parameters on the transformed fraction, such as the temperature and initial thickness of the β plates, are investigated. The finite element model and the analytical model are compared, and finally the model is validated with experimental data. The dependence of the transformation rate on the alloy content is also an important extension of the model, and will be a described in more detail in Chapter 7.

6.2 The Model

6.2.1 Introduction

The as-cast microstructure is simplified in the Finite Element Model to a representative cell containing the Al-rich phase, a single α particle and a single β-plate, which have a specific form and size. Furthermore, the cell-size is chosen such that diffusion across cell-boundaries is negligible. Both a uniform and a spatially graded initial (at t=0) composition in the Al-rich phase can be assumed. For the present study only a uniform initial composition of the Al-rich phase is considered. It is assumed that the atoms of the alloying elements diffuse through the Al-rich phase. Further, atoms that originate from the α- and β-phase are assumed to cross the interface (α/Al phase or β/Al phase) at such a rate that bulk diffusion is the rate controlling step in the transformation. For clarity, we list the assumptions that we use to predict the rate of the β→α transformation.

Assumptions 1 *Main assumptions of model:*

1. Diffusion determines the rate of transformation, from mass-conservation a Stefan problem results to determine the displacement of the interfaces.

2. During the growth of the α particle chemical elements Fe, Mn, Si cross the α/Al interface. The β-plate only dissolves at the rim of the plate, hence the thickness of the β plate is constant during the transformation.
3. The initial concentrations of the alloying elements Fe, Mn, Si in the aluminium matrix surrounding the intermetallics (but not at interface itself), are determined by the Scheil solidification model [23].
4. The interface concentrations for Fe, Mn, Si are estimated by the use of the multi-component model of Vermolen *et al.* [20] for particle dissolution. The key assumption here is that the interface concentration of the different elements should satisfy the thermodynamic solubility relations and be such that the prediction of the interface displacement of a phase is equal for all chemical elements. This procedure is applied to both the interface of the α-particle and β-plate.
5. In the transformation model only diffusion of Fe is taken into account with the use of the boundary conditions as given in item 4. The difference between the chemical potentials of the Fe concentration on the α and β interface provides the rate limiting driving force of the β-to-α transformation.
6. The concentration of Si is uniform in the Al matrix during the entire transformation.

The rate of the transformation is assumed to be determined by diffusion of Fe (See assumption 1, item 5). It is known from experiments, that during the transformation Mn is also absorbed by the α particles. The Mn is supplied by the dissolved Mn in the Al-matrix, and is not supplied from the β-AlFeSi. Since the diffusion of Mn is slower than that of Fe, the Mn content stays constant in the early stages of the transformation. Hence the thermodynamic solubility of iron at the rim of the α particle is not affected. Therefore this Mn diffusion is only a secondary effect of the transformation, and hardly controls the rate of the transformation, which was also found by Alexander *et al.* for familiar phase transformations [24]. Therefore, in this model, the diffusion of Mn is neglected. The diffusion of Si is very fast [25], in comparison to diffusion of Fe, and therefore the silicon concentration will be distributed uniformly in the aluminium matrix rapidly (as stated in assumption 1, item 6).

We assume that the stoichiometry of both the α-phase and β-phase is constant at all stages of the transformation process. Further we neglect a potential Mn concentration in the α-particle, $Al_{12}(Fe_xMn_{1-x})_3Si$, hence x=1.

6.2.2 Solubility relations of Fe on the α and the β particles

The driving force of the diffusional β→α transformation is mainly determined by the difference between the chemical potentials of iron at the α- and β- interface.

$$\Delta\mu = \mu_\beta^s - \mu_\alpha^s \tag{6.1}$$

This difference in chemical potential, $\Delta\mu$, of the solute iron in the Al-phase close to the α (μ_α^s) and the β interface (μ_β^s), gives a diffusional transport of iron atoms towards the α-phase in the aluminium matrix. It is assumed that the interfacial reactions for the α- and β-phases are fast enough to reach a local thermodynamic equilibrium concentration in both aluminium/intermetallic interfaces. The chemical potential of Fe depends on the solute levels of other elements, such as Si and Mn, at the interface.

Since the model is based on Fick's law of diffusion (see also assumption 1, item 1), we use the differences of solute level between the α and β phases (Δc_{Fe}) as the driving force. Therefore, we use the thermodynamic software package Thermo-Calc (database TTAL for aluminium) to derive a relation between the equilibrium concentrations of the alloying elements at both the α- and β-interface.

Then, it is possible to estimate the interface concentrations on the interface of the α particle. For the investigated alloy composition in this study with high Mn content, a low iron equilibrium concentration at the interface was calculated (<0.005 wt.%) and therefore, the iron concentration on the α boundary was set to c_α^s=0 wt.% for all calculations. At lower alloy concentrations of Mn (<0.015 wt.%) a considerable increase of the solubility was found. In this case it is necessary to take the iron solubility on the α particle into account. The effect of Mn on the transformation rate will be described in Chapter 7.

To compute the interface concentration for the β-plate, the solubility product is determined from Thermo-Calc for several temperatures and expressed in an Arrhenius-relation:

$$c_{\beta\,Fe}^s c_{\beta\,Si}^s = A_\beta \exp\left(\frac{-Q_\beta}{RT}\right). \tag{6.2}$$

Here $c_{\beta\,Fe}^s$ and $c_{\beta\,Si}^s$ are the equilibrium concentrations (in wt.%) in the matrix on the interface of the β particle, A_β=59·10^3 and Q_β=111 kJ/mol. We derive an implicit relation for the initial interfacial concentration of the β-Al_5FeSi in the matrix [19]:

$$\frac{c_i^0 - c_i^s}{c_i^p - c_i^s}\sqrt{\frac{D_i}{\pi}}\frac{\exp\left(-\frac{k^2}{4D_i}\right)}{erfc\left(\frac{k}{2\sqrt{D_i}}\right)} = \frac{k}{2},\ for\ \ i \in \{Si, Fe\}, \tag{6.3}$$

where k is a constant. In equation (6.3) the c_i^0, c_i^p and D_i are the initial concentration in the matrix (wt.%), concentration in the particle (wt.%), and diffusion coefficient in the Aluminium matrix of element i. The parameter k originates from the solution structure for particle dissolution/growth in a planar unbounded domain [19]. It represents the rate parameter where $S(t) = S_0 + k\sqrt{t}$ defines the interface position as a function of time. Equations (6.2) and (6.3) give sufficient conditions for the determination of c_{Fe}^s, c_{Si}^s and k. The relation (6.3) gives the exact solution for the interface concentrations at the initial stages, for different geometries. It is assumed that the interface concentrations on the β-AlFeSi phase are constant in time and are equal to this initial interface concentration. The obtained c_{Fe}^s is used as a boundary condition for the β- phase in the calculations. Since $D_{Si} >> D_{Fe}$, it follows from equation (6.3) that $c_{Si}^s \approx c_{Si}^0$.

6.2.3 Geometry of model

For 6xxx alloys the α phase is stable with respect to the β phase. The nucleation of α-particles take place preferentially on the β/Al interface rather than in the aluminium matrix, since the activation energy for nucleation of α particles on the β/Al interface is lower [26] than the nucleation energy in the Al-matrix. Therefore our model considers only this heterogeneous nucleation of α-particles on the β/Al surface. Experimentally, a distribution of nucleation distances was found, but for the sake of simplicity we only take the mean nucleation distance as model input parameter.

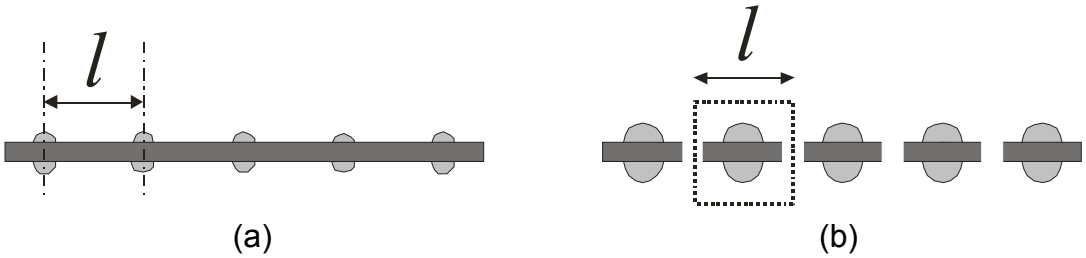

Figure 6.1 A scheme of (a) an β plate with initial α nuclei in the non-homogenised state (b) A broken β plate with consisting α particles on top. The domain of computation is situated in the picture.

The average plate length of the initial β-particles is approximately 20 μm, and the average nucleation distance is approximately 2 μm. It was found by experiment that β particles break up and transform to α-particles. Yet, it is not clear how the β plate breaks up during the transformation. In our model we propose that the β particles break up with the same length as the nucleation distance. This is illustrated in Figure 6.1. Figure 6.1a shows an initial β plate with α nuclei. Figure 6.1b shows the situation after a short homogenisation time: The β plate breaks up, and the α particles starts to grow. The domain of computation is indicated by the dotted box.

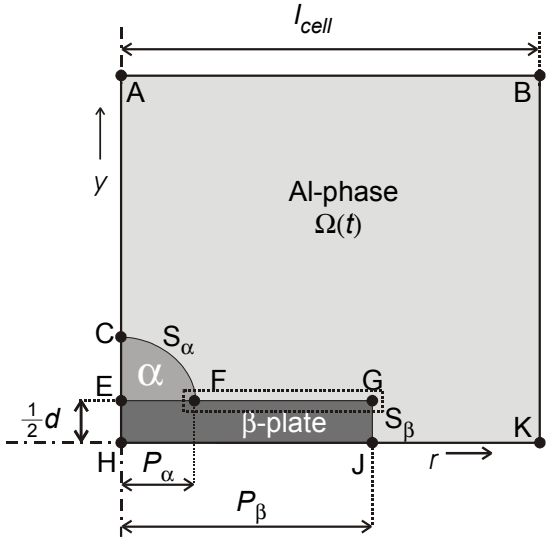

Figure 6.2 The geometry of the domain of computation of an α-particle on a β-plate in an Al-phase. The parameters are explained in the text.

Figure 6.2 shows the geometry of the model that mimics the growth of an α-particle on a dissolving β-plate. In the FE-Model we calculate an area with the size of $l_{cell} \times l_{cell}$. We assume cylindrical symmetry around the left vertical axis. A hemispherical α particle is situated on top of the plate-like β particle, and has a distance towards the rim of the β particle. The drawing is only schematic as the dimensions are not properly scaled according to those used in the calculations.

The aluminium phase is indicated in Figure 6.2 by the domain $\Omega(t)$, in which diffusion of the alloying elements takes place. The time dependence of this domain is induced by the moving boundaries of the α-particle and the β-plate. Those moving boundaries are expressed by the segment CF, defined as S_α, and the line segment GJ, defined as S_β. The unit normal vectors at the interfaces S_α and S_β, pointing outward from the aluminium matrix are denoted by $\mathbf{n}_\alpha$ and $\mathbf{n}_\beta$ respectively.

Line segment HK represents a symmetry line. Therefore the presented thickness of the β-plate in Figure 6.2 is only half of the modelled thickness of the β-plate, *d*. During this transformation this thickness remains constant, as also stated in assumption 1. Line segment AH represent the second symmetry line. For the Finite Element model, cylindrical co-ordinates are used, where the α-particle represents an hemi-spherical shape and the β plate represents a disc like shape in three dimensions. In the case of planar co-ordinates the α-particle represents an hemi-cylindrical shape and the β plate represents a rectangular shape in three dimensions.

6.2.4 The Finite Element Model.

In this section we present the Finite Element Model for dissolution of the β-plate and the growth of the α-particle which is based on the diffusion of iron only. The boundary conditions at the moving interfaces are determined from solution of equation (6.2) and (6.3) as described in Section 2.3. In the aluminium matrix, Ω(t), volume diffusion of iron is modelled by the non-steady state Fick-diffusion equation:

$$\frac{\partial c}{\partial t} = D_{Fe}\nabla^2 c \quad for \quad (r,y)\in \Omega(t), t>0. \tag{6.4}$$

Here *c* represents the Fe concentration of iron in the aluminium phase. *t* is the time of the homogenisation in seconds. From a local mass-balance of Fe over the interfaces, the equation of motion of the interface S_α and S_β is derived, leading to a Stefan condition. Let $v_\alpha(t)$ and $v_\beta(t)$ represent the velocity component perpendicular to the interface of the α and the β particle, respectively, then:

$$\left(c_i^p - c_i^s\right)\ v_i(t) = D_{Fe}\frac{\partial c}{\partial n_i} \quad for \quad (r,y)\in S_i(t), \quad i=\alpha,\beta. \tag{6.5}$$

The boundary of Ω(t) is divided into Γ_N (t), $S_\alpha(t)$ and $S_\beta(t)$. The part Γ_N (t) consists of the cell boundary (line segment CABKJ of Figure 6.2) through which we assume no diffusive transport for iron and the non-moving part of the β-plate (line segment FG of Figure 6.2), through which we assume no diffusive transport of iron either. On the

boundaries S_α and S_β the equilibrium concentrations c_α^s and $c_\beta{}^s$ are determined from equations (6.2) and (6.3) and hence they are prescribed in the Finite Element Model.
The presented mathematical problem has been implemented in the package SEPRAN, which has been developed at the Department of Applied Mathematical Analysis at the Delft University of Technology. The resulting Stefan problem is solved by the use of a moving grid method, where the grid is adjusted according to the interface movement. The interface movement is determined in a conservative way. The method is described in detail by Segal et al [27].

In the calculations it is assumed that the initial α-particle is spherical with radius r_α^{init} and that the initial β-plate is cylindrical with radius l. The Gibbs-Thomson effect only has a significant influence on the transformation kinetics when the radius of curvature is very small (typically in the order of nanometer). Since we consider only transformation behaviour in a micrometer-scale, we neglect the Gibbs-Thomson effect in the computations.

6.2.5 Analytical approach

The simplified new analytical approach (presented full in Appendix 3) is based on the assumption that diffusion in the horizontal direction (i.e. the r-direction) only plays a role (see Figure 6.2). To justify this, we show the concentration field, c(r,y), in the aluminium matrix in the vicinity of the interfaces. As the variation of the concentration in the vertical direction is very small (see Figure **6.3**), it is reasonable to assume that the second derivative in the y-direction is negligible. This motivates the one-dimensional approach. Just as in the FEM calculations, the analytical model is based on volume diffusion, where only diffusion close to the β-plate is considered, such that a one-dimensional Stefan problem arises. A further assumption is that the time dependence in the diffusion equation is negligible. We summarize this as follows:

Assumptions 2 *Main assumptions of analytical model:*

1 The growth of the α- and β–phases is determined by the derivation of the growth of the interface position of the α particle at the triple point F, and the rim point G of the β-plate (see Figure 2).
2 The rate of interface movement is negligible compared to the rate of diffusion in the α-matrix (steady state assumption).

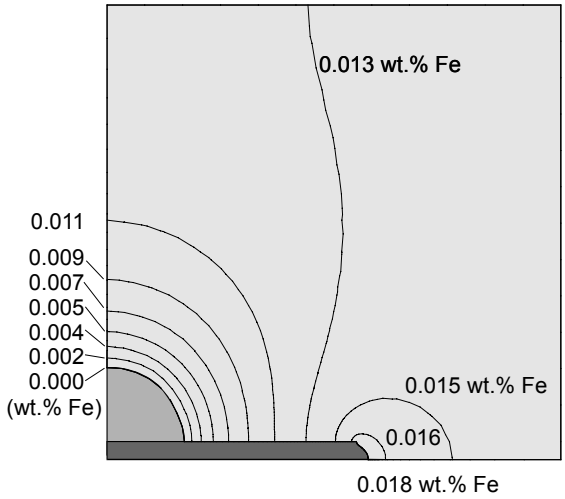

Figure 6.3 Iso-contour plot of concentrations of Fe in an cylindrical symmetric situation on an alloy homogenised for 60 minutes at 580 °C, as derived by FEM calculations. The model parameters are presented in Table 6.1.

A consequence of item 2.2, in the above assumption, is that the time derivative of the concentration field is neglected, i.e. on the β plate surface between the points F and G we have

$$\frac{D}{r}\frac{\partial}{\partial r}\left(r\frac{\partial c}{\partial r}\right)=0, \tag{6.6}$$

where the concentrations at F and G (see Figure 2) serve as boundary conditions.

Note that the Stefan-condition at these two points (see equation (6.5)) is satisfied, where n is replaced by the horizontal co-ordinate r. For both rectangular and cylindrical co-ordinates, analytical expressions for the positions of the α- and β interfaces were obtained. From these expressions the time at which the interfaces collide is determined. Since the expression for the collision time is relatively tractable for rectangular co-ordinates only, we give it to illustrate that this time t_{col} is proportional to the square of the initial distance between the reminiscent phases, $P_\beta - P_\alpha$:

$$t_{col}=\frac{(P_\beta-P_\alpha)^2}{2(c_\beta^s-c_\alpha^s)D_{Fe}\left((c_\alpha^p-c_\alpha^s)^{-1}+(c_\beta^p-c_\beta^s)^{-1}\right)} \tag{6.7}$$

The analytical solutions are compared with the Finite Element solutions in Section 6.4.3.

6.3 Experimental

An Al-Mg-Si alloy (AA 6005 A) with an alloy composition of 0.70 wt.% Mg, 0.83 wt.% Si, 0.27 wt.% Fe, and 0.18 wt.% Mn has been used for our investigations. All other chemical elements were present in weight percentages of at most 0.01 wt.%, hence their presence is ignored. The investigated alloy was DC-cast with a diameter of 254 mm respectively.

To investigate the α→β transformation rate, series of samples were homogenised at temperatures of 540°C, 570°C and 580°C for various times ranging between 10 minutes and 1 day. The samples were homogenised in an air circulation oven, for which the maximum temperature deviation over all locations in the oven is 3 °C. The samples were taken from the billet at locations between 10 mm and 30 mm from the rim of the billet. The microstructure of these samples, represent the typical microstructure of the billet. The experimental relative α-fraction was determined by using automatic SEM measurements in combination with Electron Dispersive X-ray Spectography (EDX). The α- and β- particles are classified by the difference of stoichiometric ratio of the total concentration of Fe and Mn versus the concentration of Si, which is determined by EDX. The method is described in more detail in Chapter 2.

At different distances of 20 mm, 50 mm and 75 mm from the rim of the billet, the mean dendrite arm spacing (DAS) has been determined. Each DAS value was determined by averaging 50 separate DAS-spacings determined from 5 optical micrographs on the same polished sample.

The samples were polished with ¼ silica and subsequently electro-etched at 20 V during 30 seconds in a mixture of 78 perchloric acid, 90 mL water, 730 mL ethanol and 100 mL butylglycol. SEM micrographs (JEOL 6500F) of these samples were used to measure the mean thickness of the β-plate. The thickness of the β-plates was determined by the use of SEM micrographs by averaging 50 individual thicknesses. The true thickness in 3D was taken to be π/4 times the average thickness from the cross sections images.

The nucleation distance between individual α particles was measured on two fully homogenised samples, either homogenised for 32 hours at 590 °C, or homogenised for 130 hours at 540°C. Each sample was polished with 1/4 Silica. Subsequently 20 optical micrographs were made on each sample. The distance between neighbouring α particles (l), which were located along a former β-plate, was determined by the use of the sketch of Figure 6.4. The nucleation distance in polished plain is obtained from $L/(n-1)$, where L represents the distance between the outside particles, and n is the number of particles on a sequence. The median nuclei distance, was determined by the use of 20

measurements of α-particles. The true nuclei distance in 3D, *l*, was taken to be ½ times the median nuclei distance from the measurements.

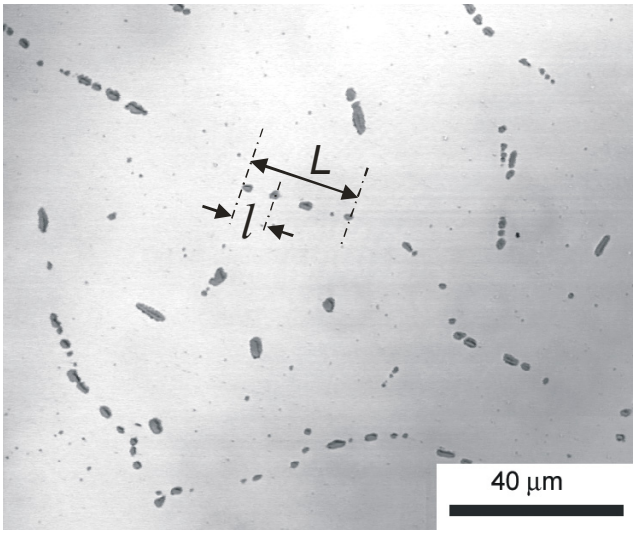

Figure 6.4 Microstructure of the fully homogenised sample at 590°C. The method of the determination of the distances between the beads of the α particles on the former β plate is showed.

6.4 Results and Discussion

6.4.1 Introduction

In this section, first a parameter study using the FEM model will be given. After this, the analytical model will be compared with the results of the FEM model. Then, the experimental results will be compared with the results obtained by the mathematical models. Finally the metallurgical implications will be given.

As a basis for the model calculations, parameters are used which are deduced from the actual alloy. Most of the simulations are done for an industrial temperature of 580°C, therefore the reported parameters are also obtained for this temperature (See Table 6.1). We used the literature values of the densities of Al, α and β phases [28] for the derivations of the concentration of Fe inside the α and β particles.

The Scheil [23,26] model derives the initial concentration of different elements in the Al-matrix close to the intermetallics. Since the FEM cell is relative small compared to the DAS, and is situated close to the intermetallics, it is assumed that the initial concentration is homogeneously distributed in this FEM cell and is equal to the derived concentrations. By Scheil calculations in Thermo-Calc, which use the compositions of

the experimental alloy as input, initial concentrations were found of c^0_{Fe}=0.02 wt.%, c^0_{Mg} = 0.6 wt.%, c^0_{Si} = 0.5 wt.% and c^0_{Mn} = 0.25 wt.%.

The concentrations on the interface of the β particles are determined by the multi-component model of equation (6.2) and (6.3). The geometric parameters, as presented in Table 6.1, are estimations from Chapter 3,4 and 5 [4,11]

Table 6.1 Basic physical parameters used for the model.

Parameter	Symbol	Value
Diffusion coefficient (at T=580°C)	D_{Fe}	0.0307 μm^2/s
Fe concentration in α particle [28]	c^p_α	39.9 wt.%
Fe concentration in β particle [28]	c^p_β	33.9. wt.%
Fe content on interface of α particle	c^s_α	0 wt.%
Fe content on interface of β particle	c^s_β	0.0183 wt.%
Initial radius of α particle	r^{init}_α	0.25 μm
Thickness of β-plate	d	0.2 μm
Diameter of initial β-plate	l	3 μm
Cell size of aluminium matrix	l_{cell}	2.5 μm
Initial iron concentration in matrix	c^0_{Fe}	0.0200 wt.%
Temperature	T	580°C

6.4.2 Parameter study using the FEM model

The influence of the physical parameters on the transformed fraction during time is investigated. Here the relative fraction of the α particles with respect to the total amount of intermetallics, is of special interest, since this is an indication of the extrudability of the material, and can also be compared with measurements from experiments. The relative α-fraction, f_α, is defined as:

$$f_\alpha := \frac{Volume(\alpha)}{Volume(\alpha)+Volume(\beta)}, \tag{6.8}$$

where *Volume(α)* is the volume of the α intermetallics and *Volume(β)* is the volume of the β intermetallics. Since the model is set up for transformations in the early state, it will only be used until the α-particle reach the rim of the β particle. Investigations will be performed on the influence on the α-fraction by variation of the geometry of the α-

particle, variation of the geometry of the β particle, variation of the matrix, and variation of the temperature.

A. Variation of the size of the α particle

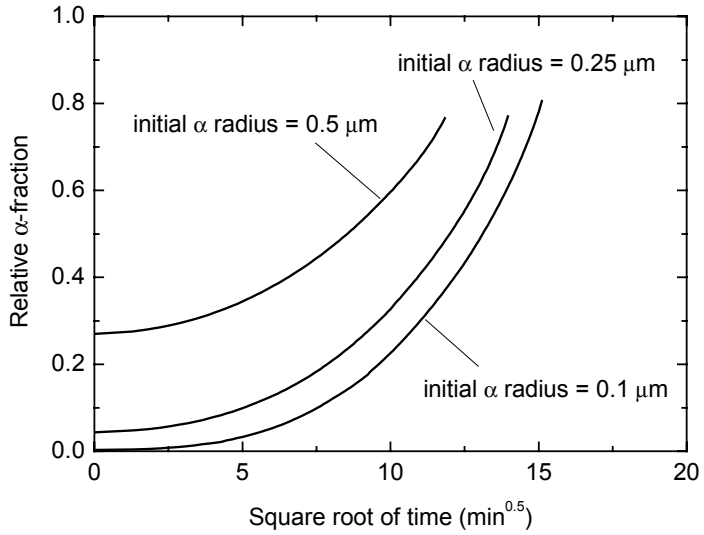

Figure 6.5 The relative α-fraction as a function of time for different initial particle radii, as computed by the Finite Elements Model. The other model parameters are presented in Table 6.1.

In Figure 6.5 the relative α-fraction as a function of time, for some modelled microstructures with different initial radii of the α particle is plotted. For all other model parameters, the values are used as presented in Table 6.1. The presented α radii cover the range of observed α particle sizes on β particles as observed in Chapter 4. The figure shows that the effect of the initial particle size is significant. By the nature of the definition of the relative α-fraction f_α, a larger initial particle radius gives already a larger initial relative α-fraction in the cast condition (t=0). Although the initial α-volumes vary widely in this numerical experiment, the α-fraction at the point of collision is approximately the same for all conditions, and the time to reach this impingement differs relatively slightly.

B. Variation of the β particle

The particle size of the intermetallics depends strongly on the solidification conditions. Fast cooling leads for example to thinner β particles. To show its effect on the homogenisation, in Figure 6.6 the relative α-fraction as function of time is plotted for

several values of thickness of the β-AlFeSi plate. For all other parameters values as in Table 6.1 are used. Figure 6.6 shows that with a thin β plate already have an initially higher relative α-fraction. (A larger plate thickness gives a larger initial plate volume and hence the initial relative α-fraction is smaller.) Figure 6.6 also shows that the time of impingement is approximately the same for all β thicknesses. Therefore the velocity of the movement of the α to the β must be approximately equal for all cases. On the other hand, the relative α-fraction at impingement is highly dependent on the β-thickness.

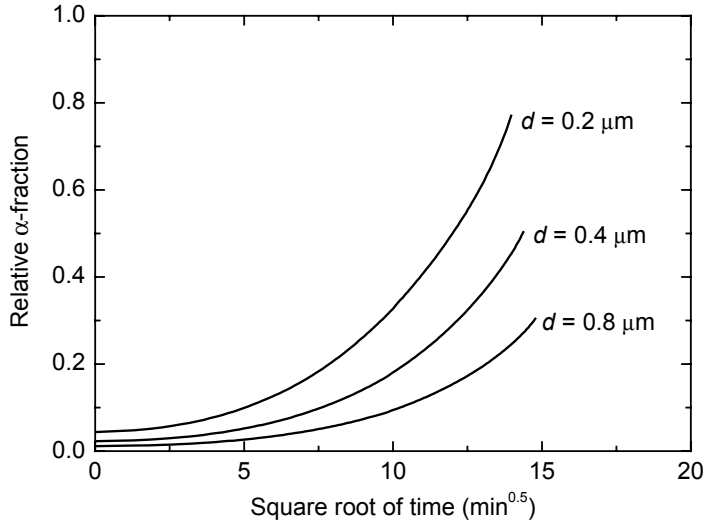

Figure 6.6 The relative α-fraction as a function of time for consecutive β-plate thicknesses, as computed by the Finite Elements Model. The other model parameters are presented in Table 6.1.

In Figure 6.7 the relative α-fraction as a function of time is given for several values of the initial radius of the β plate. This radius can be interpreted as the nucleation distance between the α particles, and therefore the average distance of the α plate towards the rim of the β plate. Again, the figure shows that the effect of the size of the β plate on the transformation is significant. Figure 6.7 shows that, as induced by the definition of the relative α-fraction, situations with a large initial radius gives a small initial relative α-fraction. The time of impingement is strongly dependent of the initial β plate radius. Smaller β plates impinge earlier, which is clearly visible in the figure. Also the relative α-fraction of impingement is higher as the initial β plate becomes larger.

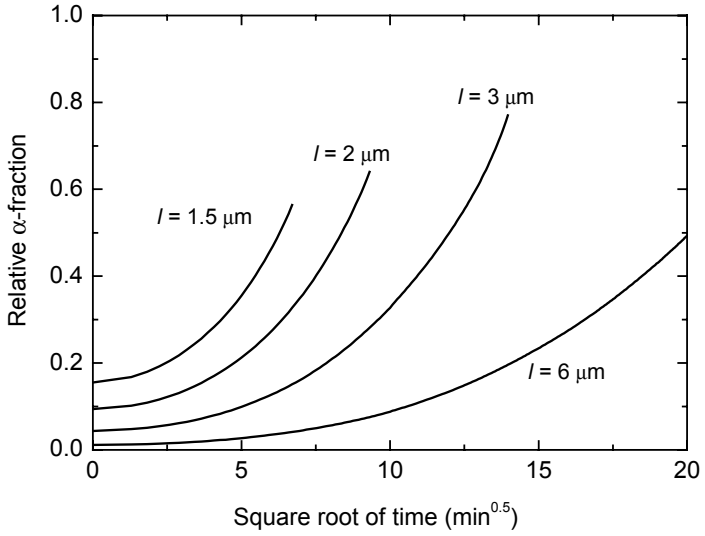

Figure 6.7 The relative α-fraction as a function of time for consecutive initial β-plate radii, as computed by the Finite Elements Model. The other model parameters are presented in Table 6.1.

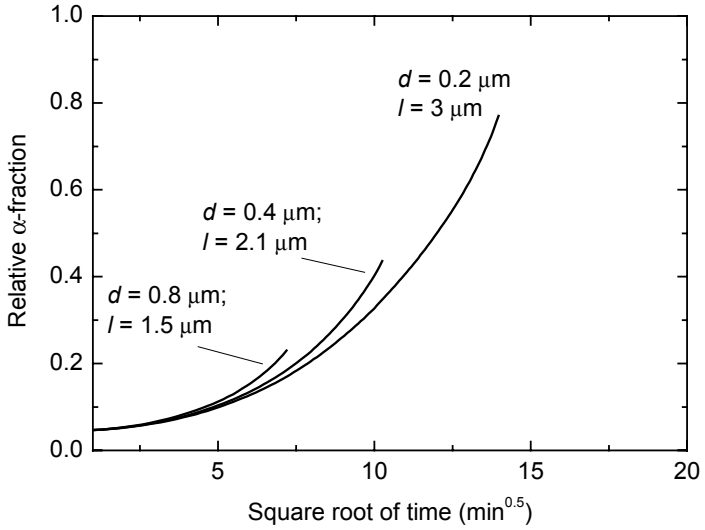

Figure 6.8 The relative α-fraction as a function of time for consecutive aspect ratio's of the β plate, as computed by the Finite Elements Model. The consecutive thicknesses (*d*) and diameters (*l*) of the β plates are indicated in the graph. The other model parameters are presented in Table 6.1.

In Figure 6.8 the relative α-fraction as function of time is plotted for several values of the aspect ratio of the β plate, such that the initial volume of the β plate is the same for all curves. It can be seen that the influence of the initial β-plate thickness and initial β-plate radius compensate each other, and therefore the relative α fraction during time is almost equal. As may be expected from the assumptions, the collision time of the α

particle and the β rim increases considerably for larger β-plate radii and the model breaks down at a later stage.

C. Variation of the matrix

Calculations with different cell sizes reveal that the influence of the cell-size on the transformation rate is not significant. The results of these computations are not shown here. We conclude that the cell-size hardly influences the transformation kinetics.

The used cell-size is correlated to the DAS of an alloy. Since the measured DAS spacing of most of the 6xxx alloys are in the order of 20 μm, thus larger than the β-plate sizes, it can be concluded that variations in the DAS have little influence on the transformation speed of the intermetallics.

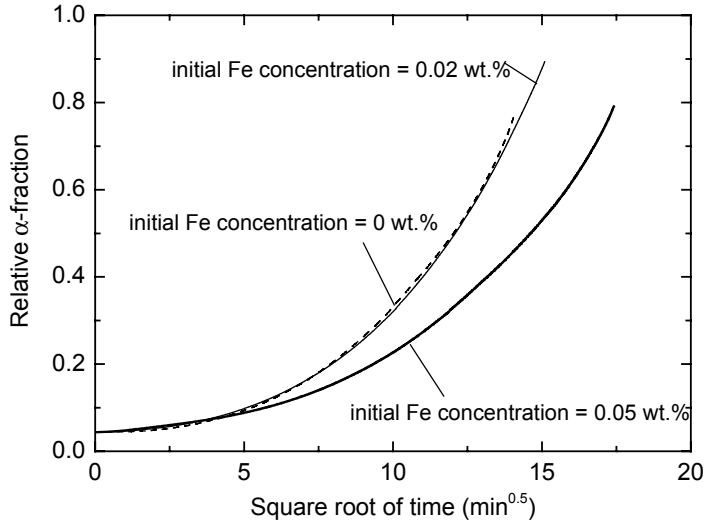

Figure 6.9 The relative α-fraction as a function of time for consecutive initial Fe concentrations in the Aluminium matrix, as computed by the Finite Elements Model. The other model parameters are presented in Table 6.1.

The Scheil-model on the AA 6082 alloy composition gives an initial iron concentration of c_{Fe}^{0}=0.02 wt.% close to the β-AlFeSi intermetallics. Since the Scheil model is based on ideal solidification, it is useful to investigate the effect of other initial solute iron concentrations. Figure 6.9 present the relative α-fraction as a function of time for several values of the initial iron concentration in the Al-matrix. The figure shows that cases with initial iron concentrations between 0 and 0.02 wt.% Fe give approximately the same kinetics. A higher initial Fe concentration, of 0.05 wt.% will slow down the transformation. In this case, the initial Fe concentration in the Al-matrix exceeds the solubility on the rim of the plate, leading to an initial growth rather than

shrinkage of the β plate. Although this effect seems unrealistic in 6xxx alloys, growth of β plates has been observed in other alloy systems [29].

D. Variation of temperature

Figure 6.10 shows the β →α transformation as computed for various temperatures. The input conditions for the various temperatures are taken from Table 6.1. Both the solubility at the interface ($c^s_{\beta Fe}$) and the diffusion coefficients of the chemical elements are functions of temperature. By using the multi-component model and solubility product (Eq. (6.2) and (6.3)), the solubility on the interface can be calculated and results are listed in table 6.2 for the relevant temperatures. As was discussed in Section 2.2, the table shows that the main difference in solubility is in $c^s_{\beta Fe}$ and the solubility of silicon approximately equals the concentration of the matrix, *i.e.* $c^s_{Si} \approx c^0_{Si}$. For the calculations of the solubility, the Arrhenius relation of the diffusion coefficient is used with pre-factor of $D_{0\,Si} = 2.02 \cdot 10^{-4}\ \mathrm{m^2 s^{-1}}$ and activation energy $Q_{Si} = 123.9$ kJ/mol for the diffusion of Silicon, [25] and pre-factor $D_{0\,Fe} = 5.3 \cdot 10^{-3}\ \mathrm{m^2 s^{-1}}$ and activation energy $Q_{Fe} = 183.4$ kJ/mol for the diffusion of iron [30].

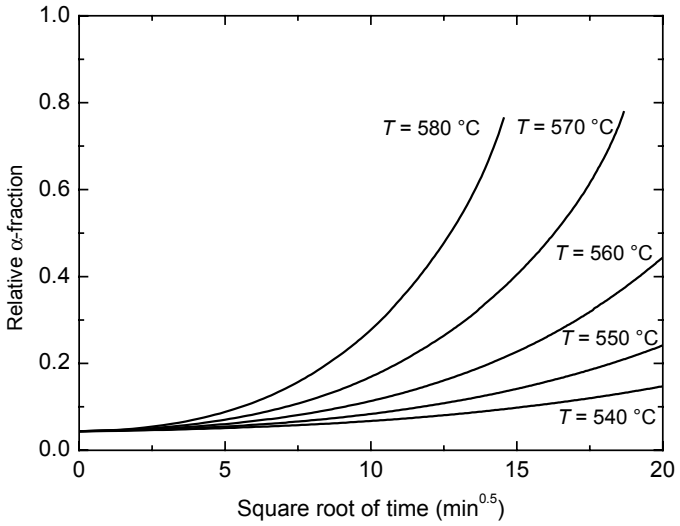

Figure 6.10 The relative α-fraction as a function of time for consecutive homogenisation temperatures, as computed by the Finite Elements Model. In the derivations, both the temperature dependence of the iron solubility concentration on the interface, and the diffusion coefficient of iron is taken into account, which parameters are presented in Table 6.2. The other model parameters are presented in Table 6.1.

Table 6.2 Input data for the computations at consecutive temperatures.

Physical quantity	T = 540°C	T = 570°C	T = 580°C
$c^s_{\beta Fe}$ (wt.%)	0.00850	0.0152	0.0183
$c^s_{\beta Si}$ (wt.%)	0.508	0.510	0.510
D_{Fe} ($\mu m^2 s^{-1}$)	0.00861	0.0226	0.0307
D_{Si} ($\mu m^2 s^{-1}$)	0.369	0.755	0.948

Figure 6.10 shows that the transformation kinetics are highly temperature dependent. An increase of e.g. 25 °C of the temperature can increase the transformed state considerably. This rapid increase is caused by two effects: both the solubility at the rim, and the diffusion coefficient increases with increasing temperature. To illustrate the effect of increasing temperature, without the influence of the solubility, calculations are performed with a fixed solubility of $c^s_{\beta Fe}$ = 0.0183 wt.%. The results are plotted in Figure 6.11. In this case, the temperature has significantly less effect on the transformation speed than for the results shown in Figure 6.10, as is to be expected.

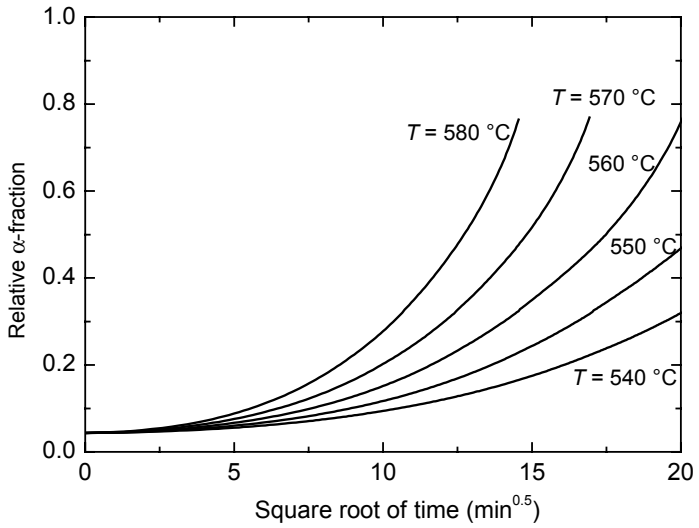

Figure 6.11 The relative α-fraction as a function of time for consecutive homogenisation temperatures, as computed by the Finite Elements Model. In the derivations, only the temperature dependence of the diffusion coefficient of iron is taken into account, which parameters are presented in Table 6.2. The other model parameters are presented in Table 6.1.

6.4.3 Comparison between the analytical approach and the FEM-approach

Figure 6.12 shows the evolution of the relative α-fraction, f_α, for the analytical, and FEM model, for both cylindrical and planar symmetry. For the analytical approach it is assumed that the α particle stays rounded during the transformation, and its radius is

defined by the position of the triple point F. Figure 6.12 shows that for the calculation of the relative α-fractions in the early stage, the analytical model is a reasonable alternative for the FEM calculation. For later stages (higher than $f_\alpha \approx 0.40$) the derivations becomes too large.

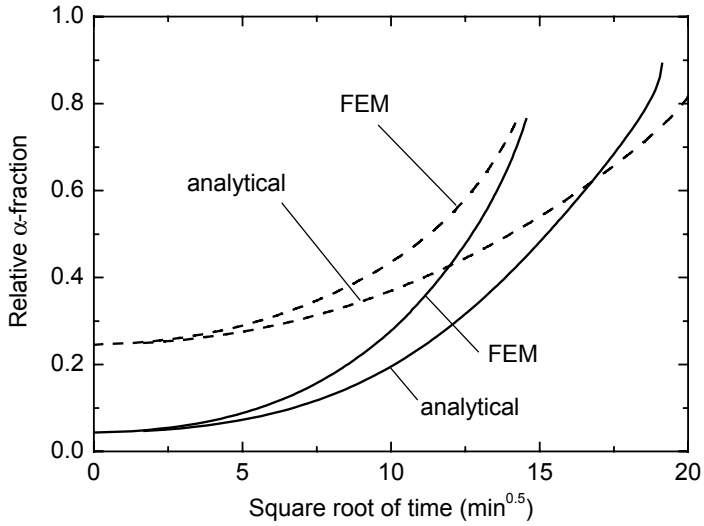

Figure 6.12 The evolution of the relative α-fraction by the use of the analytical approach and by the use of FEM, for cylindrical (as denoted by the straight lines) and planar (as denoted by the dashed lines) symmetry. The model parameters are presented in Table 6.1.

6.4.4 Model versus experiments

In the previous sections, we showed that the model showed realistic characteristics. In this section we want to perform a more quantitative comparison of the model calculations versus experiments. For the model calculations a cylindrical geometry is used with geometrical dimensions as experimentally determined. All other parameters are as presented in Table 6.1.

The mean thickness of the initial β-plate had a median thickness of 0.2 μm. This thickness of the β plate had a wide natural variation with a standard deviation of 0.15 μm. We did not find a statistical significant change in the mean thickness at later stages of homogenisation ($f_\alpha \approx 0.2$ and $f_\alpha \approx 0.5$). This supports the hypothesis that the thickness does not change during the homogenisation. Note that the thicknesses, found by SEM, are somewhat smaller than the thickness found by optical microscopy in 4) because SEM measurements also detect thinner β particles, which are not visible for optical microscopy. For the sake of simplicity, in this model we only consider the median thickness in calculations.

The nucleation distance of the α particles was determined. For the fully homogenised sample at 540°C the median distance was equal to 1.75 μm, and for a fully homogenised sample at 590°C this distance equals approximately 1.5 μm. There is a wide natural variation of the nucleation distances, with a standard deviation of 0.5 μm, but for the sake of simplicity, in this model we only take the nucleation density l=1.5 μm as a model parameter, and we neglect the temperature dependence. Note that although this median nucleation distances was corrected for the 3D situation, this values still fall in the measured distribution of the nucleation distances in the 2D plane.

The average DAS was approximately 20 μm. In Section 4.2.3., we found that the cell size does hardly has any influence on the numerical results providing it is larger than the β plate. Therefore, to reduce the computational effort, we used a numerical cell size which is smaller than the dendrite arm spacing, l_{cell} = 2.5 μm.

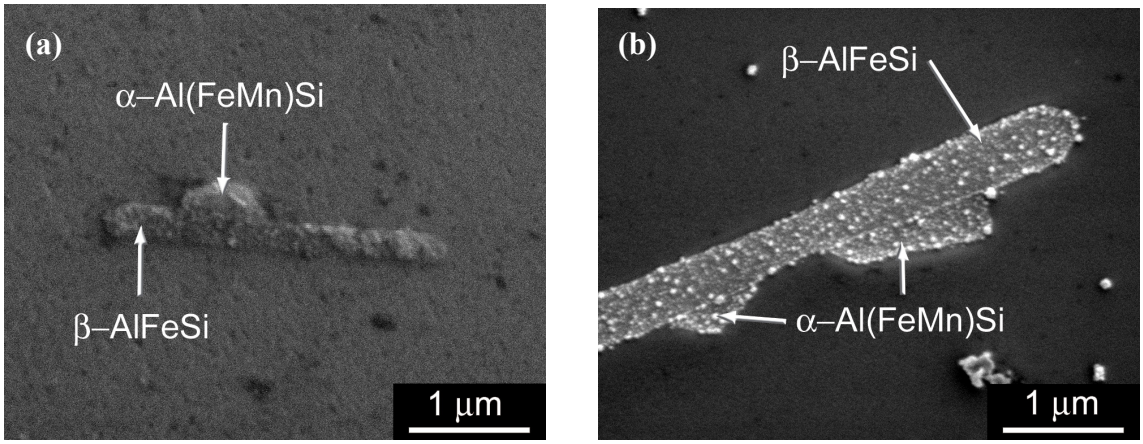

Figure 6.13 A micrograph of the Scanning Electron Microscope of an alloy homogenised at 540°C for 2 hours. (a) An α particle on a β particle. (b) Multiple α particles on a β particle.

The morphology assumed in the model calculations was also validated against some SEM micrographs. Figure 6.13a shows an SEM micrograph of an α particle which grows on top of a β plate. The morphology of this figure corresponds well to the numerical calculations. Figure 6.13b shows multiple α particles on one β plate. For the sake of simplicity we restrict ourselves in the model to one α particle. However, this figure shows interesting features, which are similar to those in the FE-Model. Firstly, this figure shows that the α particle does not remain spherical during growth. This asymmetrical growth is also observed in FEM calculations. Secondly, this figure shows clearly that the β/α interface remains in place during the transformation, and that the β/Al interface remains flat.

Figure 6.14 shows the relative α-fraction as a function of time computed by FEM and experiments. The time and temperature dependence of the relative α-fraction of the FEM model agrees well with the experiments. It should be pointed out that the model is capable to predict the transformation fraction up to approximately f_α=0.5.

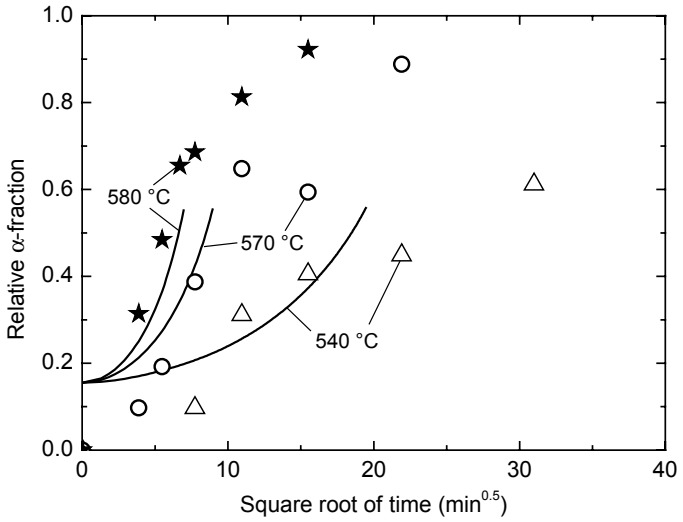

Figure 6.14 The relative α-fraction as a function of time derived by the Finite Element Model (presented by the straight lines) compared with the relative α-fractions, measured by experiments (presented by the separate points). The calculations and measurements are performed for three different temperatures.

6.4.5 Metallurgical implications

A proper homogenisation leads to a considerably increase in the extrudability and leads to less surface defects on the aluminium profiles. Therefore, preferably an extrusion ingot is homogenised to attain a high relative α fraction, e.g. preferable at least f_α=0.8 and preferably more than f_α=0.9 [1]. Although the presented transformation model is not applicable to homogenisation up to high relative α-fractions, yet still some important metallurgical implications can be already extrapolated from the numerical experiments.

Three aspects influences the homogenisation process in particular: the morphology of the intermetallics, the homogenisation temperature, and the alloy content. The influence of the alloy composition was not investigated in this study and will be discussed in Chapter 7.

A high temperature dependence of the transformation rate was found, both for numerical and experimental results. Industrial homogenisation temperatures of extrusion ingots are typically at approximately 585ºC [1]. The model showed that a decrease of the homogenisation temperature of e.g. 5ºC leads to a considerably increase

of the required homogenisation time of ~20%. Therefore, accurate temperature control is a very important aspect to achieve efficient homogenisation.

The morphology of the intermetallics has an important effect on the transformation speed. Section 6.4.2 indicates that thin β-particles will transform faster than thick β particles. Therefore it is important that the as-cast structure contains more thin distributed β particles, to achieve fast homogenisation times. Grain refiners, alloy composition and cooling speed mainly determines the coarseness of the β-AlFeSi particles, and therefore those parameters have to be optimised.

Also the effect of the DAS on the transformation speed is investigated. Experiments on the studied AA 6005A alloy indicate that the DAS ranges between 19 μm and 23 μm, within the DC-cast billet. The results as given in Section 6.4.2.C. indicate that this slight variation in DAS does not lead to a significant effect on the transformation speed.

6.5 Conclusions

A Finite Element Model has been presented which describes the initial stages of the β-AlFeSi to α-Al(FeMn)Si transformation. The model predicts strong effect of temperature and intermetallic morphologies on transformation kinetics. In spite of major simplifications in initial morphologies of the intermetallics the calculated FEM results agree over a large range of temperatures, with experimental data. A simple analytical model yielded qualitatively the same behaviour. We conclude from the good agreement of the FEM calculations and experiments that the β-to-α phase transformation kinetics is Fe diffusion controlled.

References

[1] N. C. Parson, J. D. Hankin, K. P. Hicklin: *Al-Mg-Si alloy with good extrusion properties*, US-pattent (2002) 6,440,359.

[2] S. Zajac, B. Hutchinson, A. Johansson and L. O. Gullman: *Microstructure control and extrudability of Al-Mg-Si alloys microalloyed with manganese.* Mat. Sci. Tech. **10** (1994) 323-333.

[3] A. Valles, R. P. L. Orsetti and R. Tosta: *Homogenising of 6063 alloy.* Proc. of the International Conference on Aluminium Alloys, Toyohashi, Japan (1998) 2123-2128.

[4] N. C. W. Kuijpers, J. Tirel, D. N. Hanlon, and S. van der Zwaag: *Quantification of the evolution of the 3D intermetallic structure in a 6005A Aluminium alloy during a homogenisation treatment*. Mat. Char. **48** (2002) 379-392.

[5] M. P. Clode and T. Sheppard: *Surface generation and origin of defects during extrusion of aluminium alloys.* Aluminium Technology '86, The Institute of Metals, 1 Carlton House Terrace, London SW1Y 5DB, UK (1986) 230-239.

[6] T. Minoda, H. Hayakawa and H. Yoshida: *A mechanism of pick-up formation on 6063 aluminium alloy extrusions.* Mater. Sci. Techn. **7** (2000) 13-17.

[7] S. Onurlu and A. Tekin: *Effect of heat-treatment on the insoluble intermetallic phases present in an AA-6063 alloy*. J. Mat. Sci. **29** (1994) 1652-1655.

[8] H. Tanihata, T. Sugawara, K. Matsuda and S. Ikeno: *Effect of casting and homogenizing treatment conditions on the formation of Al-Fe-Si intermetallic compounds in 6063 Al-Mg-Si alloys*. J. Mat. Sci. **34** (1999) 1205-1210.

[9] H. J. Lamb: *The effect of trace additions of manganese and prior heat-treatment on the structure of dilute Al-Mg-Si Alloy extrusion ingot.* Proc. of the Conf. on Phase Transformations, London, England (1979) Series 3, No. 1, 2, V4-V5.

[10] L. Lodgaard and N. Ryum: *Precipitation of dispersoids containing Mn and/or Cr in Al-Mg- Si alloys.* Mat. Sci. Eng. A **283** (2000) 144-152.

[11] N. C. W. Kuijpers, J. Tirel, D. N. Hanlon and S. van der Zwaag: *On the characterisation of the α-Al(FeMn)Si nuclei on β-AlFeSi intermetallics by Laser Scanning Confocal Microscopy.* J. Mater. Sci. Lett. **22** (2003) 1385-1397.

[12] J. Crank: *Free and moving boundary problems*. Clarendon Press, Oxford (1984).

[13] M. J. Whelan: *On the kinetics of precipitate dissolution.* Metal. Sci. J. **3** (1969) 95-97.

[14] H. B. Aaron and G. R. Kotler: *Second phase dissolution*. Metall. Trans. A **2** (1971) 393-408.

[15] U. H. Tundal and N. Ryum: *Dissolution of particles in binary-alloys.* Metall. Trans. A **23** (1992) 433-444.

[16] O. Reiso, J. Strid, and N. Ryum: *Melting of secondary-phase particles in Al-Mg-Si alloys.* Metall. Trans. A **24** (1993) 2629-2641.

[17] R. Hubert: ATB Metallurgie **34-35** (2002) 4-14.

[18] J. M. Vitek, S. A. Vitek and S. A. David. Metall. Trans. A **26** (1995) 2007-2025.

[19] F. J. Vermolen and C. Vuik. J: *A mathematical model for the dissolution of particles in multi-component alloys*. Comput. Appl. Math. **126 (**2000) 233-254.

[20] F. J. Vermolen, C. Vuik, and S. van der Zwaag: *A mathematical model for the dissolution of stoichiometric particles in multi-component alloys.* Mater. Sci. Eng. A **328** (2002) 14-25.

[21] R. Kobayashi: *Modeling and numerical simultations of dendritic crystal growth*. Physica D **63** (1993) 410-23.

[22] U. Grafe, B. Bottger, J. Tiaden, and S. G. Fries: *Coupling of multicomponent thermodynamic databases to a phase field model: Application to solidification and solid state transformations of superalloys.* Scripta Mater. **42** (2000) 1179-1186.

[23] E. Scheil: Z.Metallkd **34** (1942) 70-72.

[24] D. T. L. Alexander and A. L. Greer: *Solid-state intermetallic phase transformations in 3XXX aluminium alloys.* Acta Mater. **50** (2002) 2571-83.

[25] S. Fujikawa, K. I. Hirano and Y. Fukushima: *Diffusion of Silicon in Alumium*. Metall. Trans. A **9 (**1978) 1811-1815.

[26] D. A. Porter and K. E. Easterling: *Phase transformations in Metals and Alloys*, (Chapman & Hall, London, 1997).

[27] G. Segal, C. Vuik and F. J. Vermolen: *A conserving discretization for the free boundary in a two-dimensional Stefan problem.* J. Comp. Phys. **141** (1998) 1-21.

[28] L. F. Mondolfo: *Structure and Properties of Aluminium Alloys*. (Butter-worth, England, 1976).

[29] N. A. Belov, A. A. Aksenov and D. G. Eskin: *Iron in Aluminum Alloys, Impurity and Alloying Element,* (Taylor & Francis, Londen and New York, 2002) 132-136.

[30] D. L. Beke, I. Gödény, I. A. Szabó, G. Erdélyi and F. J. Kedves: *Diffusion Processes in Al Alloys.* Philos. Mag. A **5** (1987) 73-78.

Chapter 7

Alloy dependence of the β-to-α transformation kinetics

In this chapter the influence of the alloying elements, Mg, Fe, Mn and Si on the rate of the β-to-α transformation is studied. The model, as presented in Chapter 6, is used to model the influence of Mn and Si concentration on the β-to-α transformation rate. Thermodynamic databases (Thermo-Calc) are used to derive the interfacial concentrations of Fe at the interfaces of both the α and β intermetallics for various alloy compositions. The results of the model are validated with experimental data.

7.1 Introduction

Many process parameters such as homogenisation temperature and as-cast microstructure influence the transformation rate. The influence of those parameters is described in Chapter 6. In this chapter the influence of the Mn and Si concentration on the rate of the β-to-α transformation is studied.

Of all main alloying elements in 6xxx alloys, Mn seems to have the largest influence on the transformation rate. In the case of very low Mn levels, less than approximately 0.01 wt.%, an hexagonal α_h-AlFeSi phase is the stable phase [1]. Small additions of around 0.02 wt.% Mn stabilise the cubic α-Al(FeMn)Si phase and increase the β→α transformation speed [2]. A further increase of the Mn content increases the β to α transformation rate even more. The influence of Si is less significant than that of Mn and has been overlooked for a long time. However, recently it has been shown that an increase in Si content decreases the transformation rate [3].

Until now we did not find any model which explains the origin of the influence of Mn and Si on the transformation speed. Therefore, in this study we try to investigate this influence of Mn and Si concentration on the rate of the β to α transformation. To

this aim we use the same Finite Element Model as presented in Chapter 6. This FE-Model applies to the β-to-α transformation in the early state up to a transformed α-fraction of approximately 50%. We use a thermodynamic database TTAL [4] of the software package Thermo-Calc to derive equilibrium solubility products for various Mn and Si alloying levels. The equilibrium solubility products at the β-interfaces thus derived are used in a multi-component particle dissolution model, described by Vermolen *et al* [5], to obtain the interfacial concentrations of the alloying elements. Then, the interfacial concentrations are used as boundary conditions for the Finite Element calculations. In these FEM calculations geometrical parameters are used which are obtained from an experimental characterisation of the alloys. Subsequently, the results of the Finite Element Model results are compared with experiments.

7.2 Al-Fe-Si-Mn phase diagrams

Figure 7.1a visualises the aluminium corner of the Al-Fe-Si phase diagram [6-11] which is a good approximation of the phase diagram of a Mn free AA 6xxx alloy since the effect of Mg on the phase diagram is small [11]. As Mn-free AA 6xxx alloys contain small amounts of Fe and Si, the phase diagram indicates that besides matrix Al only the hexagonal α_h-Al_8FeSi or the β-AlFeSi phases are stable. The other phases in Figure 7.1a, such as Al_3Fe, $AlFeSi_2$ and Al_3FeSi are only stable if the alloy content deviates from the 6xxx family of alloys, e.g. for high Fe and Si contents. Note that in this Al-Fe-Si phase diagram the cubic α phase (α_c) is not present, since a minimum Mn content is required to stabilise this phase.

Figure 7.1b shows an enlargement of the calculated aluminium corner of the Al-Fe-Si phase diagram at a temperature of 540°C, showing a quantitative picture of the aluminium-rich part. This is obtained by use of the Thermo-Calc database. The graph shows that the maximum solubility of Fe in Al is considerably lower (~0.015 wt.%) than the maximum solubility of Si (~1 wt.%). Figure 7.1b shows that high, intermediate, and low Fe/Si alloy-content-ratios lead to stabilisation of the Al_3Fe, α_h and β phases respectively. The effect of Fe/Si ratio and the Si content on the stable phases has been confirmed experimentally [2, 3, 11, 12].

The alloy composition of 6xxx alloys is designed such that the stable intermetallic phase is the α phase. By extrapolating Figure 7.1b it can be shown that for a lowly Si alloyed AA 6xxx system (e.g. 0.6 wt.%) a low Fe alloy content (~0.20 wt.%) is required, whilst for a highly Si alloyed 6xxx system (e.g. 1.5 wt.%) a high Fe content is required (~0.5 wt.%).

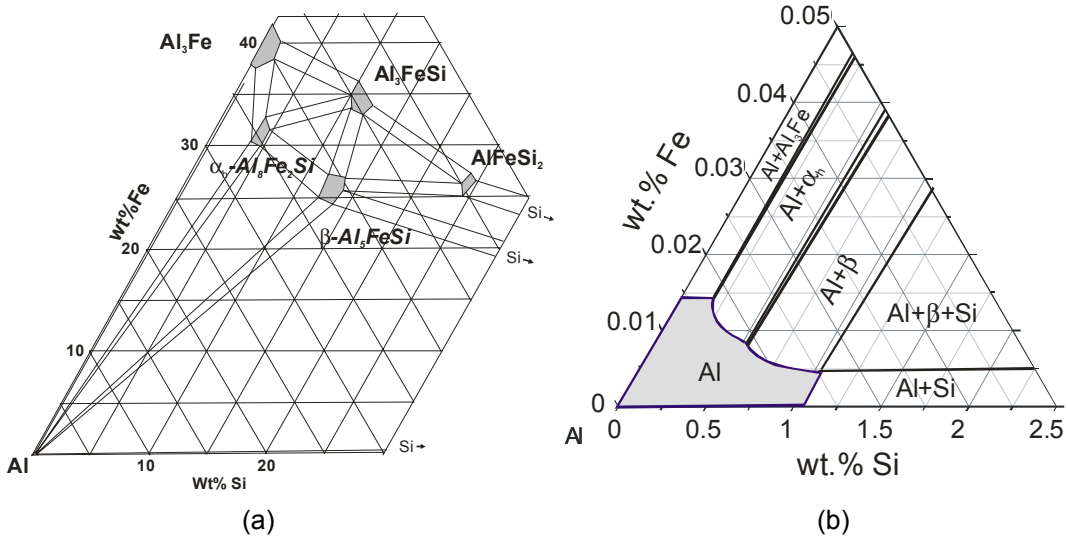

Figure 7.1 (a) The Al-corner of the Al-Fe-Si phase diagram [1]. (b) Enlargement of the Al-corner of the calculated Al-Fe-Si phase diagram, as derived by Thermo-Calc for a temperature of 540°C. Note that, in this graph, the Fe-scale is enlarged.

In the previous phase diagram only the hexagonal α phase (α_h) was present since Mn was absent. It is also interesting to study the influence of Mn on the stabilisation of the cubic α (α_c) intermetallics. This influence is depicted in the phase diagram of Figure **7.2**a, which is constructed using the results of [6,13] and the Thermo-Calc package. The figure shows that the presence of some manganese stabilises the α_c phase. The Mn content of the stabilised α_c phase is highly dependent on the alloy composition, as indicated by the tie-lines. This was also found by Tibbals *et al* [13]. Some authors [6,13] found some slight change in stoichiometry of the α phase as the Fe/Mn ratio changes. However, since these changes are only small we neglect them in the presented phase diagram of Figure **7.2**a, and we use the $Al_{12}(Fe_xMn_{1-x})_3Si$ stoichiometry in our calculations.

Figure **7.2**b shows an enlargement of the aluminium corner of the phase diagram of Figure **7.2**a. In this graph the Al-phase is visualised, where the β-phase is not taken into account. The Figure shows again that the solubility of Fe is very small (~0.01) compared to the solubility of Mn (~0.15 wt.% Mn). This graph also shows that the equilibrium Fe and Mn matrix concentration of the aluminium is highly dependent on the Fe to Mn alloy ratio, as indicated by the dotted tie-lines: For a high Fe-to-Mn ratio the hexagonal α phase (α_h) is stabilised, whilst for lower Fe to Mn ratios the cubic α phase (α_c) is stabilised. Similar results are obtained for other Si concentrations within the AA 6xxx compositional window.

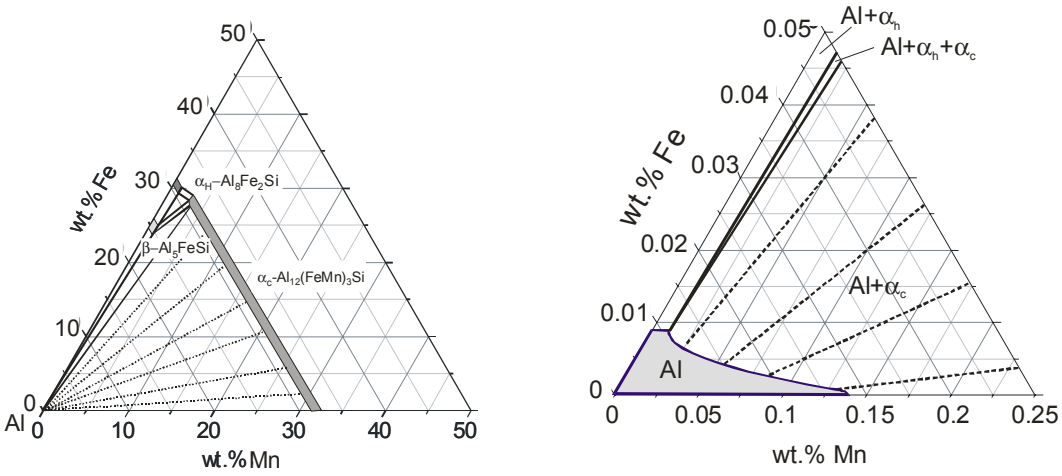

Figure 7.2 (a) Projections of the Al-Fe-Mn-Si phase diagram onto the Al-Mn-Fe plane. The non-relevant intermetallic phases for 6xxx series are left away. (b) Enlargement of the Al-corner of the Al-Fe-Mn-Si phase diagram, as derived by Thermo-Calc for a fixed Si matrix concentration of 0.5 wt.% at 540°C. Note that, in this graph, the Fe-scale is enlarged.

7.3 The model

7.3.1 Introduction

Since the Finite Element Model of the β-to-α transformation is already presented in detail in the previous chapter, we only give a brief introduction to this finite element model. After this, a thermodynamic study is presented, showing the influence of Mn and Si contents in the alloy on the chemical potential of Fe of the interfaces. These chemical potentials are an input in the FE-Model and influence the transformation speed.

7.3.2 General description of Finite Element Model.

Figure 7.3 shows a schematic representation of the particle and matrix as modelled in the FE-Model. For the model cylindrical co-ordinates are used where the line AH is the axis of symmetry. This geometry presents a piece of the original β-plate with one α nucleus on top of it. The FE-Model describes the growth of the α-particle towards the dissolving rim S_β of the β-plate. During the transformation, the thickness of the β plate remains constant. The α particle grows along the entire α/Al interface, indicated by S_α. The transformation is assumed to be diffusion controlled, and its driving force is given by the difference in chemical potential. Fe and Si diffuse from the β rim through the aluminium matrix towards the α particle. Since the diffusion speed of Fe is a few orders slower than that of Si, only the diffusional fluxes of Fe are dealt with in the model. The

velocities of the moving boundaries S_α and S_β are derived by the use of the Stefan condition [14], considering the equilibrium interface concentration, and the diffusion flux at the boundary. All FEM calculations are performed using the software package SEPRAN, which has been developed at the Department of Applied Mathematics at the Delft University of Technology, The Netherlands.

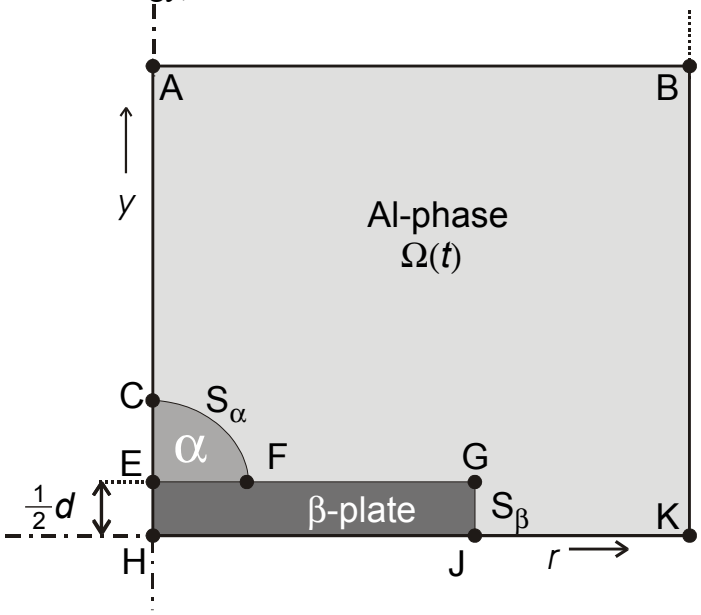

Figure 7.3 The geometry of the domain of compution of an α particle on a β plate in an Al-phase. The parameters are explained in the text.

Table 7.1 Basic physical parameters which are used for the finite element model calculations.

Parameter	Symbol	Value
Diffusion pre-factor [15]	D_0	$5.3 \cdot 10^{-3}$ m^{2}s^{-1}
Activation energy of diffusion [15]	Q	183.4 kJ/mol
Fe concentration in α particle [1]	c_α^p	39.9 wt.%
Fe concentration in β particle [1]	c_β^p	33.9. wt.%
Initial radius of α particle	r_α^{init}	0.25 μm
Thickness of β-plate	D	0.2 μm
Equivalent Diameter of initial β-plate	l	1.5 μm
Cell size of aluminium matrix	l_{cell}	2.5 μm
Temperature	T	853 K (580°C)

Table 7.1 presents the model parameters used for the FEM. The Fe particle concentrations were derived by use of the densities and the stoichiometry of the α and β phases. The geometrical parameters, such as initial radius of the α particle, initial

thickness, and initial diameter of the β plate were obtained experimentally at 580°C as described in section 7.4. In the FEM calculations, it is assumed that the geometrical starting parameters are not affected by the variation of the matrix content in Si and Mn level and by temperature.

Since the FEM cell is smaller than the DAS spacing we assume that the initial Si and Fe concentration is equally distributed over this FEM cell. The cell size is only a parameter which is of interest from a numerical point of view, and not of major importance in the quantitative results.

We assume that the matrix is initially in equilibrium with the β particle. In the FE-Model we do not take Mn diffusion into account, and we assume that the Mn matrix composition remains constant during time.

7.3.3 Thermodynamics

As demonstrated in Chapter 6 we argue that the main driving force of the transformation is the difference in chemical potential ($\Delta\mu_{\mathrm{Fe}}$) of solute iron on the interfaces (S_α and S_β) of the phases in the aluminium alloy:

$$\Delta\mu_{\mathrm{Fe}} = \mu_\beta^s - \mu_\alpha^s. \tag{7.1}$$

This difference in chemical potential of the iron solute levels in the Al-phase close to the α (μ_α^s) and the β interface (μ_β^s), result in a diffusional flux of iron atoms towards the α phase. It is assumed that the interfacial reactions are fast enough to maintain local thermodynamic equilibrium concentrations at the α/Al and β/Al interface. The chemical potentials of Fe at the two interfaces depend on the solute levels of other elements, such as Si and Mn. Since the Finite Element Model is based on Fick's diffusion for the Fe-concentration in the Al-phase, we use the differences in the solute concentration between the α and β interfaces instead. For the FEM calculations, the solubility product of the β-Al_5FeSi plate, as derived by Thermo-Calc, is expressed in an Arrhenius relation (see also Appendix 2):

$$c_{Fe}^s c_{Si}^s = A_\beta \exp\left(\frac{-Q_\beta}{RT}\right) \tag{7.2}$$

The Thermo-Calc calculations lead to A_β=10 and Q_β=115 kJ/mol. Since α particles do not have a uniquely defined stoichiometry, we did not find a solubility product for the solubility at the α/Al interface. Therefore, for the FEM calculations we use the α/Al interface concentration that was directly found by ThermoCalc.

A. Dependence of the interfacial concentration of Fe on the Mn content

It was found by experiment that the Mn alloy content has a large effect on the transformation speed [3,2,16,17], and therefore it is to be expected that the Mn content influences the driving force $\Delta\mu_{Fe}$ of the transformation considerably. $\Delta\mu_{Fe}$ is approximately proportional to the logarithm of the concentration difference. Figure 7.4 shows the influence of the Mn solute level in the solubility of Fe on the intermetallic interfaces at industrial temperatures of homogenisation (540 ºC and 580 ºC). As an example the concentration difference (Δc_{fe}) between the α/Al and β/Al interface are indicated for a Mn matrix concentration of 0.05 wt.% at 540 °C.

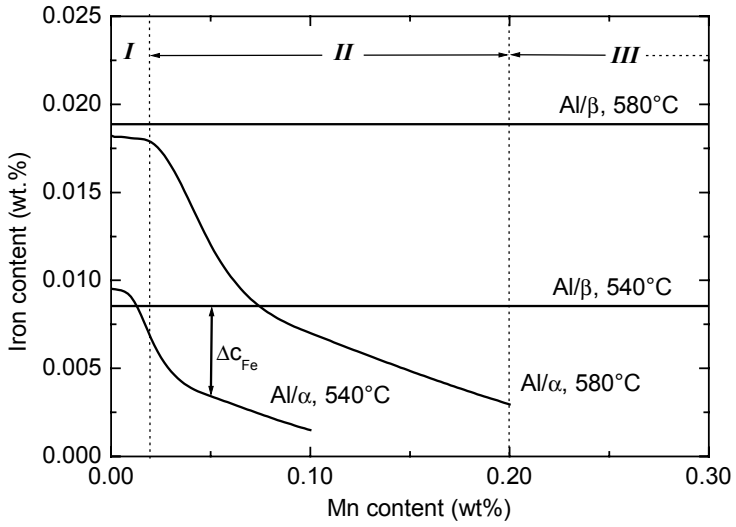

Figure. 7.4. Plots of the interfacial matrix concentrations (c_{Fe}) as a function of the Mn matrix content. The results were obtained by Thermo-Calc. Plots are drawn for both Al/α and Al/β interfaces, at homogenisation temperatures of 540°C and 580°C. For the presented calculations a fixed matrix concentration of 0.5 wt.% Si is used.

Figure 7.4 is divided into three domains indicated by region *I*, *II* and *III*. In domain *I*, representing Mn concentrations between 0 wt.% and 0.02 wt.%, the driving force Δc_{Fe} is negative or very small, and therefore the β-AlFeSi particles will not, or only slowly, transform by diffusion controlled transformation to the α-Al(FeMn)Si particles. In some parts of this domain the solubility of the α_h is lower than α cubic, and in this case, the α_h is stabilised. In domain *II*, representing Mn alloy contents between 0.02 and 0.2, an addition of Mn increases the transformation speed considerably. In region *III*, with Mn concentration higher than 0.2 wt.%, the transformation speed remains high and does not significantly depend on the Mn content anymore. These qualitiative predictions are in agreement with experimental data by Zajac *et al.* [2].

B. Dependence of the interfacial concentration of Fe on the Si content

It is reported in literature [3,2,12] that the transformation speed decreases as the Si level increases. Therefore it is expected that also the Δc_{Fe} decreases with increasing Si concentration. Figure 7.5 shows the influence of the Si matrix concentration on the Fe matrix concentrations at the β/Al and α/Al interfaces for $T = 540$°C. In the calculation results a fixed matrix concentration of 0.02 wt.% Mn was used. The figure shows that the influence of the Silicon matrix concentration on the Fe solubility ranges over a wider range (0-1 wt%) than that of Mn (0-0.2 wt%). As expected, the driving force Δc_{Fe} decreases with the Si concentration in the matrix. This effect is indicated in the figure for two values of Δc_{Fe} at Si levels of 0.1 wt.% and 0.5 wt.% Si, which shows a significant drop in Δc_{Fe} for the latter case. The figure also shows that the drop of the Δc_{Fe} is larger for alloys with lower Mn contents. Therefore, it is concluded that a combination of low Mn concentration and high Si concentration leads to a very low driving force and transformation rate. For the zero Mn level, this effect is such that negative Δc_{Fe} values are obtained. In this case no phase transition of β to α will occur and annealing would only result in a growth of the β plates. Such behaviour has indeed been reported [18].

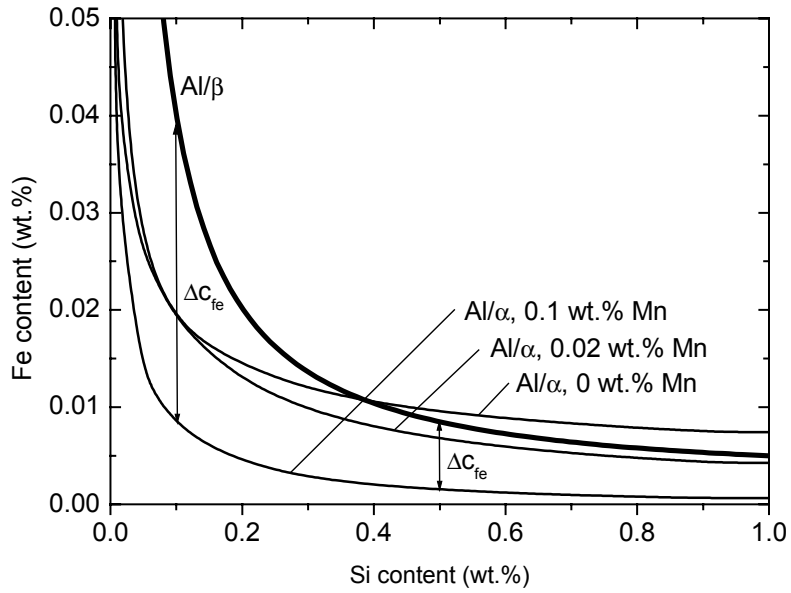

Figure 7.5 The interfacial matrix concentrations (c_{Fe}) as a function of the Si matrix content. The data was obtained by Thermo-Calc. Plots are drawn for both Al/α and Al/β interfaces, for various Mn matrix compositions at a homogenisation temperature of 540°C.

Now we investigate the combined effect of the Mn and Si matrix concentrations on the driving forces in more detail. Figure 7.6 shows the iso-Δc_{Fe} contours for a window of matrix concentrations of 0 to 0.2 wt.% Mn and 0.2 to 1.0 wt.% Si levels, at a temperature of $T = 580°C$. Each contour represents the Mn and Si concentrations for which the Δc_{Fe} is the same, and therefore are expected to have the same transformation rate.

In the figure three different regions of matrix compositions, labelled by A, B and C, are indicated. The alloys in region A have relatively high Mn and low Si concentrations. At those compositions the Δc_{Fe} is relatively large (>0.020 wt%), hence the transformation is fast. The alloys in region B have low Mn and high Si concentrations. At those compositions the Δc_{Fe} is relative small (<0.005 wt.%), hence the transformation is relatively slow. The alloys in region C have a very low Mn concentration and high Si concentrations. At those compositions the Δc_{Fe} is negative, and therefore the β phase is stable and a β-to-α transformation does not take place.

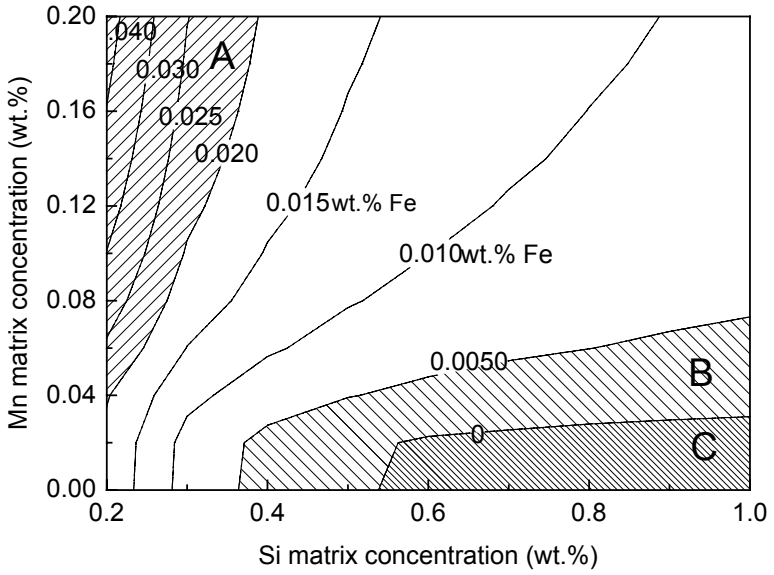

Figure 7.6 Iso-Δc_{Fe} contours for a window of Mn and Si compositions.

7.3.4 Kinetics

In this section we present some calculated transformation rates as a function of time for several values of the Mn and Si content. The results were obtained from the Finite Element Model.

A. Influence of the Mn content on transformation

First, the influence of the Mn matrix content on the β-to-α transformation rate is investigated. For this example we took a fixed Si-matrix concentration of 0.3 wt.%. Figure 7.7 shows the transformed fraction as a function of time of various alloy Mn levels. Mn additions between 0 and 0.02 wt.% show a small effect on the transformation rate. However, Mn additions between 0.02 and 0.20 wt.% give a considerably larger effect on the transformation rate. It was found that Mn additions larger than 0.20 wt.% have almost no extra effect on the transformation rate anymore, since in this case the maximum Fe concentration difference between the α/Al and β/Al interface is achieved.

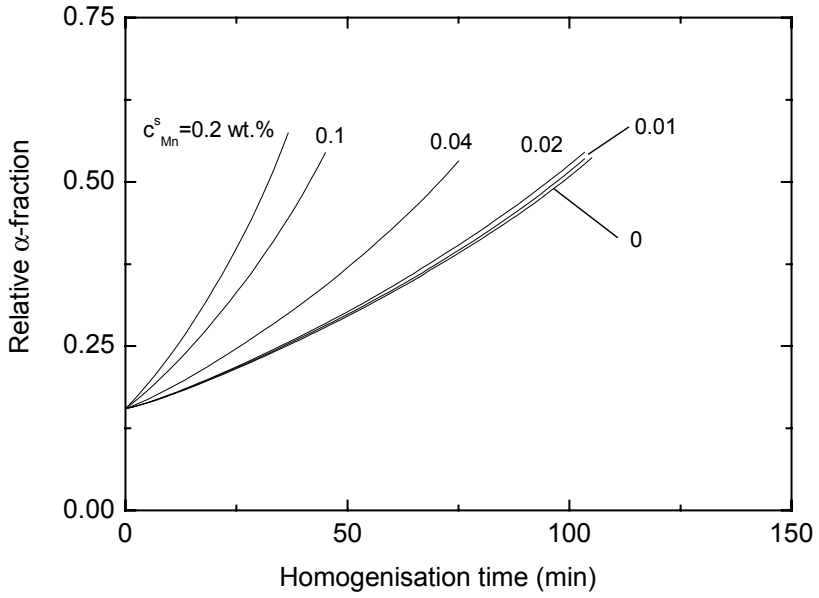

Figure. 7.7 Transformed fraction as a function of time at various Mn levels.

B. Influence of Si content on transformation

Figure 7.8 shows the transformed fraction as a function of time for various Si matrix concentrations. The figure shows that a variation of the Si concentration between 0.1 and 1 wt.% has a large influence on the transformation rate. Figure 7.8a shows the influence of Si in the case of a large Mn content of 0.2 wt.%. Figure 7.8b shows the influence of Si in the case of a small Mn content of 0.02 wt.%. The figure indicates that, when decreasing the Mn content, the influence of the Si content on the transformation rate increases considerably. The cases of a Si matrix concentration of 0.6, 0.8 and 1.0 wt.% in Figure 7.8b are hypothetical, since in this case Δc_{Fe} is negative, and the finite element model derives a dissolution mechanism of the α particles, and the β particles will be stabilised.

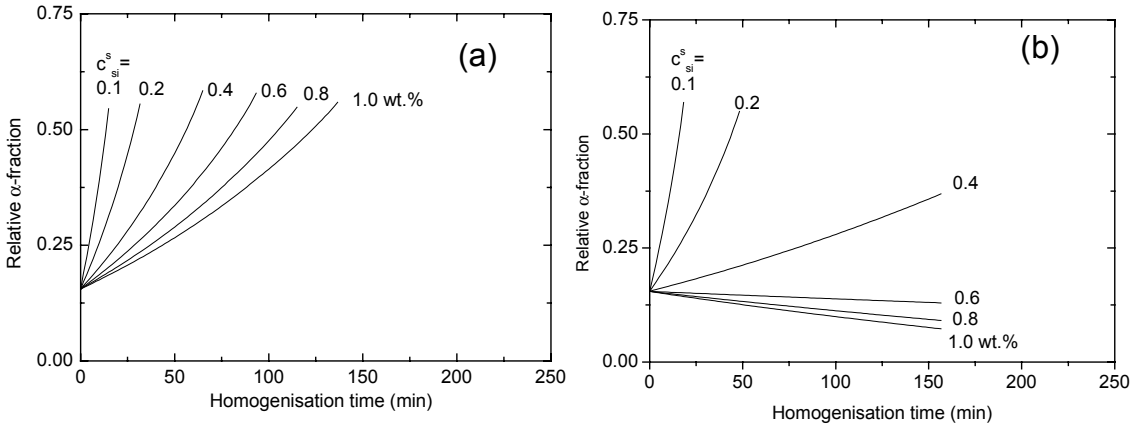

Figure 7.8 Transformed fraction as a function of time at various Si levels. (a) With a fixed Mn matrix concentration of 0.10 wt.%. (b) With a fixed Mn matrix concentration of 0.02 wt.%.

C. Influence of both Mn and Si content on transformation rate.

We investigate the combined effect of the Mn and Si matrix concentrations on the transformation time. Figure 7.9 shows the iso-time contours for various Mn and Si alloy contents. Each contour represents the Mn and Si content for which the transformation time up to a fraction of f_α=0.5 wt.% is the same. The figure indicates that the transformation time could be short (30 minutes), for alloys with a low Si and high Mn content. On the other hand, long homogenisation times, longer than 4 hours, are required for alloys with a high Si and low Mn content. In the extreme case, of a high Si content, and a Mn content lower than 0.02 wt.%, there is no transformation anymore. The dashed area in the diagram indicates the alloy compositions in which there is no transformation.

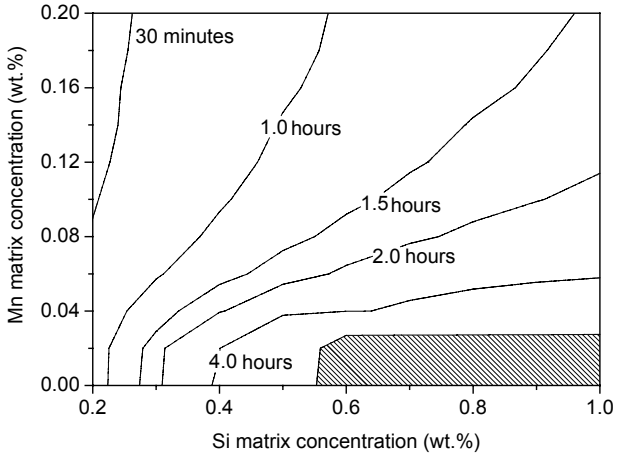

Figure 7.9 Iso-transformation-time contours for a window of Mn and Si compostions.

7.4 Experimental

For our experiments we prepared two sets of samples. The first set is designed to study the effect of the Mn contents on the β-to-α transformation rate. The second set is designed to study the combined effect of the Mn and Si content on the temperature dependence of the β-to-α transformation.

For the first set of samples we used three different Al-Mg-Si alloys, all with a concentration of ~0.4 wt.% Mg, ~0.6 wt.% Si and ~0.2 wt.% Fe similar to those in an AA 6063 alloy. The Mn concentration was varied between 0.01 wt.% and 0.1 wt.%. Table 7.1 presents the exact compositions of the alloys, labelled by H1, H2 and H3, with a low, medium and high Mn content respectively. Samples of each alloy were homogenised at a fixed temperature of 580°C for times ranging between 10 minutes and 2 days.

Table 7.2 Alloy compostions of first set of samples, used for the investigations of the effect of the Mn content on the β-to-α transformation rate (wt.%).

Alloy	Mn	Mg	Si	Ti	Cr	Fe	Cu	Zn
H1	0.011	0.431	0.605	0.016	0.001	0.200	0.009	0.009
H2	0.022	0.431	0.637	0.011	0.003	0.234	0.004	0.010
H3	0.044	0.436	0.627	0.015	0.008	0.215	0.010	0.011

For the second set of alloys we used two types, a AA 6063 and an AA 6005A alloy, labeled as A1 and A2 respectively. Both alloys differ mainly in Si and Mn content. Table 7.3 presents the exact compositions of the alloys, as determined by chemical analysis. Alloy A1 has a low Si and Mn content, whereas alloy A2 has a high Si and Mn content. Series of samples of each alloy were homogenised at temperatures ranging from 540°C to 590°C for times between 15 minutes and 4 days.

Table 7.3 Alloy contents of second set of samples, used for the investigation of temperature-dependence of the β-to-α transformation.

Alloy	Mg	Si	Mn	Fe	Other
A1	0.43	0.58	0.02	0.18	≤0.03
A2	0.70	0.83	0.18	0.27	≤0.02

Both sets of samples were taken at locations between 10 mm and 30 mm from the rim of the original DC-cast billets, which had a diameter of 203 mm (H1, H2, H3, A1) or 254 mm (A2). The microstructures of these samples, represent the typical

microstructure of the billet. For the homogenisation of the samples we used an air circulation oven, for which the maximum temperature deviation over all locations in the oven was 3°C. The samples were ground and polished down to ¼ μm silica, where the polishing plane is taken parallel to the surface of the billet. The relative α-fraction was determined using automatic SEM measurements in combination with Electron Dispersive X-ray Spectography (EDX). The α and β particles were classified on the basis of the (Fe+Mn)/Si ratio's. The method is described in more detail in Chapter 2.

To verify whether the initial microstructures of all alloys were comparable, we determined the Dendrite Arm Spacing (DAS) and the thickness of the β plates in each alloys. The DAS of each cast alloy was determined by averaging 40 separate spacings from 5 optical micrographs on the same polished sample. Comparable DAS-values ranging from 18 to 20 μm with standard deviations of 4 μm were obtained. The thickness of the β plates was obtained by SEM observations with a JEOL 5600F at a voltage of 2 keV. For each alloy we investigate samples which were homogenised for 30 minutes at 580 °C. For this homogenisation time, the Mg_2Si particles had dissolved while the β-intermetallics dimensions were practically not affected. Each sample was prepared and polished as described before and subsequently electro-etched at 20 V during 30 seconds in a mixture of 78 perchloric acid, 90 ml water, 730 ml ethanol and 100 ml butylglycol. The apparent thickness d' as observable in 2D cross sectional images was determined by averaging the thickness of fifty β-plates, using the area's of the particles as weight factors of the determination of the mean. The true thickness d was obtained using $d = \pi/4 * d'$. The corrected thickness varied between 0.2 and 0.3 μm with a large natural standard deviation of 0.05 μm. The thickness distributions all had a median at around 0.2 μm. The small differences in the DAS value and β plates thickness between the various alloys confirmed that the initial microstructures of all alloys under investigation are comparable.

The nucleation distance is an important input parameter in the FE-Model and therefore this was determined for each alloy separately. The nucleation distance between individual α particles was measured on fully homogenised samples (2 days at 580 °C). After this homogenisation, the intermetallics are present as strings of α particles. On average, one string contained approximately four or five α particles. The α particles situated on one string were formerly nucleated on the faces of one β plates. Therefore, the distances between those transformed α particles represents the initially nucleation distance on the β plates. 20 optical micrographs were made on each polished sample. The nucleation distance was obtained by $l' = L/(n-1)$, where L represents the distance between the outside particles, and n is the number of particles which are present in a sequence. The average nucleation distance in the polished plane was

determined by averaging the results of 20 strings of α-particles. Subsequently we made a correction for the translation to the average nucleation distance in 3D morphology by *l=l'/2*. This method was described in more detail in Chapter 5.

7.5 Results and discussion

7.5.1. Influence of the Mn level on transformation

Figure 7.10 presents the measured fraction transformed as a function of homogenisation time for various alloys with Mn concentrations ranging between c_{Mn}=~0.01 and 0.2 wt.% on material that was homogenised at 580°C. As expected, the rate of transformation increases significantly as the Mn alloy concentration increases. The transformation rate shifts by almost two decades when going from the low Mn alloy (c_{Mn}=0.01) to the Mn rich alloy (c_{Mn}=0.2). From the figure, the experimental transformation rates at f_α=0.25 and f_α=0.50 can be determined for comparison with the rates predicted by use of the model. The experimental rate of the transformation is determined by the derivative in time of the f_α fraction (df_α/dt).

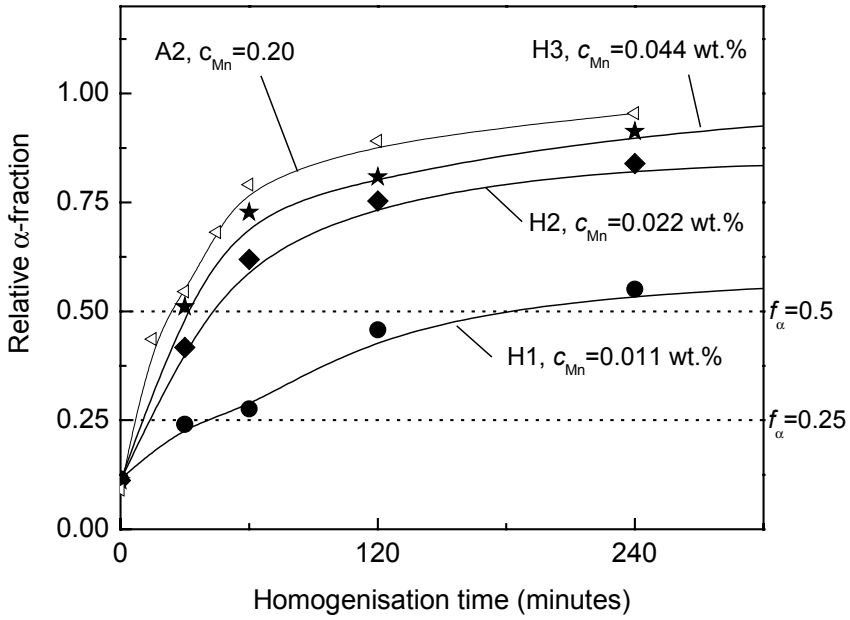

Figure 7.10 Measured transformation rate at 580°C for alloys containing various Mn levels. The labels of the alloys and the Mn contents of the various alloys are indicated in the figure.

Considering the model, it is expected that, when the temperature is constant, the rate of the transformation is almost linear with the difference of the Fe concentration at the α and β interface (Δc). For a general representation of the results, we define the "kinetic

force" by $D{\cdot}\Delta c$. In this section the temperature is constant and hence the diffusion coefficient does not change. To test whether this linear behaviour also holds for our experimental rates, we plot the experimental and modelled rates as a function of $D{\cdot}\Delta c$ for f_α=0.25 and f_α=0.5 in Figure 7.11a and b respectively.

In calculating the kinetic force, it was assumed that part of the Si concentration (Δc_{Si}) is bound to precipitates and intermetallics, and giving reduction of the Si matrix concentration by: $c_{Si\ matrix} = c_{Si\ \ alloy} - \Delta c_{Si}$. Therefore Figure 7.11 shows for four experimental alloys the rate of transformation as a function of the calculated kinetic force for various Δc_{Si} values, ranging between 0.2 and 0.4 wt.%. The solid lines give the predicted rate as a function of kinetic force, showing, as expected, a linear behviour.

Figure 7.11b shows that for the experimental rate at f_α=0.5 the experimental transformation rate at a Si binding of Δc_{Si}=0.35 are comparable with the model prediction. The rate at low Mn level of 0.011 w.% deviates from this trend. One explanation of anomalous slow speed for low Mn alloys is that in stead of cubic α particles to be formed, now hexagonal α particles are stable and hence formed, which might have a different growth mechanism [2]. Another explanation is that the low Mn content leads to a less cubic α nuclei, leading to a slower transformation.

Figure 7.11a shows that the experimental rate at f_α=0.25 deviates significantly from the model. Possibly this is due to the uncertainty in the initial α particle size and incubation time.

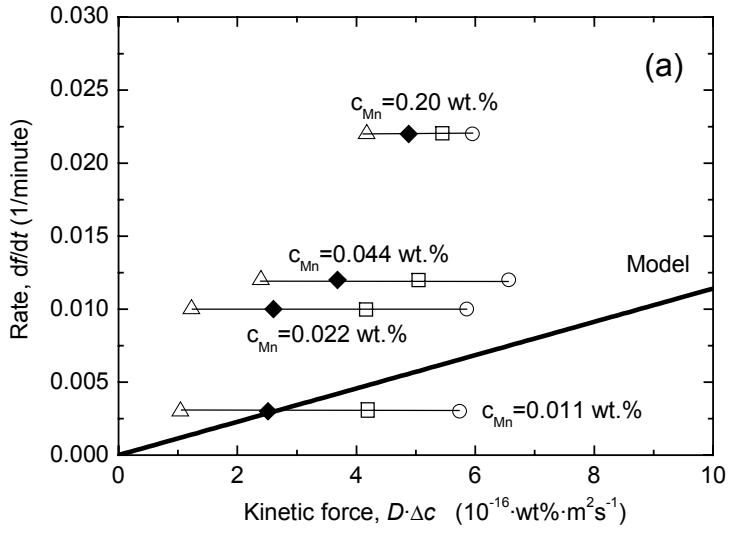

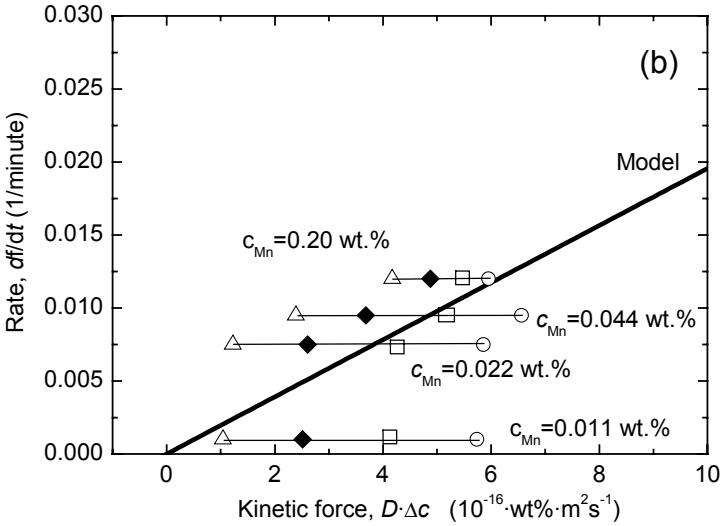

Figure 7.11 Measured transformation rate versus determined kinetic force, $D\cdot\Delta c$, compared with model. (a) for f_α=0.25. (b) for f_α=0.5. Δ, ♦, , O: Measured rates at various kinetic forces as derived for the bounded silicon concentrations Δc_{Si} = 0.2, 0.3, 0.35 and 0.4 wt.%. —— :Model.

7.5.2 Influence of alloy contents on T-dependence of transformation

Figure 7.12 shows the temperature-dependence of an AA 6063 alloy (alloy A1), which has a low Mn alloy content of 0.02 wt.%. The Johnson-Mehl-Avrami equation [19], f_α=1-exp(1-kt^n), is used to fit the experimental data points. It was found that for all temperatures the parameter n was approximately 0.5, which supports the hypothesis of a diffusion controlled transformation [19]. Figure 7.12 makes it clear that the transformation in the AA 6063 alloy has a high temperature dependence. The figure shows that for a homogenisation temperature of 540°C there is hardly any transformation, even after homogenisation times of 5760 minutes (4 days), whilst for a homogenisation temperature of 580 °C, the material is already homogenised to a fraction of f_α=0.8 after 360 minutes (6 hours). The temperature dependence of the transformation in an AA 6005 alloy (Alloy A2) (See Chapter 6), which had a higher Mn and Si content, was found to be less than that for the AA 6063 alloy.

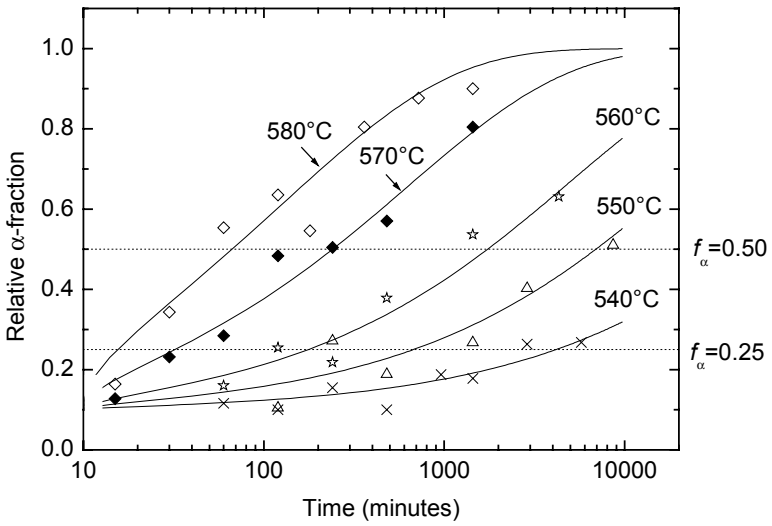

Figure 7.12 The relative α-fraction of a 6063 alloy with a low Mn and Si content as a function of time for several temperatures: ◊: 580°C, ♦: 570°C, *:560°C, Δ: 550°C, ×: 540°C. The trends of the measured temperature are indicated in the graph by the solid lines.

In Figure 7.13, the experimental transformation rates at f_α=0.25 and f_α=0.50 are compared with the rates predicted by our model. Figure 7.13a and b show the results for an alloy which have respectively a low (0.02 wt.%) and a high (0.18 wt%) Mn content. For the model we used a bounded Si concentration of Δc_{Si}=0.35. Again, the experimental rate was determined by the derivative with respect to time of the f_α fraction (df_α/dt). Since the transformation rate decreases as time proceeds in our experiments, the experimental transformation rate at f_α=0.25 is higher than at f_α=0.5. From the model we observe the contrary; Since the modelled transformation rate increases during time, the modelled rate at f_α=0.25 is lower than at f_α=0.5. Probably this is due to the model assumption that the interfacial concentrations are fixed at all times during the tranformation process. Multi-component models show that the interfacial concentration change as time proceeds (See Chapter 6). The assumption of fixed interfacial concentrations is used here since multi-component effects have not yet been implemented in the Finite Element model. This will serve as an accurate approximation for the early stages of the transformation.

From the model, it is expected that the transformation rate at a certain transformed fraction is linear with the diffusion coefficient and the Fe concentration between the β/Al and α/Al interface. Therefore we again define the "kinetic force" as $D \cdot \Delta c$. Note that both the diffusion coefficient D and Δc_{Fe} changes due to temperature change. From Figure 7.13a and b it is clear that for the model calculation, the rate is linear indeed with

the kinetic force. For the model calculations at all temperatures we used the geometrical parameters as experimentally determined at 580°C.

Figure 7.13a shows that the temperature dependence of the experiments with a low Mn alloy composition is different from the model predictions. The model calculations in Figure 7.13a show that the rate depends on the kinetic force according to a power law, but the slope of the measurements differs significantly from the slope obtained by the model predictions. In contrast, Figure 7.13b shows that the temperature dependence of the experiments for high Mn concentrations (alloy A2) agrees better with the model predictions. The experimental rates have an almost linear relation with the kinetic force and the experimental fractions at f_α=0.25 show an almost perfect match with the model (See Figure 7.13b).

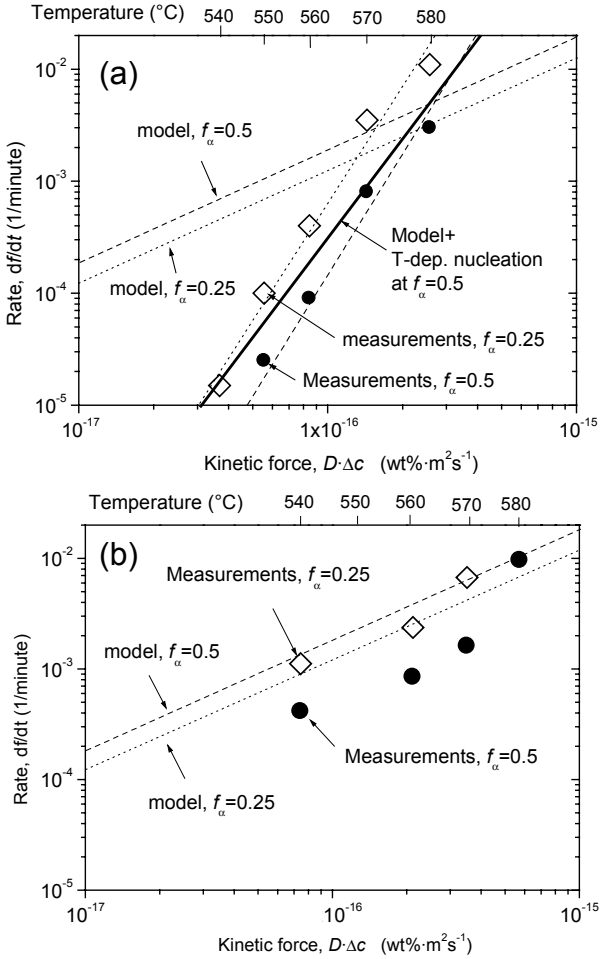

Figure 7.13 Measured and modelled transformation rates versus the theoretical kinetic force, $D^*\Delta c$. (a) For an alloy with a low Mn content (alloy A1). (b) For an alloy with a high Mn content (alloy A2). The corresponding temperatures are indicated on the top-axis. The dotted and dashed lines indicate the trends at f_α=0.25 and at f_α=0.5, respectively. The straight line in (a) indicates the model results at f_α=0.5 in the hypothetical case of a temperature dependence in nucleation distance.

Although a perfect agreement between the model and the measurements is not to be expected due to the many simplifications in the model, the very big difference in activation energy (Q_{exp}= 950 kJ/mol versus Q_{FEM}= 300 kJ/mol) for the alloy with a low Mn content (See Figure 7.13a) is rather surprising. When we examine the temperature dependence of parameters in the model, only the diffusion coefficient and the Δc_{Fe} are taken to be *T*-dependent while all geometrical factors are fixed. This assumption is probably incorrect for the nucleation distance must be *T*-dependent [20]. Unfortunately we did not succeed in determining it experimentally. However, we can use the model to explore the effect of a temperature dependent nucleation distance on the transformation rate. If we assume that at 540°C the nucleation distance is 7 times longer as that at 580°C, we get a better agreement between the apparent model predictions and the experimental data (see solid line in Figure 7.13a). In this case the experimental activation energy becomes close to the modelled apparent activation energy ($Q_{apparent}$=900 kJ/mol). This apparent activation energy is equal to the addition of the activation energy of diffusion (Q=183 kJ/mol), the activation energy of Δc_{Fe} (Q=~120 kJ/mol) and the activation energy of nucleation (Q=~600 kJ/mol). In contrast, for the alloy with a high Mn content the experimental activation energy (Q_{exp}=370 kJ/mol) was found to be close to the modelled activation energy (Q_{FEM}= 300 kJ/mol). This might suggest that for alloys with high Mn contents the nucleation activation energy is low (Q=~70 kJ/mol), and therefore the nucleation distances are only slightly *T*-dependent.

An other possible cause for the gap between the experimental and modelled transformation rates for alloys with a low Mn content is the fact that multi-components effects at the α-interface were not taken into account sufficiently. Since, strictly speaking, the displacement of the α-interface should be equal for all alloying elements that are in the α-particle. This poses an additional requirement on the relation between the interface concentrations of Mn and Fe. An estimate can be obtained by the use of the methods in Chapter 6. Due to low sensitivity of the Fe interfacial concentration for high Mn interfacial concentrations, this effect was not so important for the determination of the interface concentration in alloy A2, where only high Mn contents were considered. However, in the configuration where the Mn contents may be low, the multi-component balancing effects may be more pronouncing.

7.5.3 Industrial implications

A proper homogenisation leads to a considerable increase of the extrudability and to fewer surface defects on the aluminium profiles. Therefore, preferably an extrusion

ingot is homogenised to attain a high relative α fraction, e.g. at least f_α=0.8 and preferably more than f_α=0.9 [3]. Although the presented transformation model is not applicable to homogenisation up to high relative α-fractions, yet still some important implications for the alloy compositional dependence of the homogenisation kinetics can already be extracted from the numerical experiments.

Mg is added to the AA 6xxx alloy system to form the age hardable Mg-Si precipitates in the final extrusion product. However, since Mg has practically no influence on the interfacial concentrations on the β and α particles [11], this element has almost no influence on the transformation rate.

The Fe alloy content has some influence on the transformation speed since it influences the morphology of the cast β-AlFeSi particles. In AA 6xxx alloys, almost all the Fe in the alloy system will bind with the excess of Si and the abundant Al to form the β-intermetallics. Therefore, alloys with a low Fe concentration are preferable since after casting less β-intermetallic volume is formed and probably this leads to thinner β-plates which leads to a faster β-to-α transformation. Note that the Fe alloy content has hardly any influence on the Fe interfacial concentration of the β and α particles itself.

The Si content has an modest influence on the transformation rate. It appears that the Si matrix concentration has an effect on the Fe interfacial concentration of the β and α particles. Since only a small part of the Si alloy content binds to the β-AlFeSi particles, it can be assumed that the Si matrix concentration is approximately equal to the Si alloy content. It was found in the model that a low alloy Si content (e.g <0.5 wt.%) is preferable since this leads to a faster β-to-α transformation.

Of all alloying elements the Mn alloy content has the largest influence on the transformation rate. As it strongly affects the thermodynamic potential difference of the rate determing element Fe at the interfaces between the matrix at the β particle and the matrix at the α particle. A low Mn concentration of 0.01 wt.% leads to a very slow transformation rate or even to no transformation. It was found that small alloying additions of up to 0.2 wt.% Mn gives a large increase in the transformation rate. Finally our transformation model tells us that larger Mn additions in excess of 0.2 wt.% will give no significant extra increase of the transformation rate anymore. Therefore, for industrial purposes, a Mn content of approximately 0.2 wt.% is optimal for the transformation speed. Mn additions higher than 0.2 wt.% might only be useful for other alloying purposes, such as the formation of more dispersiods inside the Al-matrix.

From the experiments we conclude that the transformation rate for alloys with low Mn content (e.g. ~0.02 wt.% Mn) are highly temperature dependent. Therefore, for low Mn alloyed alloys, extra care for accurate temperature control is an important aspect to achieve an efficient homogenisation.

7.6 Conclusions

The Finite Element Model, as presented in Chapter 6, was used to describe the influence of the alloy content on the β-to-α transformation rate. Thermodynamic databases (Thermo-Calc) were used to derive the Fe interfacial concentrations at the interfaces of both the α and β intermetallics for several alloy compositions. The model predicts a significant effect of the Si and Mn alloy content on the transformation kinetics. It was found that Mn has the largest effect on the transformation rate. The results of the model correspond with trends found with experiments both presented in this chapter and observed by other authors. We conclude from this agreement that it is justified to use the hypothesis that the driving force of the transformation is the difference in Fe concentration at the Al-α and Al-β phase interfaces.

References

[1] L. F. Mondolfo: *Structure and Properties of Aluminium Alloys*. (Butter-worth, England, 1976).

[2] S. Zajac, B. Hutchinson, A. Johansson and L. O. Gullman: *Microstructure control and extrudability of Al-Mg-Si alloys microalloyed with manganese.* Mat. Sci. Tech. **10** (1994) 323-333.

[3] N. C. Parson, J. D. Hankin and K. P. Hicklin: *Al-Mg-Si alloy with good extrusion properties*, US-patent (2002) 6,440,359.

[4] L. Bäckerud: *Kinetic aspects of the solidification of binary and ternary alloy systems*. Jernkont. Ann. **152** (1968) 109-138.

[5] F. J. Vermolen and C. Vuik: *A mathematical model for the dissolution of particles in multi-component alloys.* Comput. Appl. Math. **126** (2000) 233-254.

[6] L. F. Mondolfo: *Aluminium Alloys: Structure and Properties*, Published by Butter Worths & Co Ltd, London-Boston (1976).

[7] H. W. L. Phillips: *Annotated equilibrium diagrams of some aluminium alloy systems*. The Institute of Metals, london (1959).

[8] V. Stefániay, A. Griger and T. Turmezey: *Intermetallic phases in the aluminium-corner of the AlFeSi-alloy system*. J. Mat. Sci. **22** (1987) 539-546.

[9] A. L. Dons: *AlFeSi-Particles in Commercial Pure Aluminium II*. Z. Metallkde. **77** (1986) 126-130.

[10] A. L. Dons: *AlFeSi-Particles in Industrial Cast Aluminium Alloys*. Z. Metallkde, **76** (1985) 609-612.

[11] P. Kolby: *Phase diagrams and phase equilibria.* In: T. H. Sanders, Jr. and E.A. Starke, Jr. editors. Aluminium alloys; their physical and mechanical properties (ICAA4). The Georgia Institute of Technology, Atlanta, U.S.A. volume III (1994) 2-17.

[12] Y. Langsrud: *Silicon in commercial aluminium alloys –what becomes of it during DC-casting?* Key Engineering Materials **44-45** (1990) 95-116.

[13] J. E. Tibballs, J. A. Horst and C. J. Simensen: *Precipitation of α-Al(Fe,Mn)Si from the melt*. J. Mat. Sci. **36** (2001) 937-941.

[14] G. Segal, C. Vuik and F. J. Vermolen: *A conserving discretization for the free boundary in a two-dimensional Stefan problem.* J. Comp. Phys. **141** (1998) 1-21.

[15] D. L. Beke, I. Gödény, I. A. Szabó, G. Erdélyi and F. J. Kedves: *On the diffuison of ^{59}Fe into aluminium and Al Mn soolid solutions*. Philos. Mag. **A5** (1987) 425-443.

[16] H. J. Lamb: *The effect of trace additions of manganese and prior heat-treatment on the structure of dilute Al-Mg-Si Alloy extrusion ingot*. Proc. of the Conf. on Phase Transformations, (London, England, 1979) Series 3, **No. 1, 2**, V4-V5.

[17] M. Ryvola and L. R. Morris: *Examination of insoluble intermetallic phases in aluminium alloys*. Microstruct. Sci. **5** (1977) 203-208.

[18] N. A. Belov, A. A. Aksenov and D. G. Eskin: *Iron in Aluminum Alloys, Impurity and Alloying Element.* (Taylor & Francis, Londen and New York, 2002) 132-136.

[19] J. W. Christian: *The theory of Transformations in Metals and Alloys, (*Pergamon Press, Oxford, 1965*)*.

[20] D. A. Porter and K. E. Easterling: *Phase transformations in Metals and Alloys*, (Chapman & Hall, London, 1997).

Summary of thesis

Kinetics of the β-AlFeSi to α-Al(FeMn)Si transformation in Al-Mg-Si alloys

Among all the process steps of the production of aluminium extrusion products, the homogenisation of Al-Mg-Si aluminium billets is a very important one, since it gives significant changes in the microstructure of the alloy, leading to an improved extrudability of the material and improved properties of the final extruded product. During this homogenisation process the aluminium billets are annealed in a furnace for a few hours at a temperature of approximately 585°C. One important microstructural change during homogenisation is the transformation of plate-like intermetallic β-Al_5FeSi particles into a string of separate coarse α-AlFeMnSi type of intermetallic particles. This β-to-α phase transformation considerably improves the extrusion process since the transformed α-particles in the homogenised material improve the ductility of the material and the surface quality of the extruded material.

A better understanding of the β-to-α transformation kinetics is important, since this gives more insight into the effects of process parameters of the homogenisation such as temperature, homogenisation time, as-cast microstructure and chemical composition. It is the objective of this research to characterise the β-to-α transformation kinetics in Al-Mg-Si alloys (6xxx alloys) by experiments and to develop a physical model that describes this transformation. Further, the research aims at gaining more insight into the behaviour of intermetallic phases during thermal processing.

Following the general introduction in Chapter 1, Chapter 2 presents a critical assessment of five experimental methods for the determination of the degree of transformation of β-AlFeSi intermetallics to α-$Al_{12}(FeMn)_3Si$ intermetallics. The degree of transformation is quantified by the relative α fraction (f_α), which is defined as the ratio of the α volume and the total volume of intermetallics. Four of the investigated experimental methods are based on microscopic classification of individual particles as either α-Al(FeMn)Si or β-AlFeSi and averaging the results by searching a sufficiently large surface area in the polished plane. For the classification of the intermetallics we use either the geometrical aspect ratio or the local chemical composition of the intermetallics. For these measurements we used optical microscopy, Scanning Electron

Microscopy (SEM), SEM in combination with Electron Diffractive X-ray (EDX), and SEM in combination with combined EDX selection criteria. In the fifth experimental method we measured X-Ray Diffraction (XRD) patterns of intermetallics extracted from the matrix. A procedure was developed on the basis of a simple error analysis, which yielded for all methods a reasonably good estimate (typically 13% variation) of the relative α-fraction transformed. The best estimate of the relative fraction transformed (typically 5 % variation) was obtained by using a combination of two classification criteria (the (Mn+Fe)/Si ratio and the absolute local Mn concentration) applied to individual intermetallic particles. The method is applicable to other AA 6xxx extrusion alloys, and can be fully automated and is relatively labour unintensive.

Chapter 3 presents the topological description of α_c-Al(FeMn)Si particles that have nucleated on β-AlFeSi plates in a partially homogenised 6000A Al alloy. Data were obtained using Laser Scanning Confocal Microscopy (LSCM) in combination with a deep etching technique to isolate the intermetallics from the matrix. The advantage of LSCM is that it is possible to obtain a sufficient lateral and vertical resolution, which yields a quantitative 3-dimensional topological description of the intermetallics. Formation of several α nuclei has been observed both on the plate edges and on the broad faces. Nuclei are distributed more or less uniformly over the surface of the β plate. Two different particle shapes are encountered: triangular and globular. The globular particles have typical sizes of approximately 0.3 μm. The triangular particles are facetted with a size of approximately 1 μm. No signs of preferential attack of either the α-Al(FeMn)Si particle or the β-AlFeSi plate near the interface is observed. Furthermore, due to the sharpness of the transition it seems reasonable to assume that all aluminium matrix material at the surface of the observed α and β intermetallics has been removed in the etching process. The obtained topographic information and nucleation densities are useful for the transformation models presented in Chapter 6 and 7.

The morphological evolution of both the α particles and β particles during the homogenisation process is described in Chapter 4. Scanning Electron Microscopy (SEM) in combination with a delicate electro-polishing method is used to classify various types of α particles at different stages of the homogenisation of a representative AA 6005A alloy. By the SEM analysis we are able to get statistically reliable results by classifying hundreds of α particles during our experiments. For the characterisation of α particles we used a classification scheme that distinguished several types of α particles by their position and morphology. Further, we investigated the evolution of the

morphology of the β-intermetallics during homogenisation. It appears that the β particles dissolve only at the rims. Their faces are not affected during homogenisation. Already in the beginning of the transformation these β plates break up into smaller plates. For the morphology evolution of the α particles we saw some interesting new features. In the early stages of the homogenisation (f_α=0.2) α particles start to nucleate on the main surfaces of the β plate. In later stages (f_α=0.5) those α particles grow closer to the rims of the β particles. Near the final stage (f_α=0.8) the α particles grow over the rims of the β particle. During homogenisation there is a mass transport of Fe and Si from the rim of the β particles towards the α particles, leaving the β plates to dissolve and the α particles to grow.

Two dimensional analyses can be misleading and therefore new techniques for a proper quantification of a three dimensional (3D) microstructure, such as a network of β plate intermetallics and its transformation products, are employed in Chapter 5. In this chapter we investigate the evolution of the 3D microstructural morphology during homogenisation heat treatment. To do so, samples are 40 times re-polished and imaged (at the same spot) by the Laser Scanning Confocal Microscope to create a stack of serial 2D sections at regular intervals along the z-axis. The serial sections are then used for 3D reconstruction of the intermetallics. The morphology of the intermetallics at the early stages of the β-to-α transformation is predominantly plate-like and interconnected. Nucleation of the α_c-$Al_{12}(FeMn)_3Si$ phase occurs on the initial β-Al_5FeSi plates. In the beginning of the transformation (f_α= 0-0.5) these nuclei grow and the β-Al_5FeSi plates break up at their edges. This will lead to both growth of the α_c-$Al_{12}(FeMn)_3Si$ particles and a related morphological evolution of the β-Al_5FeSi plates. At the final stages of the transformation (f_α = 0.5-1) the α_c-$Al_{12}(FeMn)_3Si$ particles become more cylindrical and the network connectivity decreases dramatically. The spatial distribution of the α_c-$Al_{12}(FeMn)_3Si$ cylinders still closely reflects the spatial distribution of the original β-Al_5FeSi plates.

In Chapter 6 a finite element model is presented which models the development of the α-fraction with time, by simulating the growth of an α particle on a β plate during the first stage of the transformation (f_α=0-0.5). In this model, a solubility difference between the matrix near the α interface and the matrix near the β-interface rim gives a mass transport of Si and Fe through the Al matrix between the two phases. Since the diffusion coefficient of Fe is much lower than the Si diffusion coefficient, we assume that diffusion of Fe is the rate-determining step. This makes the α particle grow and the β plate dissolve. The movement of the β and α interfaces are mathematically treated as

a Stefan problem, using interfacial solubilities that are derived by thermodynamic calculations (Thermo-Calc). The transformation fraction is calculated for several input parameter values that are estimated from experimental observations. The model predicts a strong effect of temperature and intermetallic morphology on transformation kinetics. In spite of major simplifications in initial morphologies of the intermetallics the calculated Finite Element Model (FEM) results agree qualitatively with experimental data over a large range of temperatures. A simple analytical model, based on the same morphologies as in the FEM, yields qualitatively the same behaviour. We conclude from a good agreement between the FEM calculations and experiments that the rate-controlling mechanism of the β-to-α transformation is iron diffusion.

In Chapter 7 the influence of the alloying elements, Mg, Fe, Si and Mn on the rate of the β-to-α transformation is studied. The Finite Element Model, as presented in Chapter 6, is used to model the influence of the alloy content on the β-to-α transformation rate. Thermodynamic databases (Thermo-Calc) are used to derive the interfacial concentrations of Fe at the interfaces of both the α and β intermetallics for different alloy compositions. It is found that Mn has the largest effect on the transformation rate and that the dependence is clearly non-linear with three distinctively different domains. The results of the model correspond with trends found with experiments presented in this chapter and those observed by other authors. However, some discrepancies between the model and the experiment remain, which are attributed to the simplifying assumptions for the α nucleation density and the inaccurate treatment of multi-component effects.

N.C.W. Kuijpers, Delft University of Technology, 2004.

Samenvatting van proefschrift

Kinetiek van de β-AlFeSi naar α-Al(FeMn)Si transformatie in Al-Mg-Si legeringen

Een belangrijke processtap in de productie van aluminium extrusie-producten, zoals buizen en profielen, is het homogeniseren van gegoten Al-Mg-Si aluminium palen (billets), omdat deze stap aanzienlijke veranderingen in de microstructuur van de legering veroorzaakt, en daardoor leidt tot een verbeterd extrusie-product. Gedurende dit homogeniseerproces worden aluminium billets gedurende een aantal uur verwarmd rond 585°C. Een belangrijke microstructurele verandering is de transformatie van plaat-vormige β-Al_5FeSi deeltjes naar meerdere kleinere bolvormige α-Al(FeMn)Si intermetallische deeltjes. Deze getransformeerde α-deeltjes leiden tot verbeteringen in zowel de vervormbaarheid als de oppervlaktekwaliteit van het materiaal.

Een beter begrip van de kinetiek van de β-naar-α transformatie geeft meer inzicht in het effect van verschillende procesparameters zoals temperatuur, homogenisatietijd, microstructuur en chemische compositie op het homogenisatieproces. Dit onderzoek heeft als doelstelling om de β-naar-α transformatie in Al-Mg-Si legeringen (AA 6xxx legeringen) te karakteriseren met behulp van experimenten, en om een fysisch model te ontwikkelen dat deze transformatie beschrijft. Tevens omvat dit onderzoek de bredere doelstelling om meer inzicht te verkrijgen in het gedrag van intermetallische fases gedurende een thermisch proces.

Na een algemene introductie in Hoofdstuk 1 wordt in Hoofdstuk 2 een kritische beoordeling gepresenteerd van vijf experimentele methoden voor de bepaling van de mate van intermetallische transformatie. Deze is gekwantificeerd in de zogenaamde relatieve α fractie (f_α), welke gedefinieerd is als de verhouding tussen het totale volume van de α deeltjes en het totale volume van alle intermetallische deeltjes. Vier van de geïnventariseerde experimentele methoden zijn gebaseerd op microscopische classificatie van individuele deeltjes als α-Al(FeMn)Si of β-AlFeSi waarna het resultaat door het analyseren van een voldoende groot gepolijst oppervlak wordt uitgemiddeld. Voor de classificatie van de intermetallische deeltjes gebruiken we de geometrische hoogte-breedte verhouding en/of de lokale chemische compositie van de intermetallische fasen. Voor deze metingen hebben we gebruik gemaakt van optische

microscopie, Scanning Elektronen Microscopie (SEM), SEM in combinatie met Electron Disperisive X-ray (EDX), en SEM/EDX in combinatie met zekere selectie criteria. Bij de vijfde experimentele methode zijn röntgen diffractie (XRD) patronen gemeten van intermetallische fasen die aan de Al-matrix zijn onttrokken. Een kwantitatieve procedure is ontwikkeld op basis van een eenvoudige foutanalyse, welke voor alle methoden tot een redelijk goede afschatting (typisch 13 % variatie) van de relatieve α-fractie leidt. De beste benadering van de relatieve fractie (typisch 5% variatie) werd gevonden met het gebruik van een combinatie van twee classificatie criteria (de (Mn+Fe)/Si verhouding en de lokale Mn concentratie) die zijn uitgevoerd op individuele intermetallische deeltjes. Deze methode is ook toepasbaar op andere AA 6xxx extrusie legeringen en kan eveneens automatisch worden uitgevoerd. Tevens is deze methode in verhouding tot XRD minder arbeidsintensief.

Hoofdstuk 3 beschrijft de topologische beschrijving van α_c-Al(FeMn)Si deeltjes welke zijn ontkiemd (genuclieerd) op de β-AlFeSi platen in een gedeeltelijk gehomogeniseerde AA 6000A legering. Experimentele gegevens werden gevonden met gebruikmaking van de Laser Scanning Confocal Microscope (LSCM) in combinatie met een diep-ets techniek om de intermetallische fasen van de matrix te isoleren. Het voordeel van LSCM is dat een voldoende laterale en verticale resolutie kan worden behaald, die resulteert in een kwantitatieve 3-dimensionale topologische beschrijving van de intermetallische fasen. Meer typen α nucleaties zijn gevonden, zowel op de randen als op de vlakken van de β plaat. Deze α deeltjes zijn min of meer uniform verdeeld over het oppervlak van de β plaat. Twee verschillende vormen van α deeltjes zijn gevonden: driehoekige en bolvormige. De bolvormige deeltjes hebben een typische grootte van ongeveer 0.3 μm. De driehoekige deeltjes zijn gefacetteerd en hebben een grootte van ongeveer 1 μm. Er is geen aanwijzing gevonden dat het diep-ets proces de α-deeltjes of de β platen aantast. Door de scherpte van de overgang kan worden aangenomen dat al het aluminium verwijderd is bij het oppervlak van de waargenomen α en β intermetallics door het ets-proces. De geobserveerde topologie, en nucleatie dichtheden worden als input gebruikt voor de parameters van de transformatie modellen in Hoofdstuk 6 en 7.

Hoofdstuk 4 onderzoekt de twee-dimensionale morfologie veranderingen van zowel de α deeltjes als de β deeltjes gedurende het homogeniseringsproces. SEM in combinatie met een verfijnde elektro-polijst methode is gebruikt om de α deeltjes van de β deeltjes te onderscheiden in een representatieve AA 6005A legering. Met behulp van de SEM analyses is het mogelijk om statistisch betrouwbare resultaten te verkrijgen door middel

van de karakterisering van enkele honderden α deeltjes. Voor de karakterisatie van de α deeltjes hebben we een indelingsschema gebruikt dat vijf verschillende typen α deeltjes onderscheidt door hun positie en morfologie. Gedurende verschillende stadia van het homogenisatie proces hebben we voor elk stadium 300 α deeltjes ingedeeld in de verschillende types. Dit geeft een duidelijk beeld van de morfologische verandering van de α deeltjes gedurende het homogeniseer proces. Hiernaast hebben we ook de evolutie van de morfologie van de β-intermetallische fasen onderzocht. Het blijkt dat de β deeltjes alleen aan de randen oplossen en dat de vlakken van de β platen niet worden aangetast gedurende homogenisatie. Al in het begin van de transformatie breken de β platen op naar kleinere platen. Voor de morfologische veranderingen van het α deeltje zagen we enkele interessante eigenschappen. In het vroege stadium van de homogenisatie (f_α=0.2) nucleëren α deeltjes aan de oppervlakken van de β platen. In een later stadium (f_α=0.5) groeien deze α deeltjes dichter tot de randen van de β deeltjes. Tijdens het late stadium van de transformatie (f_α=0.8) groeien de α deeltjes over de randen van de β deeltjes. Gedurende de homogenisatie is er een massa transport van Fe en Si vanaf de randen van de β deeltjes tot aan de α deeltjes, waardoor de β deeltjes oplossen en de α deeltjes groeien.

Twee dimensionale analyse van microstructuren kan misleidend zijn, en daarom wordt er in Hoofdstuk 5 een nieuwe techniek onderzocht voor het kwantificeren van drie dimensionale (3D) microstructuren, bestaande uit het netwerk van intermetallische β platen en de getransformeerde α deeltjes. In dit hoofdstuk onderzoeken we het verloop van de 3D morfologie van de intermetallische fasen gedurende de homogenisatie. Hiervoor zijn proefstukken 40 keer gepolijst en vervolgens afgebeeld (op hetzelfde gebied) met de LSCM. Hierdoor ontstaat een rij opeenvolgende twee dimensionale (x,y) dwarsdoorsneden met min of meer regelmatige afstanden op de z-as. Deze opeenvolgende dwarsdoorsneden zijn hierna gebruikt voor de 3D reconstructie van het intermetallische netwerk. De morfologie van de intermetallische fasen is in het begin van de transformatie hoofdzakelijk plaatvormig en de platen zijn onderling verbonden. Op de β platen vormen zich nucleaties van de α fases. In het beginstadium van de transformatie (f_α=0-0.5) groeien deze nucleaties aan en breken de β platen aan de randen op. Dit leidt tot zowel groei van de α fasen als gerelateerde morfologische veranderingen van de β platen. In het eindstadium van de transformatie (f_α=0.5-1) worden de α deeltjes cilindrisch. Deze α deeltjes zijn onderling niet zo sterk met elkaar verbonden; echter, de ruimtelijke verdeling van de α deeltjes reflecteert nog steeds de plaats van de voormalige originele β platen.

In Hoofdstuk 6 wordt een Eindig Elementen Model (FEM) gepresenteerd dat het verloop van de α fractie in de tijd modelleert door het simuleren van de groei van een α deeltje op een β plaat gedurende het eerste stadium van de transformatie (f_α=0-0.5). In dit model wordt gebruik gemaakt van het verschil tussen de grensvlakconcentraties van het α deeltje en het β deeltje, dat leidt tot een massa transport van Si en Fe door de Al matrix tussen de twee fases. Hierdoor groeien de α deeltjes en lossen de β platen op. Omdat de diffusiecoëfficiënt van Fe veel kleiner is dan die van Si, nemen we aan dat de diffusie van Fe de snelheidsbepalende stap is. De beweging van de grensvlakken van de β en α deeltjes zijn wiskundig benaderd als een Stefan-probleem, waarbij de grensvlakconcentraties zijn uitgerekend door thermodynamische berekeningen (Thermo-Calc). De getransformeerde fractie is uitgerekend met het FEM waarbij gebruik wordt gemaakt van experimentele input parameters. Het model voorspelt een groot effect van de temperatuur en de intermetallische morfologie op de transformatie kinetiek. Ondanks grote vereenvoudigingen in de begin morfologie van de intermetallics in het model, komen de gemodelleerde getransformeerde fracties kwantitatief overeen met de experimentele fracties. Een simpel analytisch model, gebaseerd op dezelfde morfologie als in het FEM, leidt kwalitatief tot hetzelfde gedrag. Vanwege de goede overeenkomst tussen de FEM resultaten en experimenten, concluderen we dat Fe diffusie het snelheid bepalende mechanisme is van de β-naar-α transformatie.

In Hoofdstuk 7 wordt de invloed van de legeringselementen, Mg, Fe, Si en Mn op de snelheid van de β-naar-α transformatie bestudeerd. Het Eindige Elementen Model, wordt gebruikt om de invloed van de legeringshoeveelheid op de β-naar-α transformatie snelheid te onderzoeken. Een thermodynamische database (Thermo-Calc) is gebruikt om de Fe grensvlakconcentraties van zowel de α als de β intermetallics voor verschillende legeringsamenstelling te berekenen. Mn heeft het grootste effect op de transformatie snelheid en de mate van afhankelijkheid is onder te verdelen in drie verschillende concentratiegebieden. De resultaten van het model komen overeen met de trend die gevonden is in experimenten beschreven in dit hoofdstuk, en observaties van andere auteurs. Er blijven enkele discrepanties over, die worden toegekend aan de vereenvoudigde aannamen van de nucleatiedichtheden van de α deeltjes en een onnauwkeurige behandeling van multi-component effecten.

N.C.W. Kuijpers, Technische Universiteit Delft, 2004.

Dankwoord

In de eerste plaats gaat mijn erkentelijkheid uit naar de mensen die mij direct begeleid en ondersteund hebben bij het schrijven van mijn proefschrift. Professor Sybrand van der Zwaag wil ik graag bedanken voor zijn kritische beschouwingen bij het opzetten van mijn experimenten en het snelle nakijken van mijn stukken. Fred Vermolen en Kees Vuik wil ik hartelijk danken voor het altijd openstaan voor verbeteringen en de prettige discussies omtrent mijn promotieonderwerp. Mijn dankbaarheid gaat ook uit naar Pim Kool vanwege zijn kritische correcties die erg leerzaam waren voor mijn schrijfvaardigheden.

Ook Peter Koenis (BOAL, de Lier) wil ik speciaal bedanken. Hij was altijd behulpzaam bij het doormeten van mijn samples met zijn SEM. Ook Johan Tirel ben ik bijzonder dankbaar voor zijn bijdrage aan de drie-dimensionale reconstructies van de intermetallics en niet minder voor de leuke en nodige sociale afwisseling die we op zaterdagavonden hebben gehad in Leiden.

De prettige werksfeer in de Microstructure Control of Metals (MCM)-groep heb ik bijzonder gewaardeerd. In het bijzonder wil ik de vaste staf bedanken voor hun ondersteuning: Erik Peekstok, Nico Geerlofs en Ton de Haan voor hun hulp op het experimentele vlak; onze secretaresse, Olga Wens (de stille kracht achter de MCM-groep), voor het geven van nuttige administratieve tips en Jilt Sietsma voor het altijd openstaan voor vragen en het betoonde respect voor zijn medewerkers. Tevens wil ik Jilt bedanken voor de ruimte die hij mij heeft gegeven om, na mijn NIMR-contract, als gast van de MCM-groep een tijdelijk onderzoek uit te voeren voor PamGene International b.v. te 's Hertogenbosch. Mijn dank treft ook het meest wijze lid van MCM: Bert Korevaar. Ook veel oud-leden wil ik bedanken: Jörgen van der Langkruis voor de eerste inleidingen in de materiaalkunde van het aluminium; Iain Todd voor de nuttige wetenschappelijke tips die hij mij gegeven heeft en Shang Ping Chen voor de pittige discussies en de goede raad bij het schrijven van artikelen. Verder wil ik mijn oud-collega's Roland van Straaten, Bruce Davenport, Willemijn van Til, Elly Hilkhuijsen, Arjen Mol, Jiajun Wang, Ton Gommers, Martin Huisert, Theo Kop, Pieter van der Wolk, Ali Gholinia en Dave Hanlon bedanken voor de prettige samenwerking. Natuurlijk treft mijn erkentelijkheid ook alle nieuwe leden van de MCM-groep: Erica Anselmino, voor het aangeven van de trend in de Italiaanse mode; Rias Lok voor het bij de tijd zijn; Haiwen Luo voor het wachten tot zijn computer wordt gehackt (Hack-When?); Anne Mertens voor de lekkere Belgische bonbons;

Erik Offerman voor zijn beleefdheid; Ali Smith (Smidje) voor de biertjes die we samen hebben gedronken; Lie Zhao voor het geven van de rust in mijn kamer waardoor ik mijn proefschrift kon afschrijven; Suzelotte Kruijver voor de leuke bruiloft in Drachten; Alexis Miroux voor de lekkere Spaanse ham, maar ook voor de inhoudelijke discussies met betrekking tot mijn promotie; Thim Zuidwijk (dr. Gleeble), voor het brouwen van de lekkere biertjes; Pina Mecozi voor de prettige wetenschappelijke discussies en de studentes Hiske Landheer en Sietske Geuzebroek voor de extra sfeer die zij in de MCM-groep brachten.

Verder zijn er veel mensen van de TU-Delft, buiten de MCM-groep, die ik speciaal wil bedanken: het koppel Niek van der Pers en Han van Lent voor de gezellige gesprekken aan tafel omtrent de röntgen diffractie metingen; Jouk Jansen voor de ondersteuning van de röntgen diffractie berekeningen; Kees Kwakernaak en Han Kiersch voor de ondersteuning bij de SEM metingen; Jianghua Chen voor TEM metingen op de intermetallics; Etelvina Javierre Perez voor de wiskundige discussies en Peter Overkamp, Bart Norbart, Lidy Apachitei-Fratila en Bram Huis voor de hulp die zij boden aan een tijdelijk onderzoek op de faculteit Materiaalkunde na mijn NIMR-periode. Graag wil ik ook de stagiaires Sylvia Leever, Denis van Kroonenburg en Joris Hofhuizen vernoemen. Het was voor mij een leerzame ervaring om deze stagiaires te mogen begeleiden.

Mijn dank gaat ook uit naar verscheidene mensen uit het bedrijfsleven, waaronder natuurlijk de eerder genoemde Peter Koenis en Kjell Nilsen (BOAL, de Lier) voor het inbrengen van belangrijke industriële doelstellingen in mijn onderzoek. Hans Winter (Corus, IJmuiden) wil ik bedanken voor het meehelpen aan de Sibut extractie van intermetallics en Jan Pieter Mulder (Aldel, Delfzijl) voor het uitvoeren van enkele experimenten en voor de belangstelling voor mijn onderzoek. Ook ben ik natuurlijk het Netherlands Institute for Metals Research (NIMR) bijzonder erkentelijk voor het financieren van mijn promotieonderzoek.

Als laatste, maar niet in het minst, ben ik mijn ouders dankbaar voor de morele steun die zij mij gegeven hebben en voor het meehelpen klussen in mijn huis in Delft. Mijn broer Maarten en zijn vrouw Marjan wil ik ook bedanken voor het aanhoren van de vele telefoontjes vanuit Delft en het meehelpen verhuizen naar Delft. Niet in het minst ook wil ik mijn vriendin Cynthia danken, met name voor de bemoediging toen de laatste loodjes van dit proefschrift zwaar begonnen te wegen.

Appendix 1

Calorimetric study on Mg-Si phases in as cast AA 6xxx

As cast billets of AA6xxx alloys require a homogenisation treatment to make the material suitable for hot extrusion. During this homogenisation treatment several processes take place such as the transformation of interconnected plate-like β-$A1_5FeSi$ intermetallics into more rounded discrete α-$A1_{12}(FeMn)_3Si$ particles and the dissolution of β-Mg_2Si particles. Precipitation and dissolution of Mg-Si phases in as cast material were investigated for various Fe contents (0.02 wt.%, 0.19 wt.% and 0.65 wt.%) by means of DSC measurements and optical microscopy. Eutectic melting was also studied. In as cast material, the amount of Fe-containing intermetallics increases with Fe content. It appears that the amount of precipitation of β′′ and β′ Mg-Si phases during the DSC scan is lower for higher Fe content and that the corresponding activation energies are similar and independent of the Fe content. The amount of eutectic melting is dependent on the time involved with the DSC scan.

A1.1 Introduction

As cast billets of AA6xxx require a homogenisation treatment to make the material suitable for hot extrusion. During this homogenisation treatment several processes take place such as the transformation of interconnected plate-like β-A15FeSi intermetallics into more rounded discrete α_c-$A1_{12}(FeMn)_3Si$ particles and the dissolution of β-Mg_2Si particles [1]. Transformation of β-Al_5FeSi to α_c-$A1_{12}(FeMn)_3Si$ intermetallics is important because it improves the ductility of the material [2]. Dissolution of β-Mg_2Si is also important since it will give maximum age hardening potential for the extruded product and will suppress the generation of surface defects due to local melting [3,4]. Although the precipitation and dissolution of Mg-Si phases in already homogenised and aged material have been studied in detail [5-7], such studies are not found for as cast materials.

It is known that the concentration of Fe influences the β-Al_5FeSi to α_c-$Al_{12}(FeMn)_3Si$ transformation kinetics and the amount and morphology of these phases [8]. Also some influence of Fe on the precipitation and dissolution of the Mg-Si phases might be expected. A strong influence of the Fe content on the diffusion of Mg and Si or

their solubility is not anticipated since for a very low Fe content the maximum solubility of Fe in Al has already been reached. Therefore, the activation energies of dissolution and precipitation of Mg-Si phases are expected to be independent of Fe content. However, an indirect influence of the Fe content might be present since Fe will affect the morphology and spatial distribution of the Fe containing intermetallics in the eutectic and therefore that of the Mg_2Si particles in the eutectic. Furthermore, the Si concentration in the matrix may depend on the Fe content because of the incorporation of Si in the Fe containing intermetallics.

The aim of this study is to investigate precipitation, dissolution and eutectic melting of Mg-Si particles in the as cast structure of AA6xxx for various Fe contents. To this purpose both optical microscopy and Differential Scanning Calorimetry (DSC) measurements were performed.

A1.2 Experimental

A 1.2.1 Materials and microstructural characterisation.

Table 1 shows the compositions of three as cast Al-Mg-Si-Fe alloys. The Mg and Si contents in each alloy are approximately equal whereas the Fe content varies between 0.02 and 0.65 wt.%. Since these alloys do not contain Mn, the Fe containing intermetallics consist of β-Al_5FeSi and/or α_c-$Al_{12}Fe_3Si$. The alloys were cast in steel moulds of 200 mm x 150 mm x 400 mm and subsequently air cooled. All samples for optical characterisation and DSC measurements were taken at least 20 mm from the edge of the ingot to get a similar microstructure and composition.

Table 1 Alloy composition [wt.%] for alloys A, B and C.

Alloy	Mg	Si	Fe	Other	Al
A	0.75	0.52	0.02	<0.01	Balance
B	0.76	0.45	0.19	<0.01	Balance
C	0.82	0.49	0.65	<0.01	Balance

In the optical micrographs, the Al matrix appears as light grey areas, the β-Al_5FeSi and α_c-$Al_{12}Fe_3Si$ intermetallics as medium grey particles and the β-Mg_2Si as dark grey particles. Also differences in morphology between the different types of particles are visible. The volume fraction of the intermetallics in each casting was determined. By

automatic SEM and EDX measurements the volume fraction of α_c-$Al_{12}Fe_3Si$ and β-Al_5FeSi was determined, which method was described in detail in Chapter 2.

A1.2.2 DSC measurements.

DSC measurements were performed using a Perkin and Elmer DSC7 with a sample weight of approximately 60 mg. Pure aluminium was used as a reference. Temperature scans were made from 20°C to 605°C with constant heating rates of 5, 10, 20 or 40 °C/min. A baseline was obtained by fitting a polynomial at points in the curve where no reactions occurred. The activation energies of the precipitation of β˝ and β′ Mg-Si and the precipitation and dissolution of β-Mg_2Si were obtained by the Kissinger method [9,10]. The activation energy Q is determined from the slope of the straight line obtained by plotting $\ln(T_p^2/\phi)$ versus $1/RT_p$, where T_p is the peak temperature of the reaction, ϕ is the heating rate and R is the gas constant.

A1.3 Results

A1.3.1 Optical microscopy

Figure A1.1 shows micrographs of two as cast microstructures (alloys B and C). The intermetallics and the Mg-Si particles are clearly distinguishable. The particles are plate-like and appear as needles in the micrographs (See Chapter 5). The Mg-Si particles are precipitated as β-Mg_2Si on the boundaries of the Fe containing particles, as isolated β-Mg_2Si particles on the boundaries of the Al-dendrites, or as much smaller β-Mg_2Si or β′ Mg-Si precipitates in the matrix. The larger β-Mg_2Si particles, present in the interdendritic liquid accompanying the eutectic reaction during casting, are more spherical with a diameter of approximately 2 μm or larger. The β-Mg_2Si or β′ Mg-Si particles in the Al matrix have a needle shape and their width is smaller than 0.5 μm. They are precipitated from the supersaturated solid matrix during cooling of the casting. Close to the Fe containing particles there is a solute depleted zone where no Mg-Si particles are precipitated.

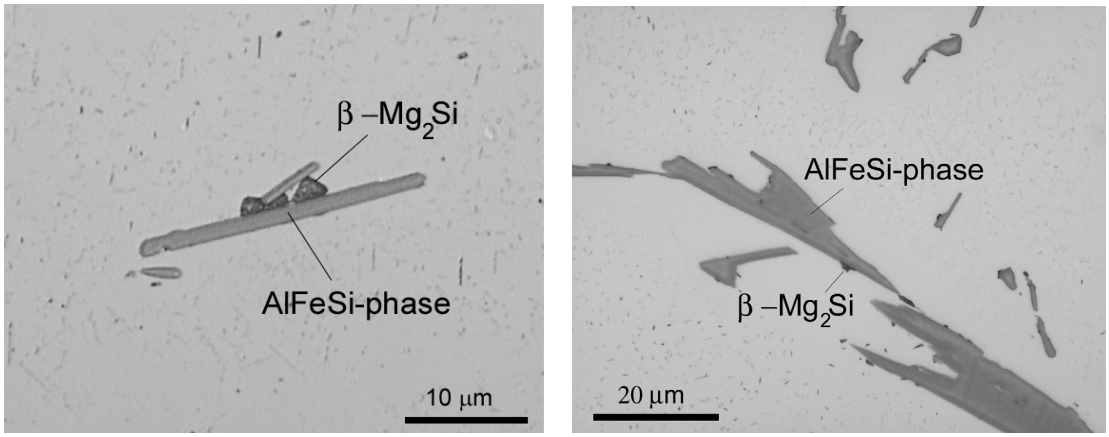

Figure A1.1 Optical micrographs of alloys B (a) and C (b).

Table A1.2 gives an overview of the measured volume concentration of β-Al_5FeSi and α_c-$Al_{12}Fe_3Si$ intermetallics. Also the calculated volume concentration of intermetallics is given assuming that all Fe in the alloy is bound in the intermetallic phases. The volume fraction of intermetallics increases as the Fe content increases. The calculated intermetallic volume fraction is slightly higher than the measured fraction, since some Fe is in solid solution or precipitated in small particles which were not detected by the imaging system. Measurement of the amount of Mg-Si and β-Mg_2Si particles present in the matrix was not possible because most particles were too small to analyse quantitatively by optical or SEM measurement.

Table A1.2 Volume concentrations [vol.%] of intermetallic phases present.

Alloy	α_c-$Al_{12}Fe_3Si$ (measured)	β-Al_5FeSi (measured)	αc-$Al_{12}Fe_3Si$ + β-Al_5FeSi (calculated)
A	<0.1	<0.1	<0.1
B	0.3 ± 0.1	0.1 ± 0.1	0.5
C	0.6 ± 0.2	0.6 ± 0.2	1.9

A1.3.2 DSC measurements.

DSC scans of alloys A, B and C are shown in Figure A1.2 for a heating rate of 40°C/min. Six peaks are visible in the plots, indicated by (1) to (6). The exothermic peak (1), with a maximum at approximately 320°C, is due to the formation of β´´ Mg-Si particles [5]. The exothermic peak (2), with a maximum at approximately 350°C, is caused by the formation of β´ Mg-Si particles [5]. There is a large overlap of the peaks (1) and (2). The exothermic peak (3), with a maximum at approximately 450°C, is caused by the precipitation of β-Mg_2Si particles [5]. The endothermic peak (4), with

maximum at approximately 540°C, is due to the dissolution of the Mg_2Si particles. The small endothermic peak (5), with an onset of approximately 578°C, is caused by eutectic melting of Al+Mg_2Si+β-Al_5FeSi→L+α′-Al_8Fe_2Si [3]. It appears only in the alloy with a high Fe content (alloy C). The endothermic peak (6), with an onset temperature of approximately 587°C, is caused by the eutectic melting of Al+Mg_2Si→L [11].

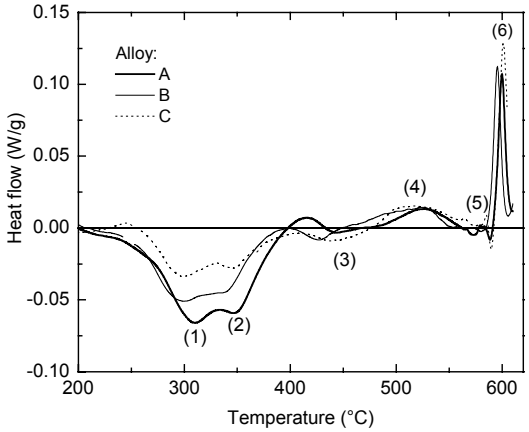

Figure A1.2 DSC scans for alloys A, B and C; heating rate: 40°C/min. The characteristic peaks are indicated by (1) to (6).

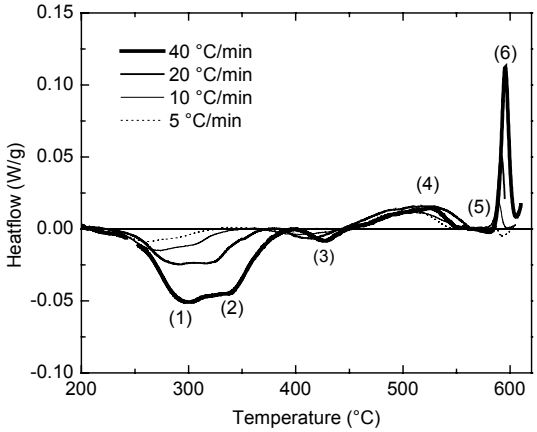

Figure A1.3 DSC scans for alloy B for various heating rates.

It is found that peaks (1) and (2) decrease as a function of Fe content, which means that fewer β′′ and β′ Mg-Si particles are precipitated. Since more Si is bound to the Fe containing particles in alloys with higher Fe content, the resulting Si concentration in solute solution is lower and precipitation of β′′ and β′ Mg-Si particles will decrease. As the intensity and position of peak (4) are independent of Fe content, the dissolution of the Mg_2Si particles is not influenced by the Fe content.

A1.3.3 Kinetics of precipitation and dissolution of Mg-Si phases.

Figure A1.3 presents the DSC results of alloy B for various heating rates. The peak temperatures of peak (1) to (4) shift as a function of heating rate. Figure A1.4 shows the Kissinger plots of peak (1) to (3) of alloy B. Straight lines are observed for this alloy and also for alloys A and C. Table 3 summarises the activation energies obtained from the Kissinger plots. Within experimental error, the activation energies of β′′ and β′ precipitation are the same for all three alloys. The activation energies for the precipitation of β-Mg_2Si are higher but also the same for the three alloys.

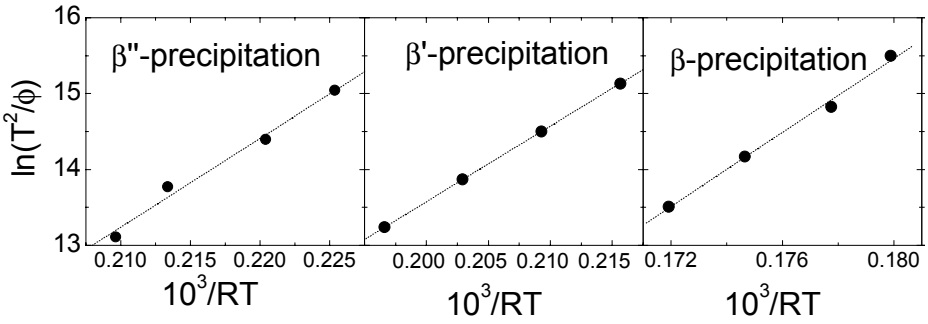

Figure A1.4 Kissinger plots of the different peaks found for alloy B.

The activation energies measured correspond well with those derived from the data published by Doan *et al.* [5], which results are also given in Table 3. The activation energies of the precipitation of β´´ and β´ are close to the reported activation energies for diffusion of Mg and Si in Al, which are in the range of 120-140 kJ/mol [12,13].
The activation energies, determined from the Kissinger plots for peak (4) (dissolution of β-Mg_2Si) are in the range of 500 ± 250 kJ/mol and are much higher than the activation energies reported above, in spite of the large uncertainty in the values. Also from the published data in Ref. [3], we derive comparable high values.

In Figure A1.5 the released heat of β-Mg_2Si dissolution (peak 4) is plotted as a function of heating rate. The heat of dissolution decreases with increasing heating rate, which implies that at a higher heating rate less β-Mg_2Si gets dissolved. Within experimental error no effect of Fe content was found.

Table A1.3 Activation energies found by the Kissinger method. Values derived from literature data for AA6061 [5] are also given.

Alloy	β´´ precipitation [kJ/mol]	β´ precipitation [kJ/mol]	β-Mg_2Si precipitation [kJ/mol]
A	115± 10	110± 10	175± 15
B	117± 10	100± 10	182± 15
C	125± 10	112± 10	170± 15
AA6061	105	93	100-300

A1.3.4 Eutectic melting.

In Figure A1.6 the heat released with eutectic melting (peak (6)) is plotted as a function of heating rate. It is found that the total heat increases as a function of heating rate which means that less β-Mg_2Si is present in the microstructure after heating till the onset of peak (6). This trend corresponds with the trend as presented in Figure A1.5,

indicating that during the DSC scan for high heating rates less β-Mg_2Si gets dissolved, and that more β-Mg_2Si remains in the eutectic and contributes to eutectic melting. Within experimental error no effect of Fe content was found.

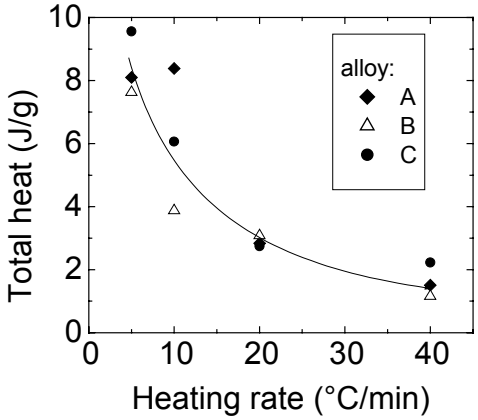

Figure A1.5 The released heat of β-Mg_2Si dissolution for alloys A, B and C.

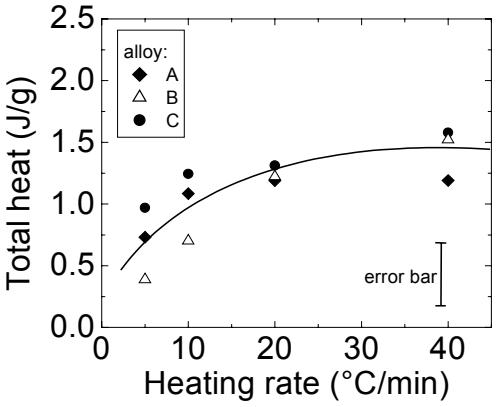

Figure A1.6 The released heat of eutectic melting for alloys A, B and C.

A1.4 Conclusion

The amount of β′′ and β′ Mg-Si precipitation is lower for higher Fe content. This is attributed to the incorporation of a part of the Si into the α_c-$Al_{12}Fe_3Si$ and β-Al_5FeSi intermetallics and consequently to a lower Si solute level.

Activation energies for the β′′ and β′ Mg-Si precipitation are similar and correspond well to the literature data. They are independent of the Fe content in the alloy. The activation energies of the β-Mg_2Si precipitation are higher than those obtained for β′′ and β′ Mg-Si precipitation and are also independent of the alloy content in the alloy. The activation energy of β-Mg_2Si dissolution is much higher.

The heat connected with the eutectic melting of Al +β-Mg_2Si decreases for lower heating rates. During the DSC-scan a certain amount of homogenisation of the as cast alloy has already taken place, leading to a lower amount of eutectic left at the onset of eutectic melting.

References

[1] S. Zajac, B. Hutchinson, A. Johansson and L. O. Gullman: *Mat. Sci. and Tech.* **10** (1994) 323.

[2] J. Langerweger: *Proc. of Conf. on Aluminium Technology*, London, March 1986 (1986) 216.

[3] T. Minoda, H. Hayakwa and H. Yodida: *Sumito Light Metal Technical Reports* **39** No. 1 (1998) 26.

[4] K. Karhausen, A. L. Dons and T. Aukrust: *Mat. Sci. Forum* **217-222** (1996) 403.
[5] L. C. Doan, Y. Ohmori and K. Nakai: *Mat. Trans. JIM* **41** No 2 (2000) 300.
[6] S. P. Chen, M. S. Vossenberg, F. J. Vermolen and J. van de Langkruis, *Mat Sci. and Eng. A* **272** (1999) 199.
[7] H. Westengen and N. Ryum: *Z. Metallkde* **70** (1979) 528.
[8] H. Tanihata, T. Sugawara, K. Matsuda and S. Ikeno: *J. Mat. Sci.* **34** (1999) 1205.
[9] H. E. Kissinger: *Anal. Chem.* **29** (1957) 1702.
[10] S. P. Chen, K. M. Mussert and S. van der Zwaag: *J. Mat. Sci.* **33** (1998) 4477.
[11] N. Chakraborti and H.L. Lukas: *Calphas* **16** (1992) 79.
[12] S. Fujikawa, K. Hirano and Y. Fukushima: *Mat. Trans. A.* **9A** (1978) 1811.
[13] S.I. Fujikawa: *Defects and Diffusion Forum* **143-147** (1997) 403.

Appendix 2

Derivation of solubility product of β-AlFeSi

For the dissolution of precipitates, such as β-Mg_2Si, solubility products are applied to express the boundary conditions of the concentration [1]. In the β-Al_5FeSi intermetallic phase also aluminium is present in the particle. This gives a shift in the phase diagram of the particle composition towards the Al-phase. It is not clear whether the solubility product is still valid if the Al content in the β-AlFeSi particle is high, and therefore this will be investigated in this appendix.

We assume that the interfacial aluminium matrix is an ideal solid phase of Al, Fe and Si with atomic fractions c^s_{Al}, c^s_{Fe}, c^s_{Si}. When we neglect the mixing energies of different phases the Gibbs free energy of the Al-interface (G^s) is described by [2]:

$$G^s(c_{Al}, c_{Fe}, c_{Si}) = \sum_{i \in \{Al, Fe, Si\}} \left(c_i G_i^m(T) + RT c_i^s \ln c_i^s \right), \tag{A2.1}$$

Where R is the universal gas constant and T the temperature in Kelvin and G_i^m are the molar free energies of the pure elements in the matrix phase. Note that G_i^m decreases as the temperature increases.

The Gibbs free energy of the β-Al_5FeSi phase (G^p) is strongly minimised at its stoichiometric composition, c^p_{Al}=3/7, c^p_{Fe}=1/7, c^p_{Si}=1/7:

$$G^p(c^p_{Al}, c^p_{Fe}, c^p_{Si}) = G^p_{stoich} \tag{A2.2}$$

All compositions that deviate from the stoichiometric composition leads to a drastic increase of the G^p. Therefore, it is energetically favourable for the phase to stay in its stoichiometric composition.

In general, the Gibbs free energy can be expressed by the chemical potentials (μ_{Al}, μ_{Fe} and μ_{Si}) and the compositions:

$$G = \mu_{Al} c_{Al} + \mu_{Fe} c_{Fe} + \mu_{Si} c_{Si} \tag{A2.3}$$

For small Si and Fe contents ($c^m_{Si} << 1$, $c^m_{Fe} << 1$) and large Al content ($c^m_{Al} \approx 1$) equations (A2.1) and (A2.3) lead to the following expressions of the chemical potentials in the Al-interface [2]:

$$\mu^s_{Al} = G^m_{Al}, \qquad \mu^s_{Fe} = G^m_{Fe} + RT \ln c^s_{Fe}, \qquad \mu^s_{Si} = G^m_{Si} + RT \ln c^s_{Si} \tag{A2.4}$$

If the particle interface is in equilibrium with the interfacial matrix, the chemical potentials of the matrix at the interface (μ_i^s) and in the particle (μ_i^p) must be equal:

$$\mu_i^s = \mu_i^p \quad for \quad i \in \{Al, Fe, Si\} \tag{A2.5}$$

Using equation (A2.3) and the Gibbs free energy of a phase at the stoichiometric composition can be described by:

$$G_{stoich}^p = \mu_{Al}^s c_{Al}^p + \mu_{Fe}^s c_{Fe}^p + \mu_{Si}^s c_{Si}^p \tag{A2.6}$$

Using equation (A2.4), will lead to:

$$(c_{Fe}^s)^{c_{Fe}^p} * (c_{Si}^s)^{c_{Si}^p} = \exp\left(\frac{-\Delta G}{RT}\right) \tag{A2.7}$$

where ΔG is expressed by

$$\Delta G = G_{Al}^m c_{Al}^p + G_{Fe}^m c_{Fe}^p + G_{Si}^m c_{Si}^p - G_{stoich}^p \tag{A2.8}$$

ΔG can be expressed by [2]:

$$\Delta G = \Delta H - T\Delta S\,, \tag{A2.9}$$

where ΔH is the difference in enthalpy of one mole atoms with composition ($c_{Al}^p, c_{Fe}^p\ c_{Fe}^p$) between the particle phase and the matrix phase, in J mol^{-1}. Equations (A2.**7**) and (A2.9) lead to:

$$(c_{Fe}^s)^{c_{Fe}^p} * (c_{Si}^s)^{c_{Si}^p} = k_0 \exp\left(\frac{-Q}{RT}\right), \tag{A2.10}$$

where, in the case of no mixing energy, Q= ΔH . Then Q is the enthalpy change, or heat absorbed, when 1 mol of atoms (in the stoichiometric composition) in the β structure dissolves in the aluminiummatrix k_0 is a pre-factor which is not dependent of temperature, and is equal to $\exp(\Delta S / R)$.

In the same way, as presented in this appendix, it is possible to derive the general solubility product:

$$\Pi_{i=1..N} (c_i^s)^{c_i^p} = k_0 \exp\left(\frac{-Q^s}{RT}\right) \tag{A2.11}$$

where N is the total number of alloy elements (Al is therefore not included).

references

[1] O. Grong: *Metallurgical modelling of welding*. published by the Institute of Materials, 1 Carlton House Terrace, London, Sw1y5DB, 303, (1994).

[2] D. A. Porter, K. E. Easterling: *Phase transformations in metals and alloys.* Published by Chapman & Hall, 2-6 Boundary Row, London SE1 8HN, (1992).

Appendix 3

Further details of the analytical model

For the analytical approach, the concentration profile is assumed to be instantaneous already at the beginning of the phase transformation (t=0). For a planar geometry this gives a linear solution, whereas for a cylindrical geometry this gives a logarithmic solution of the concentration profiles. Now, the aim is to describe the movement of the triple point F (the intersection of the aluminium matrix, α particle and β plate as indicated in Figure 6.2) and the rim position of the β plate, point F. These positions are referred to as P_α (distance EF) and P_β (distance EG) of the α and β phases respectively. Hence, the following diffusion problem is solved:

$$\frac{D}{r^\alpha}\frac{\partial}{\partial r}\left(r^\alpha \frac{\partial c}{\partial r}\right)=0, \quad c(P_\alpha,t)=c_\alpha^s, \quad c(P_\beta,t)=c_\beta^s. \tag{A3.1}$$

Here the constants c_α^p, c_β^p and c_α^s, c_β^s respectively denote the particle and interface concentrations of iron for the α and β phases. The constant a is referred to as the geometric exponent: a=0 and a=1 respectively correspond to the planar and cylindrical case.

Mass conservation on the α and the β interface leads to the following Stefan conditions which describe the movement of both boundaries during time:

$$\left(c_i^p - c_i^s\right)\frac{dP_i}{dt} = D_{Fe}\frac{dc}{dr}(P_i,t), \quad i=\alpha,\beta\,. \tag{A3.2}$$

This condition is independent of the geometry.

A3.1 The planar case

Solution of equation (A3.1), with a=0 for the planar case, gives for the concentration c(r,t):

$$c(r,t)=\frac{c_\alpha^s - c_\beta^s}{P_\alpha(t)-P_\beta(t)}r + B(t)\,. \tag{A3.3}$$

Since only the first derivative of the concentration with respect to r, is of interest only, it is not necessary to calculate B(t) in (8). Note that the time-dependence in the above equation is a result of the movement of the interfaces of the α-particle and β-plate. From a combination of Equation (A3.2) and (A3.3), follows:

$$P_\alpha^{'}(t) = \lambda_\alpha \frac{c_\alpha^s - c_\beta^s}{P_\alpha(t) - P_\beta(t)}, \tag{A3.4}$$

$$P_\alpha^{'}(t) = \lambda_\beta \frac{c_\alpha^s - c_\beta^s}{P_\alpha(t) - P_\beta(t)}, \tag{A3.5}$$

where we define $\lambda_i := \frac{D_{Fe}}{c_i^p - c_i^s}, i = \alpha, \beta$. $\lambda_i := \frac{D_{Fe}}{c_i^p - c_i^s}, i = \alpha, \beta$. Combination of equations (A3.4) and (A3.5) gives:

$$P_\alpha^{'}(t) = -\frac{\lambda_\alpha}{\lambda_\beta} P_\beta^{'}(t). \tag{A3.6}$$

Integration of this differential equation and using the initial condition gives the following relation between P_α and P_β :

$$P_\alpha(t) = P_\alpha(0) + \frac{\lambda_\alpha}{\lambda_\beta}(P_\beta(0) - P_\beta(t)). \tag{A3.7}$$

Now equations (A3.5) and (A3.7) are combined to obtain an ordinary differential equation for Pβ (t) only:

$$P_\beta^{'}(t) = \lambda_\beta \frac{c_\beta^s - c_\alpha^s}{P_\alpha(0) + \frac{\lambda_\alpha}{\lambda_\beta} P_\alpha(0) - P_\beta(t)\left(\frac{\lambda_\alpha}{\lambda_\beta} + 1\right)}. \tag{A3.8}$$

Equation (A3.8) is solved by the use of separation of variables and the initial condition to obtain

$$\frac{1}{2}\left(\frac{\lambda_\alpha}{\lambda_\beta} + 1\right) P_\beta(t)^2 - (P_\alpha(0) + \frac{\lambda_\alpha}{\lambda_\beta} P_\beta(0)) P_\beta(t) + \lambda_\beta (c_\beta^s - c_\alpha^s) t + \xi = 0, \tag{A3.9}$$

$$\text{where } \xi := \frac{1}{2}\left(\frac{\lambda_\alpha}{\lambda_\beta} + 1\right) P_\beta(0)^2 - (P_\alpha(0) + \frac{\lambda_\alpha}{\lambda_\beta} P_\beta(0)) P_\beta(0). \tag{A3.10}$$

Equation (A3.9) is solved to obtain the solution:

$$P_\beta(t) = \frac{1}{1+\frac{\lambda_\alpha}{\lambda_\beta}}\left(P_\alpha(0) + \frac{\lambda_\alpha}{\lambda_\beta} P_\beta(0) + \sqrt{(P_\alpha(0)-P_\beta(0))^2 - 2(\lambda_\alpha+\lambda_\beta)(c_\beta^s - c_\alpha^s)t} \right). \quad \text{(A3.11)}$$

By the use of equation (A3.7), P_α is easily obtained. The time at which the interfaces collide (i.e. $P_\alpha(t_{col}) = P_\beta(t_{col})$ is obtained at the time at which the discriminant in equation (A3.11) is equal to zero:

$$t_{col} = \frac{(P_\beta(0)-P_\alpha(0))^2}{2(c_\beta^s - c_\alpha^s)D_{Fe}\left((c_\alpha^p - c_\alpha^s)^{-1} + (c_\beta^p - c_\beta^s)^{-1}\right)} \quad \text{(A3.12)}$$

This time can be used to estimate the transformation-time. From (A3.12) it is clear that the time at which the interfaces collide is inversely proportional to the difference between the interface concentrations, i.e. c_β^s - c_α^s, assuming that $c_i^p >> c_i^s$, i=α, β. It also follows that t_{col} is inversely proportional to D_{Fe}. (A3.12) also shows that the collision time is quadratic proportional to the initial distance between the α particle and the rim of the β particle, i.e. $(P_\beta(0)-P_\alpha(0))^2$.

A3.2 The cylindrical case

For the cylindrical symmetric case, the geometric factor a=1, then the solution of equation (A3.1) is given by:

$$c(r,t) = \frac{c_\alpha^s - c_\beta^s}{\ln\left(P_\alpha(t)/P_\beta(t)\right)}\ln(r) + B(t). \quad \text{(A3.13)}$$

By combination of equations (A3.2) and (A3.13), the velocity of the interfaces is determined by:

$$P_\alpha'(t) = \lambda_\alpha \frac{c_\alpha^s - c_\beta^s}{P_\alpha(t)\ln\left(P_\alpha(t)/P_\beta(t)\right)}, \quad \text{(A3.14)}$$

$$P_\beta'(t) = \lambda_\beta \frac{c_\alpha^s - c_\beta^s}{P_\beta(t)\ln\left(P_\alpha(t)/P_\beta(t)\right)}. \quad \text{(A3.15)}$$

Combining equations (A3.14) and (A3.15), the ratio of the interface velocities is given by:

$$\frac{P_\alpha'(t)}{P_\beta'(t)} = -\frac{\lambda_\alpha}{\lambda_\beta}\frac{P_\beta(t)}{P_\alpha(t)} \Rightarrow P_\alpha(t)P_\alpha'(t) = -\frac{\lambda_\alpha}{\lambda_\beta}P_\beta(t)P_\beta'(t), \qquad \text{(A3.16)}$$

Integration of equation (A3.16) over t and incorporation of the initial condition gives the following explicit relation between P_α(t) and P_β(t):

$$P_\alpha(t) = \sqrt{P_\alpha(0)^2 + \frac{\lambda_\alpha}{\lambda_\beta}\left(P_\beta(0)^2 - P_\beta(t)^2\right)}. \qquad \text{(A3.17)}$$

Expression (A3.17) is substituted into Equation (A3.15) to obtain the following ordinary differential equation for P_β (t):

$$P_\beta'(t) = \frac{\lambda_\beta\left(c_\beta^s - c_\alpha^s\right)}{P_\beta(t)\ln\left(P_\beta(t)^{-1}\sqrt{P_\alpha(0)^2 + \frac{\lambda_\alpha}{\lambda_\beta}\left(P_\beta(0)^2 - P_\beta(t)^2\right)}\right)}. \qquad \text{(A3.18)}$$

The above equation is solved by the use of separation of variables to get

$$\left(\frac{1}{2}\ln\left(P_\alpha(0)^2 + \frac{\lambda_\alpha}{\lambda_\beta}\left(P_\beta(0)^2 - P_\beta(t)^2\right)\right) - \ln(P_\beta(t))\right)P_\beta(t)P_\beta'(t) = \lambda_\beta(c_\beta^s - c_\alpha^s). \qquad \text{(A3.19)}$$

The above equation is integrated in time and $P_\beta(t)$ using integration by parts. Combination of the obtained results with the initial condition, gives the following relation:

$$\frac{\lambda_\beta}{\lambda_\alpha}\left(P_\alpha(t)^2\ln(P_\alpha(t)) - P_\alpha(0)^2\ln(P_\alpha(0))\right) + P_\beta(t)^2\ln(P_\beta(t)) - P_\beta(0)^2\ln(P_\beta(0)) = 2\lambda_\beta(c_\alpha^s - c_\beta^s)t. \qquad \text{(A3.20)}$$

The above equation gives an implicit relation between $P_\beta(t)$ and t. The condition $P_\alpha(t_{col}) = P_\beta(t_{col})$, at which the interface positions collide, is determined from equation (A3.17):

$$P_\beta^2(t_{col}) = (\lambda_\beta - \lambda_\alpha)^{-1}\left(\lambda_\beta P_\alpha^2(0) + \lambda_\alpha P_\beta(0)\right) \qquad \text{(A3.21)}$$

This position is substituted into equation (A3.20) to obtain the time, at which the interfaces collide, t_{col}.

List of Publications

N. C. W. Kuijpers, J. Tirel, D. N. Hanlon and S. van der Zwaag: *Characterisation of the α-Al(FeMn)Si nuclei on β-AlFeSi intermetallics by Laser Scanning Confocal Microscopy*. J. Mater. Sci. Lett. **22** (2003) 1385-1397.

N. C. W. Kuijpers, F. Vermolen, C. Vuik and S. van der Zwaag: *A model of the β-AlFeSi to α-Al(FeMn)Si transformation in AA 6xxx alloys*. Mater. Trans. **44** (2003) 1448-1456.

S. P. Chen, N. C. W. Kuijpers and S. van der Zwaag: *Effect of microsegregation and dislocations on the nucleation kinetics of precipitation in aluminium alloy AA3003*, Mater. Sci. and Eng. A **341** (2003) 296-306.

N. C. W. Kuijpers, W. H. Kool, P. T. G. Koenis, K. E. Nilsen, I. Todd and S. van der Zwaag: *Assessment of different techniques for quantification of α-Al(FeMn)Si and β-AlFeSi intermetallics in AA 6xxx alloys*. Mater. Char. **49** (2002) 409-420.

N. C. W. Kuijpers, J. Tirel, D. N. Hanlon, and S. van der Zwaag: *Quantification of the evolution of the 3D intermetallic structure in a 6005A Aluminium alloy during a homogenisation treatment*, Mater. Char. **48** (2002) 379-392. (Awarded with the Buehler Technical Paper Merit Award.)

N. C. W. Kuijpers, W. H. Kool and S. van der Zwaag: *DSC study on Mg-Si phases in as cast AA6xxx*. Mater. Sci. Forum **396-402** (2002) 675-680.

N.C.W. Kuijpers: *Microstructuurveranderingen tijdens het Homogeniseren van Aluminium Extrusie Billets*. Aluminium. **3** (2001) 34-35.

J. van de Langkruis, N. C. W. Kuijpers, W. H. Kool, F. J Vermolen, and S. van der Zwaag. *Modeling Mg_2Si dissolution in an AA6063 alloy during preheating to the extrusion temperature*. ET 2000: Seventh International Aluminum Extrusion Technology Seminar. Chicago, Aluminum Extruders Council, **1**, 119-124.

Curriculum vitae

***1973*:** Geboren 12 mei 1973 te Oss.

1991 – 1995: Technische Natuurkunde aan de Hogeschool Eindhoven.

1995 – 1998: Technische Natuurkunde aan de Technische Universiteit Eindhoven.

1998: TU-afstudeeropdracht bij de vakgroep Fysica van Nanostructuren, Faculteit Technische Natuurkunde aan de Technische Universiteit Eindhoven. Titel afstudeerrapport: *Characterisation of nonmagnetic and ferromagnetic tunnel junctions*.

1999 – 2003: Promotie onderzoek te Delft in opdracht van het Nederlands Institute for Metals Research (NIMR). Werkzaam in de groep van Microstructure Control of Metals (MCM), afdeling Technische Materiaal Wetenschappen aan de Technische Universiteit Delft.

2003: Tijdelijke medewerker als materiaalkundige bij PamGene International b.v. te ‘s Hertogenbosch. Werkzaam als gast in de groep van MCM, afdeling Technische Materiaal Wetenschappen aan de Technische Universiteit Delft.

2003 – heden: Materiaalkundige bij Van Doorne’s Transmissie b.v. te Tilburg.

ISBN 90-77172-07-6